FACULTY OF SCIENCE
UNIVERSITY OF COPENHAGEN

Master Thesis

by Martin Kühnel

C_{60} Intercalated Bilayer Graphene

A Structural and Electrical Study

Supervisor: Prof. Jesper Nygaard - Center for Quantum Devices
Co-Supervisor: Jakob Abild Stengaard Meyer - PhD-Student

August 13, 2013

Center for Quantum Devices

Preface

The work of this master thesis was part of the Center for Quantum Devices located in the Nano Science Center at University of Copenhagen. The work was supervised by professor Jesper Nygaard and Phd-student Jakob A. S. Meyer.

Acknowledgement

During the project, many people provided inspiration, technical assistance and feedback, and without whom the project would not have been possible. I would like to express my sincere thanks to each of these. Foremost, Jesper Nygaard my lead supervisor for having diverted time from his busy schedule to guide me.

A special thanks has to go to Jakob A. S. Meyer, my assistance supervisor, for his day to day guidance. Without whom the project would not have been possible.

Furthermore does the following people deserve a huge thank you. Nini Elisabeth Abildgaard Reeler for conducting the Raman Spectroscopy experiments and discussion of the data. Kasper Lincke Rue and Thomas Just for helping with and preparing the potassium intercalation experiments. Marc Overgaard and Poul Norby for conducting the XRD measurements at Risø DTU and at MaxLab Lund, respectively. Bo W. Laursen for general discussion of the project and the possibilities within this.

Additionally, I extend my gratitude to a variety of people who have provided technical assistance during the course of the project, including: Nader Payami, practical laboratory assistance and SEM imaging; Morten Kjærgaard, Electron Beam Lithography (Elionix) and AJA; Tim Booth, initial TEM discussions.

Abstract

The main objective of this thesis was to synthesize a two-dimensional heterostructure consisting of two remarkable carbon structures: two graphene sheets with a C_{60} fullerene monolayer in between, also known as "Carbon Burger". The possibility of synthesizing this structure from two different intercalation methods of the C_{60}-molecules into bilayer graphene samples was studied. The motivation behind the presented work is the promising prospect of the Carbon Burger being a two-dimensional semiconductor with the in-plane properties of pristine graphene.

The first method is thermal intercalation of C_{60} molecules directly into graphene samples. The synthesized structure was characterized by a series of techniques including: AFM, SEM, XRD, Raman spectroscopy and CAFM. With these it is demonstrated that the thermal experiments does not yield the proposed structure, as none of the samples showed signs of successful intercalation.

Another approach presented in this thesis is to ease the intercalation of the large C_{60} molecules by expanding the interlayer distance of graphite by potassium intercalation. The C_{60} molecules are intercalated in solution or thermally.

The unsuccessful experiments inspired a very critical discussion of the results obtained by two articles suggesting the two difference intercalation methods to synthesize C_{60} intercalated graphite. From this discussion a slightly alternative interpretation of the results obtained in the two articles are given.

All in all the work in this project shows no sign of successful intercalation of C_{60} molecules into bilayer graphene nor graphite, hence it is concluded that intercalation is not a suitable route to production of the Carbon Burger, regardless of what is stated in the literature.

Dansk Resumé

Hovedformålet med denne afhandling var at syntetisere en todimensionel heterostruktur bestående af to bemærkelsesværdige kulstofstrukturer, to grafen lag med et enkeltlag af C_{60}-molekyler imellem, også kendt som "Carbon Burgeren". Muligheden for at syntetisere denne struktur ved interkalering af C_{60}-molekyler ind i et dobbeltlag af grafen undersøges med to forskellige metoder. Motivationen for afhandlingen er Carbon Burgerens potentiale som todimensionel halvleder med samme egenskaber som grafen.

Den første metode er termisk interkalering af C_{60}-molekylerne direkte ind i grafen prøven. Den syntetiserede struktur undersøges med følgende eksperimentelle teknikker: AFM, SEM, XRD, Raman spektroskopi og CAFM. Det demonstreres at det termiske eksperiment ikke giver den foreslåede struktur, da ingen prøver viste tegn på succesfuld interkalering.

En anden foreslået fremgangsmåde er at lette interkaleringen af de store C_{60}-molekyler ved at forøge grafen-grafen afstanden i grafit ved interkalering af kaliumatomer. C_{60}-molekylerne er bagefter forsøgt interkaleret enten igennem opløsning eller termisk.

De usuccesfulde eksperimenter igangsatte en grundig og kritisk diskussion af resultaterne fra to artikler omhandlende interkaleringsteknikkerne. På baggrund heraf foreslås en alternativ fortolkning af de to artiklers resultater.

Overordnet set viser resultaterne fra afhandlingen ingen tegn på succesfuld interkalering af C_{60} i hverken dobbeltlaget grafen eller grafit, og det konkluderes at interkalering ikke effektivt kan anvendes til syntese af Carbon Burgeren.

Contents

List of Figures

List of Abbreviations

#LG # Layer Graphene

AFM Atomic Force Microscopy

BLG BiLayer Graphene

BSE Back-Scattered Electrons

C-AFM Conducting Atomic Force Microscopy

DOS Density of State

EBL Electron Beam Lithography

fcc Face-Centered Cubic

FLG Few Layer Graphene

GIC Graphite Intercalated Compounds

GNR Graphene Nano-Ribbon

hcp Hexagonal Close-Packed

HOPG Highly Oriented Pyrolytic Graphite

HRTEM High Resolution Transmission Electron Microscope

IPA IsoPropyl Alcohol

NN Nearest Neighbour

NNN Next-Nearest Neighbour

RT Room Temperature

SE Secondary Electrons

SEM Scanning Electron Microscope

SLG Single Layer Graphene

TEM Transmission Electron Microscope

XRD X-ray Diffraction

Chapter 1

Introduction

Nano and molecular electronics are two fields of science which in recent years have undergone a huge development. Since the discovery of graphene[59], a one atom thick two dimensional (2D) honeycomb network of carbon atoms, the field of graphene based electronic systems has in record time become one of the largest in nano-electronics. Graphene based devices are thought as a possible solution towards low-cost and flexible nano-electronics, and even thought as a one of the candidate materials for post-silicon electronics[76].

The main objective of this master thesis is to develop a 2D transistor, consisting of two exciting carbon structures, namely graphene, a semi-metal, and C_{60} molecules, a semiconductor in the crystal phase. The principle behind the design is a 2D all carbon heterostructure, where a monolayer of C_{60} molecules is intercalated in between two sheets of graphene, also referred to as the Carbon Burger, see figure 1.1. Hopefully this design preserves the prominent in-plane properties of graphene, but introduces a band gap in the z-direction*, as the electrons has to cross the C_{60}-monolayer to jump between the two electrodes (the two graphene layers). For a device with a perfect C_{60} it is expected that electrons will travel from one electrode to the other, through the LUMO† state of C_{60}, when inducing a potential difference between the two electrodes large enough to raise the Fermi level in the vicinity or above the band gap of the C_{60} molecules, depending on the temperature of the measurement.

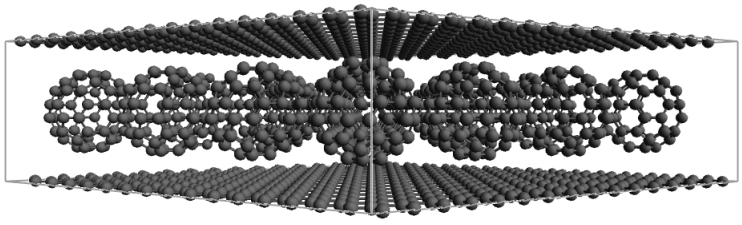

Figure 1.1: Suggested structure of the C_{60} intercalated monolayer between two pristine graphene sheets, also known as the Carbon Burger.

To support the physics behind this design, Cho et al.[16] reported a band gap of ~ 3.5 eV for C_{60}-molecules adsorbed on a graphene/SiC surface, which is comparable with that of solid C_{60}. Compared to C_{60} on metallic substrates, the charge transfer from graphene to C_{60} is much smaller. In fact,

*z-direction being orthogonal to the planar graphene

†Lowest Unoccupied Molecular Orbital

recently published data by Wang et al.[84] estimates the charge transfer to be of the order 0.01 electron per C_{60} molecule, hence an increase in the z-direction resistance might be measurable even at room temperature. A finite charge transfer occurs even though both graphene and C_{60} only consist of carbon atoms with three neighbours. This effect can be understood by considering the hybridization of both carbon structures, where the hybridization of the carbon atoms in graphene are pure sp^2 and in a C_{60}-molecule are not. This originates from the curvature of the C_{60}-molecules, which does not hybridize the $2s$ and $2p$ orbitals in pure sp^2, hence the π-state does not purely consist of $2p_z$-orbitals, but also have a finite $2s$-component[74]. Chapter 2 give a more thorough introduction to the two carbon structures and the proposed 2D heterostructure.

An experiment, highly inspired by the work of Gupta et al.[28], where C_{60}-molecules can be intercalated into bilayer graphene (BLG), was proposed and tested. After the experiments on the the all-carbon heterostructure are conducted, structural and electrical characterizations are carried out. Graphene flakes are produced by mechanical cleavage of graphite[59] and the intercalation is done by thermal heating[28]. The experimental details are presented in full in section 3.2 and appendix A.

Different characterization techniques are used throughout this project. Structural characterization with use of three different kinds of microscopes, namely Optical, Atomic Force (AFM) and Scanning Electron (SEM) microscopes, along with Raman spectroscopy and X-Ray Diffraction (XRD). For electrical measurements wafers with in-plane electrodes are produced, with one of the graphene layers in the above described C_{60} intercalated BLG compound in contact. Electrical contact to the upper graphene layer, and conductance measurements at room temperature, are performed with a modified AFM. The technique, know as conducting AFM (CAFM), works by engaging a conductive AFM tip, which can be used as an electrode, probing the surface at different sites. For an introduction to the different techniques see section 4.

An alternative approach towards fullerene intercalated BLG was attempted, where potassium intercalated graphene was used as a pre-cursor, easing the fullerene intercalation step by increasing the inter-planar distance. Besides contributing to increasing the interlayer distance, potassium might potentially have a huge influence on the electrical properties. Co-intercalation of potassium and C_{60} into graphite has been reported to be superconducting with a transition temperature of 19.5 K[23]. A similar approach, as reported by Fuhrer et al.[23], towards co-intercalation is attempted, with thermal intercalation of potassium and solution based intercalation of C_{60}-molecules. Finally an approach with thermal intercalation of both potassium and C_{60}-molecules is suggested and performed. All results obtained throughout this thesis are presented and discussed in chapter 5.

To summarize, the overall structure of this thesis is as follows: Chapter 2 introduces the field of nano electronics through a brief historical review, followed by a thorough description of graphene and C_{60}-molecules, both its structural and electronic properties. Lastly it review the relevant article inspiring the work of the thesis; Chapter 3 describes the experimental details; Chapter 4 introduces the applied characterization techniques; Chapter 5 is a presentation and discussion of the results obtained through the course of the project; Last but not least chapter 6 gives the final remarks and tries to give an outlook.

Chapter 2

Background

Chapter two gives the reader a short overview of some of the exciting science conducted from the first proposed electronic device based on molecular properties, up to present time, where graphene leads the field as one of the most intriguing materials. The two key elements in the carbon burger, graphene and C_{60}-molecules, will be reviewed individually, with main focus on the electronic properties. Finally the work leading up to this thesis will be presented and some predictions towards the electronic properties of the heterostructure will be made.

2.1 Historical Review

Nano molecular electronics are the next step in the ever evolving field of electronic devices, where optimizing size, power consumption and performance have been amongst some of the main objectives for many decades. Ever since, Aviram and Ratner[4] first published a theoretical paper in 1974 on the subject of molecular electronics, proposing single molecules as the base for electronic devices (in this case a rectifier), the interest in the field of nano electronics has been constantly increasing. A wide variety of devices have been suggested, ranging from single molecule electronics[54] to 2D film of molecules[14]. In all cases the need for good molecule-electrode contact is crucial in order to take advantage of the specific molecular properties. So far most molecular electronics are with metal electrodes, where specialized side groups attached to the molecule of interest are a necessity for providing good molecule-electrode contact. Commonly the devices are build from gold electrodes due to the stability of its electronic and structural properties, with sulphur atoms as the bonding group due to the strong gold-sulphur interaction[69].

A new branch in molecular electronics, where devices are based on graphene, has since the discovery of graphene in 2004[59] undergone a huge development. One of the latest developments in graphene science is it being used as electrodes, where it is regarded as a good candidate for leading the field towards commercial success, due to its incredible electronic and structural properties, albeit still some way out in the future. The properties of graphene will be reviewed more thorough in section 2.2. In general the interest in graphene is high, not only as electrodes. The hugh development the area of graphene science has undergone, is well illustrated by the evolution of scientific papers with graphene as topic, see figure 2.1. The first publications using the term graphene are from 1991, 13 years before

the discovery, and thus only used when referring to a single atomic layer in graphite. It is evident that the real evolution started few years after the work by Novoselov et al.[59] leading to the discovery of graphene, and that this development is still ongoing with an expected number of publications reaching close to 10.000 for 2013.

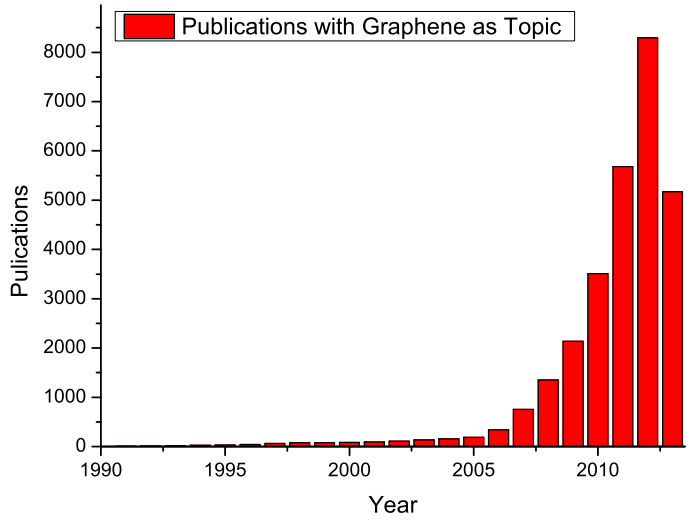

Figure 2.1: The evolution of number of publications per year with graphene as topic from 01.01.19 to 29.07.13. The first publication referring to graphene are as early as 1991, 13 years before its discovery.

In molecular electronics most devices are basically build from one of two main designs. These being an in-plane design with two side-electrodes or a horizontal with a top and bottom electrode. The principal behind the two designs are illustrated in figure 2.2. The two designs hold different advantages and are hence used equally often.

The side-electrode design is normally made pre-deposition of molecules and is optimal for single molecule electronics[54]. For single molecule electronics narrow gaps of the order of the molecule between the two electrodes are essential. Many production methods have been suggested, including breakage by electromigration in a gold nanowire[66] and mechanical breakage of the nanowire[69]. Most of them have one thing in common, namely the uncontrollable geometry of the produced electrodes. Exactly the geometry has been proved to hold a high influence on the molecule-electrode contact[52]. Hence control of this factor is very desirable if the specific molecules electronic properties are to be probed and not the randomized e.g. sulphur-gold interaction. Martin et al.[46] reduced the fluctuations due to individual atomic details at the anchoring sites by using C_{60}-molecules to end-cap linear molecules for molecular electronics. C_{60}-molecules are with its high symmetry and strong hybridization with gold[71], a good candidate for stable anchoring molecules[79].

Another solution is to expand to a multi-molecule device. By having multiple molecules conducting, the random individual contact resistances should be ruled out, and the molecule of interest can be measured. Most such devices are made as a horizontal device. In general the production steps are first to deposit the bottom electrode, followed by the molecular layer and finally deposition of the

top electrode. When depositing the top electrode, holes in the molecular film might lead to short circuits of the device[30]. This unwanted effect can be prevented using graphene as top electrode. A perfect graphene sheet are impenetrable to metal, hence working as good blocking and contact material between the molecular thin film and metal or just as a sole electrode.

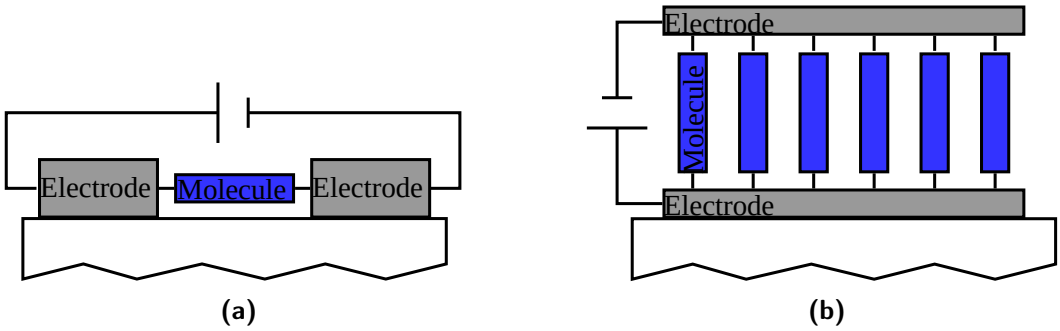

Figure 2.2: Schematic presentation of two types of molecular electronic devices. **(a)** Two in-plane electrodes. Typical used for single molecule electronics. **(b)** Horizontal design, with a top and bottom electrode. This design is most suitable for devices with molecular films.

The idea of an all-carbon heterostructure, where the electrodes consist of graphene and the molecules of interest a C_{60}-molecules originates from the need of better molecule-electrode contact as described above. By using the C_{60}-molecules, not only as anchor molecules but as the molecule of interest, a hopefully monolayered semiconductor can be created, with good contact to the graphene electrodes. Further details on the design and experimental approach used in this thesis are given in section 2.4. A different route towards the Carbon Burger, is a more step-by-step building approach, with three main steps. First deposition of a bottom graphene electrode, followed by metal electrode design and deposition with lithography. Second, deposition of C_{60}-molecules within a well-defined area of the graphene electrode and some kind of resistor covering the remaining part. Third and last is deposition of the top graphene electrode. The production method can be applied to all kinds of molecules, not only C_{60}. The biggest disadvantage of this method is the difficulties in mass production, but as the production and transfer of graphene on arbitrary wafers improves, the difficulties encountered minimizes.

2.2 Graphene

Since first discovered in 2004 by Novoselov et al.[59], graphene, an one atom thick densely packed 2D hexagonal lattice of carbon atoms, has been regarded as one of the most promising materials for molecular electronics. The discovery of graphene is the latest development in the evolving field of carbon science, which already includes three-, one- and zero-dimesion structures. The three structures, 3D graphite, 1D carbon nanotubes and 0D fullerene, can be visualized by either stacking, rolling or wrapping up graphene[24], respectively, see figure 2.3. The great attention given to graphene is due to both its unique molecular and electronic properties. Transparency and it being the strongest, thinnest, most flexible known material are just some of the exciting molecular properties. Quasi-particles acting like massless Dirac fermion carriers[60], high mobility and it being a zero gap semiconductor are amongst

the most distinctive electronic properties[68]. In order to understand these exciting properties, one has to look deeper into the basic science of graphene.

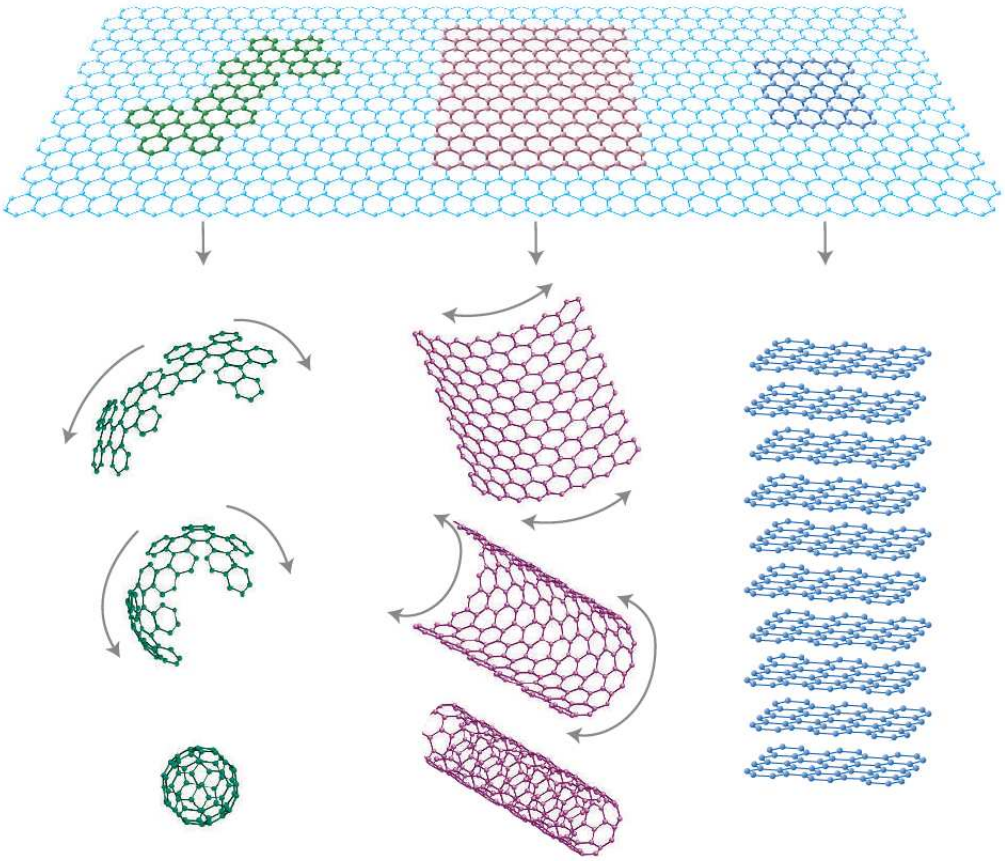

Figure 2.3: Visualization of graphene as building block for other dimension carbon structures. From left to right it is graphene wrapped up to a fullerene molecule (0D), rolled up to a nanotube (1D) and stacked to form graphite (3D). Adopted from Geim and Novoselov[24].

2.2.1 Structural Properties

As mentioned above, the carbon atoms (sp^2-hybridized) in graphene are ordered in a planar hexagonal lattice, in which strong covalent bonds are formed between neighbouring carbon atoms. The strong σ-bonds and the high crystalline purity, makes graphene stronger than diamond, but very flexible when a force is applied[42]. The transparency of graphene (and FLG) in the visible light range, is the property that prolonged the discovery of graphene[67;68]. One of the first attempts to cleave graphite into thin graphite films, was done as early as 1960 by Fernandezmoran[20], where graphite single crystals down to a thickness of $5-50$ nm ($\sim 15-150$ layers) are reported as a support membrane for electron microscopy. These membranes were produced using micro-mechanical exfoliation, basically the same method as used by Novoselov et al.[60], which are just one amongst many suggested methods for graphene production. Other methods are chemical vapour deposition of hydrocarbons on reactive nickel thin film[37], reduction of graphene oxide films made from solution[19] and annealing of SiC substrate to form FLG[6]. All of these chemical approaches holds the advantage over the mechanical

exfoliation process of being suitable for large scale and reproducible production, but as to this date does not have the same quality as pristine graphene.

The unit cell of graphene is hexagonal and consist of two carbon atoms, C_A and C_B. 3D graphite is constructed by stacking individual graphene layers in a Bernal (AB) stacking order, in which the center of each hexagon are aligned with the corner of a hexagon on adjacent graphene layers[45]. The unit cell of graphite consist of 4 carbon atoms from two graphene layers, C_{A1}, C_{B1} C_{A2} and C_{B2}. Reducing the number of stacked graphene layers, going from graphite to multilayer graphene (MLG), does not change the stacking arrangement or the unit cell, and in fact does the unit cell of bilayer graphene contain four carbon atoms, as for graphite*. 3LG is constructed from a bilayer sheet with a single layer graphene (SLG) on top, 4LG from two BLG and so on. The two individual types of atoms in the unit cell for SLG can be described by two sub-lattices, A and B, which both are triangular Bravais lattices. The unit cell is expanded by the following unit vectors: $\mathbf{a}_1 = a(-1, 0)$ and $\mathbf{a}_2 = a(-1/2, \sqrt{3}/2)$, whit lattice constant $a = 2.461$ Å, see figure 2.4a. Atom A and B are located at $\mathbf{R}_s = n_1\mathbf{a}_1 + n_2\mathbf{a}_2 + \mathbf{r}_s$ where the vectors $\mathbf{r}_s$ $(s = A, B)$ defines the position of atom A and B in the unit cell. Constructing the same unit cell of graphite, a third-dimension unit vector has to be defined.

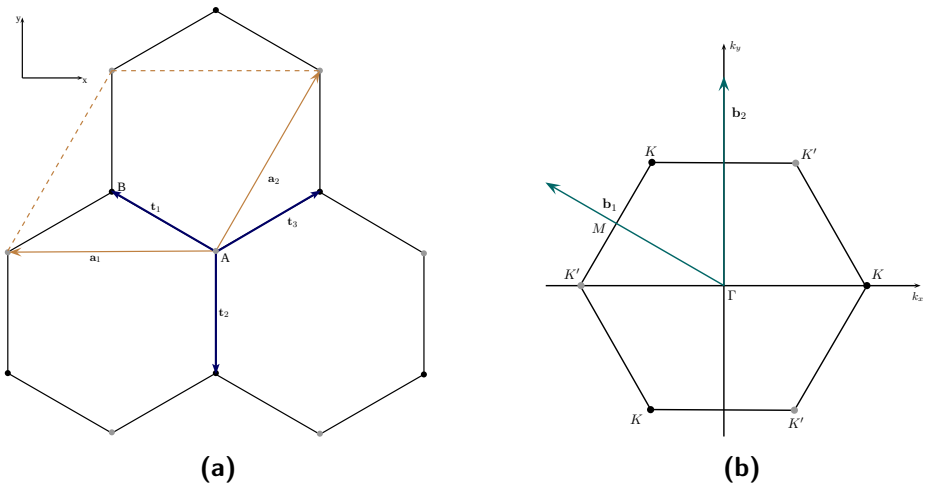

Figure 2.4: **(a)** Real space hexagonal lattice for graphene. $\mathbf{a_1}$ and $\mathbf{a_2}$ are the lattice vectors expanding the unit cell. The two different atoms in the unit cell are denoted A and B. **(b)** Reciprocal space representation of (a), with $\mathbf{b_1}$ and $\mathbf{b_2}$ the reciprocal lattice vectors. Points of high symmetry are denoted Γ, K, K' and M.

2.2.2 Electronic Band Structure

Graphene consist of two carbon atoms per unit cell, contributing four valence electrons each. Three of the four valence electrons on each carbon atom are sp^2-hybridized and forms σ-bonds to the three nearest-neighbour (NN) atoms, with a bond length of approximately 0.14 nm. The fourth valence electron, described by the p_z-orbital perpendicular to the graphene plane, is used to create a large de-localized π-system expanding over the whole graphene sheet, by forming π-bonds to neighbour

*It should be noted that not all production methods yields an AB-stacking arrangement for BLG, but as all graphene samples in this project are produced with mechanical cleaving, which does give AB-stacking, only this type of graphene will be considered.

p_z-electrons. Hence the valence band is the bonding molecular orbital, π, and the conduction band the anti-bonding, π^*. As the two carbon atoms in the unit cell each contribute one electron to the π-system, the valence band is totally filled and the conduction band empty.

The first description of the band structure of graphene, was by Wallace[83] in 1947, a whole 57 years before the discovery of graphene. He used the tight-binding approximation, to calculate the band structure for a single atomic sheet in graphite, where only interactions between nearest- and next-nearest-neighbour atoms on the sheet were included. Furthermore the overlap between individual $2p_z$-orbitals were neglected. Following this approximation, correctly yields a semi-metal, with no charge carriers at the Fermi-energy at 0 K, but incorrectly gives a symmetric valence and conduction band around the Fermi energy. Latter calculations have corrected for this error by including the overlap integral between neighbour atoms[70;72].

A simple calculation of the electronic band structure, neglecting all interactions except between nearest neighbour, and including the overlap integral, is conducted as an introduction to the electronic properties of graphene. For SLG the energy bands of interest are the π^* and π electronic states, originating from the large conjugated system of p_z-orbitals. The tight-binding model gives a satisfactory result, when trying to model these bands[1;25]. For details on this simple energy band calculation see appendix C. The expression obtained for the energy, $E(\mathbf{k})$, in terms of the wave vector, $\mathbf{k}$, is within the above stated assumption given as

$$E(\mathbf{k}) = \frac{\epsilon_{2p_z} \pm \gamma_0 \sqrt{|f(\mathbf{k})|^2}}{1 \pm s_0 \sqrt{|f(\mathbf{k})|^2}}$$

The three parameters ϵ_{2p_z}, γ_0 and s_0, are the orbital energy of the $2p_z$-orbital, the transfer integral and the overlap integral, respectively. These values can be estimated by fitting either experimental or first-principle calculation data[70]. The sum of phase factors, $f(\mathbf{k})$, is given as

$$f(\mathbf{k}) = 2\cos\left(\frac{a}{2}k_x\right)\exp\left(i\frac{a}{2\sqrt{3}}k_y\right) + \exp\left(-i\frac{a}{\sqrt{3}}k_y\right)$$

Figure 2.5 shows three different plots obtained with Matlab[48], where 2.5b is a 3D representation of the energy dispersion for graphene and 2.5a is a line plot of the same, between points of high symmetry, see figure 2.4b. The values used are $\epsilon_{2p_z} = 0$, $\gamma_0 = -3.033$ and $s_0 = 0.129$, which are obtained from Saito et al.[72].

Figure 2.5c shows the linear energy dispersion around the symmetry point K, which can be explained as the charge carriers being massless. This originates from the effective mass being inverse proportional to the second derivative of the energy, which for a straight line is zero. The physical impact is amongst many anomalous integer quantum Hall effect[60]. Another surprising discovery with graphene was the measurement of quantum Hall effect at room temperature[61].

The most important property of graphene for this project is the very high charge carrier mobility, μ[60]. The carrier mobility is reported to exceed 20000 $c\mathrm{m}^2\mathrm{V}^{-1}\mathrm{s}^{-1}$, and expectation is that it might reach 200000 $c\mathrm{m}^2\mathrm{V}^{-1}\mathrm{s}^{-1}$, higher than reported for any know material[24;53]. Being measured under ambient conditions and high charge carrier density ($> 10^{12}$ cm), only additional add to the significant impact of these numbers.

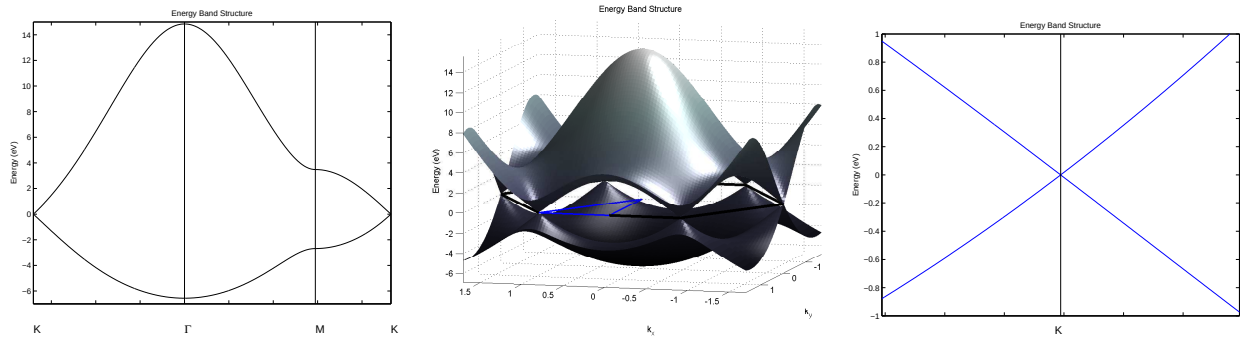

(a) **(b)** **(c)**

Figure 2.5: Calculated energy dispersions for graphene with use of the tight-binding approximation and the software Matlab[48]. **(a)** A line plot of the energy dispersion for the valence and conduction band for graphene along point of high symmetry, see figure 2.4a. **(b)** 3D plot of the energy dispersion. The blue marked triangle is the route of the line plot in (a). **(c)** Energy dispersion around the symmetry point K, showing the linear relation between the energy and the wave vector.

Expanding the Model

For a more precise calculation of the electronic band structure, one has to not only consider NN, but also 2nd and 3rd etc. Two approaches are at present done, one going to 3rdNN with non-orthonormal p_z-orbitals[26;70] and one to 5thNN with orthonormal p_z-orbitals[81]. For a complete image of the electronic bands, not only the valence and conduction bands needs to be included. But as an illustrative example of the most basic electronic properties of graphene, the band structure seen on figure 2.5 is adequate.

Bilayer Graphene

The same model can relative simple be applied to calculation on BLG, by expanding the unit cell to include four different carbon atoms[49;50]. Doing so increases the amount of carbon-carbon interactions which should be taking into account, complicating the calculations. Because the unit cell of BLG consist of four carbon atoms, thus four valence electrons[12], its band structure consist of two extra bands. The four bands comes in pairs of two, one for the conduction band and one for valence band. Over most of the Brillouin zone, each pair is split by an energy of the order of the interlayer coupling, ~ 0.4 eV[51]. Around the K-point one conduction band and one valence band are degenerate at the Fermi energy, while the other two split away from zero energy by the order of the interlayer coupling[57].

2.2.3 Band Gap in Graphene

One disadvantage of graphene is the lack of a band gap, making pristine graphene unsuitable for room temperature (RT) transistor with a sufficient on/off ratio. Many experiments towards opening a band gap in graphene, have so far been attempted. As the goal of this thesis can be seen as an attempt towards incorporating a band gap in graphene, two alternative approaches, which shows promising prospects with regard to nano-electronics will be presented below.

One approach is to narrow in a graphene sheet and create the structure called graphene nano-

ribbon (GNR)[15]. Narrowing a 2D graphene sheet sufficiently, alters the 2D energy dispersion into a number of 1D modes. These 1D modes depends on the boundary conditions, when narrowing below 50 nm, and does in some cases not intersect at the Fermi energy as for pristine graphene. Instead a finite band gap is produced, making the quasi-1D GNR semiconducting. The electronic properties are highly dependent on the type of edges, e.i. armchair or zig-zag, where the prior is either semiconducting or metallic dependent on the width, while the later always is a metallic conductor[77]. The increased dependency of the edges induces scattering, hence reduces the charge carrier mobility[15]. The reduced mobility is the biggest disadvantage of the graphene nano ribbons.

The nano-pattering of graphene is of great importance in order to produced well-defined GNR, hence controlling the electronic properties. Most commonly the pattering is done with lithography, which has been optimized through the need of well defined electrodes. For metal electrodes, the smallest features are obtained with use of Electron Beam Lithography (EBL). Features below the 10 nm range have been obtained by cold developing an exposed PMMA film[32]. Pattering graphene can be done by different etching procedures, e.g. argon[85] or oxygen[87] plasma etching. Sub-nanometer resolution have been achieved by Boerrnert et al.[9] by using a high precision electron beam to cut in suspended graphene. Another approach towards producing GNRs is by unzipping carbon nanotubes[38].

The second approach were first realized by Ohta et al.[63], who published a paper on tunable band gap in bilayer graphene. By render individual graphene layers in a bilayer inequivalent, a band gap is opened at the former Dirac point due to a potential difference between the two layers[49]. Experimentally this was realized, by inducing a dipole field across a bilayer graphene sheet on a SiC surface. The dipole was induced by the depletion layer of the SiC surface and the accumulation of charges on the graphene layer next to the interface. The accumulated charge render the two graphene layers differently, opening a band gap at the Dirac point. The size of the band gap were controllable by adsorption of charges, in the form of potassium ions, on the BLG. Castro et al.[11] showed that the electronic band gap can be controlled externally by a gate voltage. Their device was a bilayer graphene sheet on a SiO_2/Si-wafer, where the insulating oxide layer worked as a blocking layer, for inducing a gate voltage between the BLG sheet and the Si-wafer, changing the charge carrier concentration differently for the two layers in the BLG. This type of device should preserve the high mobility of graphene (the BLG should have approximately the same charge carrier density as graphene[53]), as the mobility is expected to depend mainly on charged impurities and microscopic ripples[53], hence the doping should not alter the mobility significantly. This makes back-gated BLG devices one of the most promising solution to produced room temperature transistor with a sufficient on/off ratio.

2.3 Buckminsterfullerene

The soccer-ball shaped (or icosahedral) structure of C_{60}-molecules, see figure 2.6d, was first realized by Kroto et al.[40] in 1985. Pure C_{60} crystals were first time synthesized by Kratschmer et al.[39] in 1990. The crystal phase is now known to be face-centred cubic (fcc)[41], and not hexagonal close-packed (hcp) as suggested by Kratschmer et al.[39]. The hcp structure observed in the early work with C_{60} are formed when the C_{60}-crystal is not entirely pure, e.g. solvent residues[41]. The C_{60} pack with a nearest neighbour distance of approximately 10 Å. Each individual C_{60}-molecule has a diameter of 7

Å, and consist of 12 pentagons and 20 hexagons, see figure 2.6d. Two different carbon-carbon bonds are present in the molecular structure, namely one between a hexagon and a pentagon and another shared by two hexagons. Each carbon atom form σ-bonds to three neighbour atoms, but due to the curvature of the molecule, the carbon atoms are not purely sp^2-hybridized. Instead does each σ-bond include of a finite part of the $2p_z$ orbital[†], and similarly for the π-bond, which have a finite component from the sp^2-hybridized orbital.

2.3.1 Electronic Band Structure

The electronic band structure of both a single molecule and a crystal can be seen in figure 2.6, showing calculations conducted by Saito and Oshiyama[74]. Figure 2.6a show the energy levels for a single C_{60}-molecule, where the arrows indicate the six lowest allowed transitions. The energy gap between the highest occupied molecular orbital (HOMO), the h_u-level, and the lowest unoccupied, the t_{1u}-level, is 1.9 eV for a single C_{60}-molecule. The calculations for a crystal can be found in 2.6b, with 2.6c being a zoom of around the Fermi level, showing a direct band gap of approximately 1.5 eV[74]. Saito and Oshiyama[74] assign energy bands between -6 eV and 7 eV to the π-bond states, as all energy levels in this region are highly dispersive in the crystal phase due to a large overlap with neighbour molecular orbitals, see figure 2.6b. All other states are assigned to the less spacious σ-bond states, with a contrary argument.

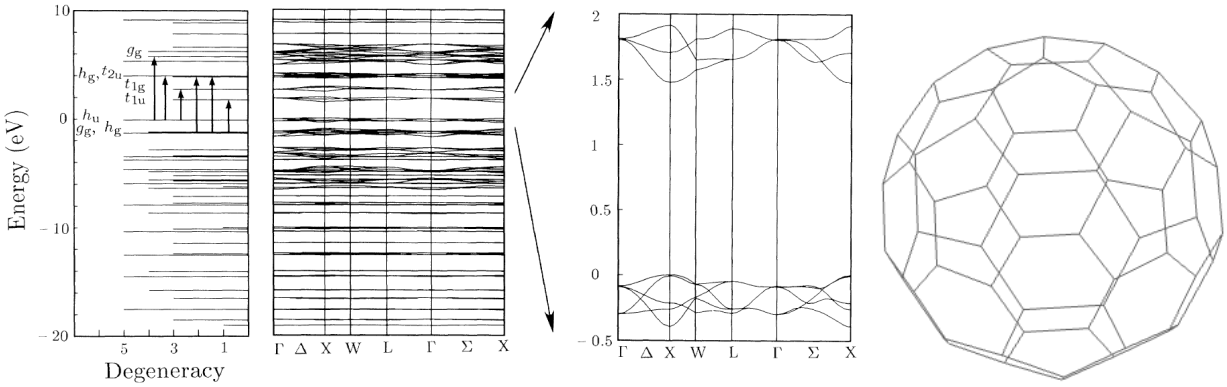

Figure 2.6: The C_{60} molecule **(a)** Energy level calculation for a single C_{60}-molecule. The band gap between the h_u and t_{1u} is calculated to 1.9 eV. **(b)** Energy calculation for a C_{60} crystal. **(c)** The same calculation as in (b), just focused around the Fermi level, showing a direct band gap of 1.5 eV. **(d)** A stick drawing of a single C_{60}-molecule, consisting of 12 pentagons and 20 hexagons of carbon atoms. (a), (b) and (c) adopted from Saito and Oshiyama[74]

2.3.2 Superconductivity

The electronic properties of solid C_{60} are very sensitive to doping, and alkali metal doped C_{60} solid is shown to be superconducting with transition temperature as high as 33 K for $RbCs_2C_{60}$[80] and 40 K for 15 $k$bar pressurized Cs_3C_{60}[65]. Potassium intercalated C_{60}, K_3C_{60}, is also superconducting

[†]The z-direction being perpendicular to the spherical surface and is hence different for individual carbon atoms in the C_{60}-molecule

with a transition temperature of 18 K[31]. The superconducting effect is thought to stem from a doping effect, increasing the amount of charge carriers at the Fermi level[73]. More precise a metallic state is achieved, by raising the Fermi level so the t_{1u}-level is approximately half-filled, corresponding to stoichiometry M_3C_{60}. The transition temperature is dependent on the size of intercalant and the number of atoms per C_{60}-molecule. This dependency can be understood by considering the influence of the effectively increased lattice constant. Increasing the lattice constant, decreases the intermolecular C_{60}-C_{60} coupling hence narrowing the HOMO band, which in the doped crystal is the t_{1u}-level. A narrowed band have a corresponding increased density of state (DOS), hence a higher transition temperature as this is depend on the DOS[18]. However this is not true for all phases, e.g. the K_6C_{60} being insulating[18], where the potassium dopes the C_{60} so the Fermi energy lies in a higher energy band gap.

2.4 The Carbon Burger Reviewed

This thesis uses two carbon structures, namely graphene and C_{60}, with graphene as the main target of interest and the C_{60} molecule a more arbitrary choice. The experimental work is divided into two parts, one with intercalation of C_{60} into bilayer graphene and another with co-intercalation of potassium and C_{60}. These two parts will be introduced individually.

2.4.1 C_{60} Intercalated Bilayer Graphene

The idea of a pure carbon structure consisting of C_{60} intercalated graphite, was suggested in a theoretical paper by Saito and Oshiyama[75] in 1994. Saito and Oshiyama[75] used density-functional theory (DFT) calculations to predict the electronic band structure of stage-1 C_{60} intercalated graphite, with a hexagonal close-packed C_{60} monolayer. The stage number of a graphite intercalated compound (GIC) denotes the number of graphene layers separating each intercalation layer. With this model the unit cell of the intercalation compound contains 32 graphene carbon atoms per C_{60} molecule, $C_{32}C_{60}$. The results from their calculations can be seen in figure 2.7. Figure 2.7b and 2.7c are the electronic band structure for graphene and a monolayer of C_{60}, respectively. They note that a similar result as the calculated band structure for the intercalated compound (figure 2.7a), can be obtained by simply merging that of graphene and C_{60}, and aligning the Fermi levels. Such a simple approach does (of course) not give the right results, as some interaction between the graphene layers and the C_{60} layers must be expected. Valence electron density calculations from the same paper does indeed show changes compared to pure graphene and C_{60}, with a charge transfer towards the C_{60}-layer. The charge transfer can be understood from a simple consideration of the π states of planar graphene and spherical C_{60}. Even though the carbon atoms in both graphene and C_{60} are sp^2-hybridized, the curvature of the C_{60} molecule introduces a s-orbital component to the π-state, which are not pure p_z-orbital as for a perfectly planar graphene sheet. Hence the C_{60} π-state is lower in energy and a finite charge transfer from graphene to C_{60} must be expected. Saito and Oshiyama[75] does not estimate the size of the charge transfer. This can be determine from a simpler system, with a monolayer of C_{60} deposited on a graphene sheet, and indeed many such studies have been performed, both structural[44], electrical[16;82]

and theoretical[82]. Cho et al.[16] determines the direct HOMO-LUMO gap of C_{60}-molecules on an epitaxial grown graphene on SiC to be ~ 3.5 eV. They report reduced charge transfer from graphene to C_{60}, when comparing with C_{60} on various metallic substrates. Furthermore it is confirmed that the C_{60}-molecules forms a hcp monolayer on graphene, with a nearest neighbour distance of ~ 1 nm, comparable to that of solid C_{60}. The charge transfer from graphene to a C_{60}-molecule is of the order of 0.01 electron[84], hence the Fermi energy is expected to still lie within the band gap of the C_{60} monolayer, as calculated by Saito and Oshiyama[75].

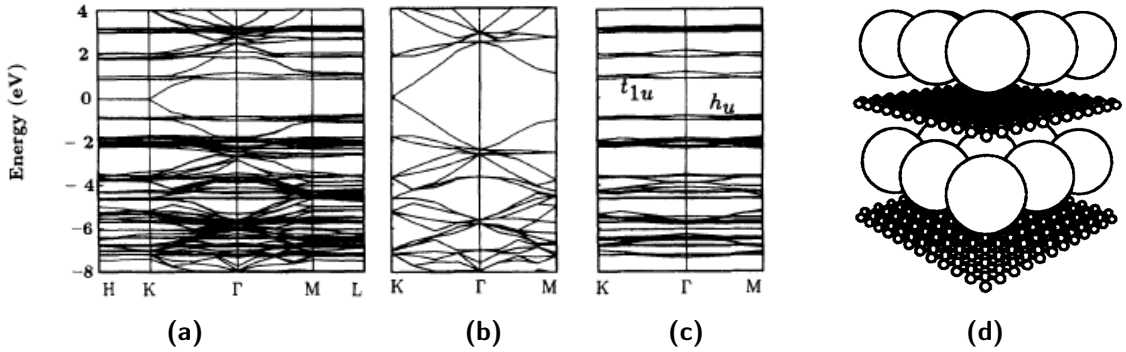

Figure 2.7: C_{60} intercalated graphite **(a)** Energy band calculation of the $C_{60}C_{32}$ structure, arranged as seen in (d). **(b)** Energy band calculation for C_{32} unit cell. **(c)** Energy band calculation for a C_{60} molecule. **(d)** Proposed arrangement of the intercalated C_{60} molecules between graphene layers in graphite. (a), (b), (c) and (d) adopted from Saito and Oshiyama[75]

The first group to directly intercalated C_{60} into graphite were Gupta et al.[28‡]. They show that by heating C_{60} powder and graphite powder to 600°C for 2 weeks, a highly ordered stage-1 GIC is produced. This observation is supported by the Transmission Electron Microscope (TEM) and Raman measurements seen in figure 2.8. Figure 2.8a is a High Resolution Transmission Electron Microscope (HRTEM) image of pristine graphite. HRTEM image of the GIC where each individual C_{60} molecule are visible and one marked by an arrow is presented in figure figure 2.8b. Gupta et al.[28] observe an increased interlayer distance, marked by the two parallel lines , measured to 1.27 nm. The enhanced interlayer distance was estimated to 1.29 nm, and is in good agreement with the observed distance in figure 2.8b. The synthesized material showed hexagonal symmetry obtained from selected area diffraction data (not shown here, but will be discussed in section 5.5).

The Raman data for the intercalated compound can be seen in figure 2.8c. Assigning the three peaks from right to left in the same way as Gupta et al.[28], the first is the G-peak for graphite, up-shifted from the usual 1582 $c\text{m}^{-1}$ to 1589 $c\text{m}^{-1}$, due to electron transfer from graphite to C_{60}. This postulate is in good agreement with the small charge transfer expected by Saito and Oshiyama[75]. The same charge transfer down-shift the peak for pristine C_{60} from 1469 $c\text{m}^{-1}$ to 1446.1 $c\text{m}^{-1}$. The electron transfer is expected to partially fill the t_{1u} level, making the C_{60} layers highly conductive. Lastly the broad peak at 1370 $c\text{m}^{-1}$ is a D-peak, indicating slightly defected graphite. From these data Gupta et al.[28] conclude successful intercalation of a highly ordered compound of C_{60} intercalated graphite.

‡Albeit they claim to use graphite they do use exfoliated graphite. But these considerations are not important at present, but will be discussed later on.

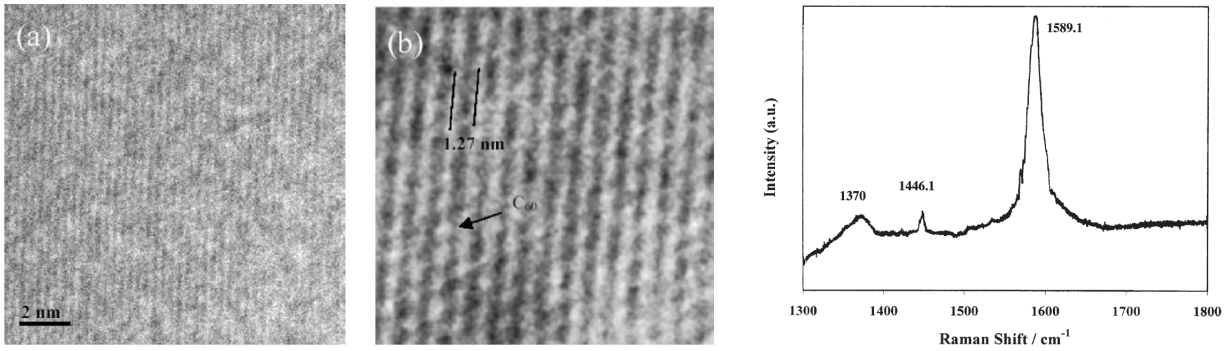

(a) **(b)** **(c)**

Figure 2.8: Results obtained by Gupta et al.[28]. **(a)** HRTEM image of graphite. **(b)** HRTEM image of stage-1 C_{60} intercalated graphite, with a individual C_{60} molecule marked by the arrow and the interplanar distance measured to 1.27 nm. **(c)** Raman spectrum of stage-1 C_{60} intercalated graphite, showing a small D peak around 1370 $c\text{m}^{-1}$, a down shifted C_{60} peak at 1446.1 $c\text{m}^{-1}$ and a up shifted G peak for graphite at 1589.1 $c\text{m}^{-1}$.

The main part of the experiments in this project will build on these experiments, in the attempt to produce a 2D all-carbon semiconductor. The results will be presented and discussed in section 5, where the results obtained by Gupta et al.[28] will be more critical reviewed, partially based on the results obtained in this project.

2.4.2 Potassium and C_{60} co-Intercalated Bilayer Graphene

Another approach towards C_{60}-intercalated graphite, is through an intermediate product of potassium intercalated graphite, C_8K. This were demonstrated by Fuhrer et al.[23] in 1994. The C_8K precursor was synthesised by two-zone thermal intercalation of potassium[58]. The two-zone method is characterized by two connected chambers, one containing the potassium and one the graphite. Heating the chambers controlling the temperature gradient between the two sides, the stage number of the GIC can be controlled with high precision, as is is temperature dependent[58]. For the stage-1 GIC the temperature different should be hold at a minimum, but non-zero to avoid to much adsorption on the surface of the graphite[17]. The resulting structure with stoichiometry $C_{32}K_4C_{60}$ were prepared by immersing the C_8K precursor in a 80°C saturated solution of C_{60} in dry benzene. The proposed arrangement of the potassium atoms and C_{60}-molecules in the interlayer sites of the graphite can be seen in figure 2.9b. Fuhrer et al.[23] only conduct transport characterization of the synthesized structure. These measurements showed that the sample were superconducting after annealing, with a transition temperature of 19.5 K, close to that of K_3C_{60} structure. Before annealing of the sample, the sample showed no sign of superconductivity above 4.2 K. They postulate that the C_{60} and benzene co-intercalate into C_8K precursor, and only upon removal of excess benzene a superconducting phase is formed. The relative high resistivity below the transition temperature, not going to zero, is assigned to only fractional superconductivity in the sample.

The measured superconductivity was predicted by Saito and Oshiyama[75] around the same time as the experiments. The calculation on the electronic band structure for $C_{32}K_4C_{60}$, is presented in figure 2.9a. It is seen that the band structure is similar to that of pure C_{60} GIC, except that the Fermi

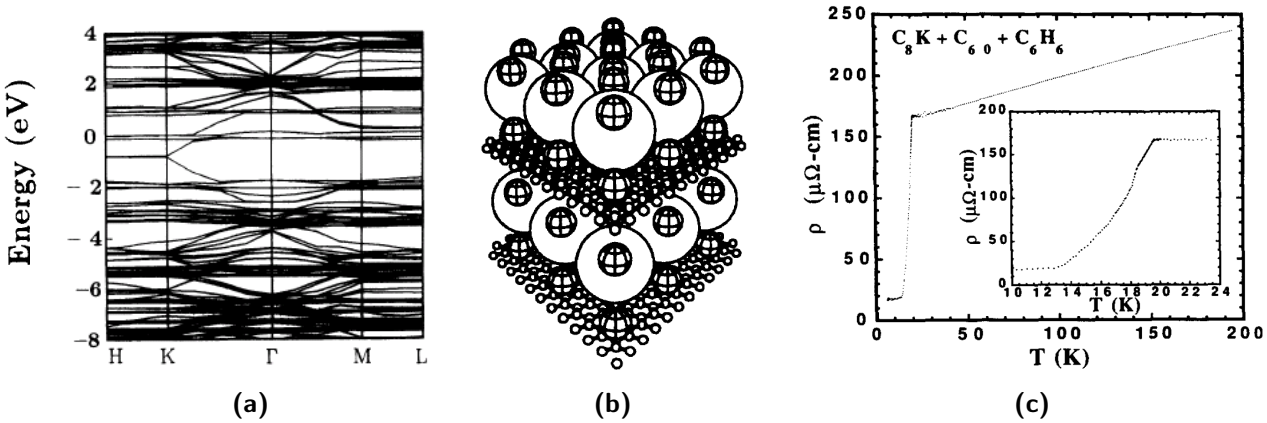

Figure 2.9: The GIC with stoichiometry $K_4C_{60}C_{32}$. **(a)** Electronic band structure calculation by Saito and Oshiyama[75] **(b)** Suggested arrangement of the potassium atoms (small decorated spheres) and C_{60}-molecules (large open spheres) in the graphite. Adapted from Saito and Oshiyama[75]. **(c)** Low temperature measurement by Fuhrer et al.[23] on the GIC, showing superconductivity with transition temperature, $T_c = 19.5$ K.

energy lies around the original t_{1u}-level from the C_{60}-molecule. This is the same effect seen in the superconducting alkali metal intercalated C_{60} crystal, M_3C_{60}, which can explain the similar transition temperatures.

Fuhrer et al.[23] argue that the seen superconductivity indeed arises from the intercalation product and not a K_3C_{60} phase in the sample. The postulate is that C_{60}-molecules probably would form K_6C_{60} when reacting with potassium in excess, which is an insulating phase[2;88], and not the superconducting K_3C_{60} phase. Furthermore they state that it is unlikely that a K_3C_{60} phase would account for the reproducibility they observe for all their samples. To confirm whether the superconductivity is due to a K_3C_{60} or $C_{32}K_4C_{60}$ phase they state that XRD and Raman measurements were in the making. These measurements are a necessity for eliminate either of the two structures. Unfortunately these measurements were never published.

The second part of this thesis will build on these findings, with focus on easing the intercalation of C_{60} into bilayer graphene through the intermediate product C_8K_3. The results obtained will be presented and discussed in section 5, and compared to the results obtained by Fuhrer et al.[23].

Chapter 3

Experiments

The experimental part of the thesis is presented to give an overview of techniques used in the attempt to prepare C_{60} intercalated bilayer graphene and the experimental difficulties encountered. The synthesis of C_{60} intercalated bilayer graphene, is a two-step process, namely production of bilayer graphene on wafers and the intercalation of C_{60}. The production of co-intercalation of potassium and C_{60} into BLG, is done by preparing the C_8K-precursor for the C_{60}-intercalation. For further details see appendix A, which is a step-by-step presentation of the optimized experimental procedures.

3.1 Basic Device Fabrication

Before the intercalation experiments, devices containing BLG sheets contacted by electrodes are produced. The idea was to produce in-plane electrodes on a SiO_2 wafer and then deposit graphene/graphite on-top. The details are presented below.

3.1.1 Bottom Electrode Production

Bottom electrodes were produced in two different ways. Either optical lithography, for which shadow-masks were designed using the software Clewin 4[86] and produced by Delta Mask[47]. Or electron beam lithography (EBL), where design files were produced with the software DesignCad 3D Max[33].

Photo-resist (or PMMA for EBL) were spin cast on silicon wafers with 285 nm layer of SiO_2 (the optimized oxide layer thickness for making graphene visible in an Optical Microscope, see section 4.1 for further details). After lithography the wafers were etched with a hydrofluoric acid etching mixture, provided by Sigma Aldrich[78], with a well-known etching rate. An E-gun metal evaporator was used for metal deposition, and the photo-resist was lifted-off leaving behind the etched down electrodes. Figure 3.1 is a schematic representation of the bottom electrodes production.

The electrode metal chosen was Platinum as its electrical properties are expected to be more stable than e.g. gold, after exposure to elevated temperatures for longer time (600°C for up to two weeks was needed for the intercalation synthesis[28]). The metal to SiO_2 adhesion was increased by deposition of a thin layer (5 nm) of Titanium prior to Pt. Picture 3.2a shows the final results, including the designed coordinate system, with the light areas being the Pt electrodes and the dark blue SiO_2.

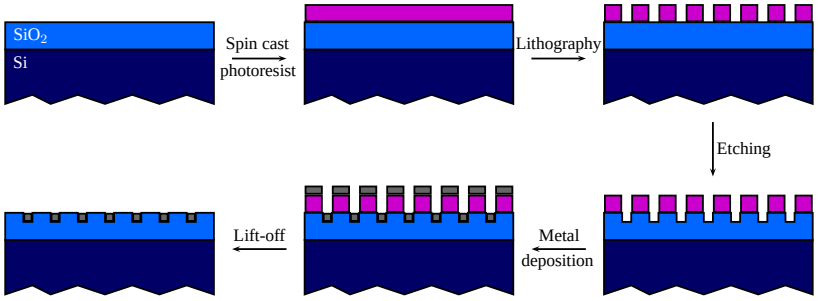

Figure 3.1: Schematic of the bottom electrode production and the different production processes used, being in right order; photoresist deposition, lithography, ething, metal evaporation and lift-off.

3.1.2 Pristine Bilayer Graphene

A wafer prepared as described above, is cleaned with acetone, methanol and IsoPropyl Alcohol (IPA), and ashed for 5 minutes in a plasma oven. Deposition of graphene on the wafer is done using the technique developed by Novoselov et al.[59], where tape is used to mechanical cleave flakes of natural graphite. The number of graphene layers per flake is reduced by repeatedly sticking together and peeling off the tape. The hopefully few layer graphene sheets can be transferred to the wafer, simply by putting the graphene covered side towards the wafer. The tape can be peeled off by heating the wafer to 70°C until the tape is released, leaving behind a minimal amount of glue on the sample.

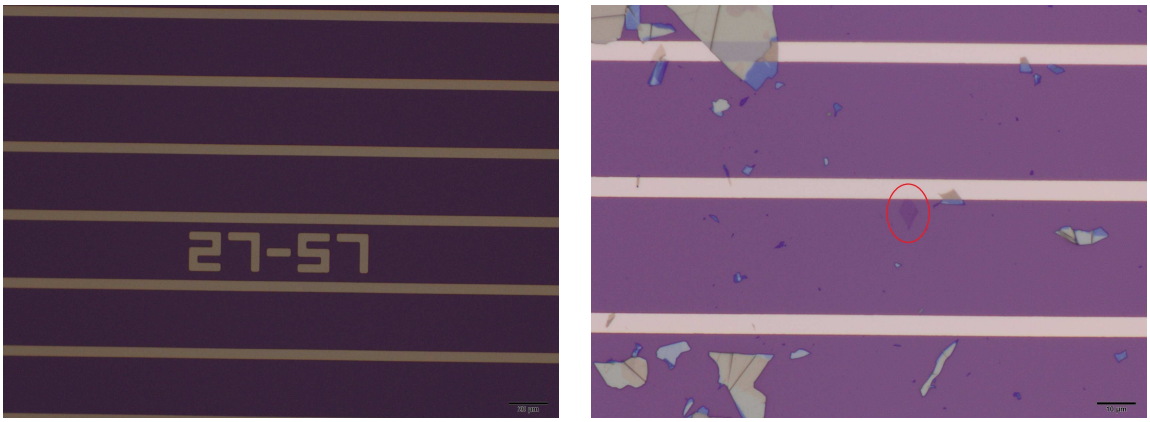

(a) **(b)**

Figure 3.2: Sample design and preparation. (a) Bottom electrodes and coordinate system. Dark areas are SiO_2 and light are the Platinum electrodes. (b) An example of a (small) bilayer graphene sheet, marked by the red circle, visible on SiO_2 and invisible on Pt. Pictures are taken with an Olympus optical microscope.

3.1.3 Expanded Bilayer Graphene

In order to ease the future intercalation step, the graphite interlayer distance was attempted increased, by preparing expanded graphite. It is reported that treating natural graphite with a mixture of sulphuric acid and nitric acid (4:1) for 16h, followed by a shock-heat-treatment ($1050°C$ for 15s) produce expanded graphite[13]. As this acid mixture is known to dissolve some noble metals it was replaced with fuming sulphuric acid (oleum) as the bottom electrodes consisted of noble metal platinum. Further-

more is H_2SO_4 a known intercalant in graphite[3], and hence the treatment with the highly concentrated sulphuric acid were expected to give similar results as the acid mixture. However it turned out impossible to do the acid intercalation on a substrate as intercalation between the graphene sheets and the surface resulted in almost all sheets washed off or was dissolved in the solution.

After these initial results, the acid treatment was conducted prior to deposition on the substrate. This was done by soaking natural graphite in oleum for at least 12h, followed by rinsing in millipore water. Attempts towards mechanical cleave the acid treated graphite with the tape technique were unsuccessful, as the graphite did not stick to the tape, indicating change in the surface chemistry. This and the observation that the acid treated graphite kept sticking to the metal tweezer, could indicate charges on the surface. Further indication of successful intercalation (or at least some kind of reaction), was the weight of the graphite pieces after acid treatment, which approximately doubled.

The vain attempt of wafer depositing the acid treated graphite, inspired the production of expanded graphite prior to wafer deposition. The initial hope of doing the expansion of the graphite after deposition on wafers was that a thickness increase of the graphite sheets could be detected using AFM, see section 4.2. Instead was the acid treated graphite heated to 600°C for 1 min in a nitrogen atmosphere. Expansion of the graphite flakes were observed as the graphite grew into a worm-like structure (referred to as expanded graphite). Deposition of the expanded graphite with the tape technique was possible, indicating that the before expected charges in the acid treated graphite vanished. Further discussion and results on the different graphite samples in presented in section 5.

3.2 Synthesis of C_{60} Intercalated Bilayer Graphene

After production of BLG samples, the experiments on C_{60} intercalation could be started. The intercalation process used in this project is highly inspired by the work by Gupta et al.[28].

3.2.1 Intercalation

The graphene sheets prepared as described above and C_{60} powder, were put in a quartz ampoule (dimensions $1x10$ cm). The ampoule was evacuated (for atleast 1 hour) using a turbo-pump, reaching a vacuum $< 10^{-5}$ $m$bar, see figure 3.3b for the turbo-pump setup. When a satisfactory high vacuum was reached the ampoule was sealed using a oxy-propane burner bought from Arnold Gruppe[27], see figure 3.3a for the sealing process. The sealed and evacuated ampoule containing the graphene covered wafer and C_{60}-powder was heated to 600°C for two weeks. Removal of excess C_{60}-molecules adsorbed on the surface of the wafers, were attempted with either heat treatment in a continuous nitrogen flow or dispersion in acetone followed by drying the wafer at 80°C to remove excess acetone.

Experiments with C_{60} intercalation into expanded graphite were conducted, in the same way as described above.

(a) **(b)**

Figure 3.3: Quartz ampoule sealing setup. **(a)** Close-up of the quartz burner sealing a pumped down quartz tube. **(b)** An overview of the experimental setup, including the quartz burner, turbopump and adapter for the quartz tubes.

3.3 Synthesis of C_{60} Intercalated Bilayer Graphene from C_8K Precursor

Another approach towards C_{60} intercalated bilayer graphene, synthesizing the structure $C_{60}C_{32}K_4$, was suggested. The idea of using potassium intercalated BLG, C_8K, as a precursor for C_{60} intercalation, was obtained from Fuhrer et al.[23]. The intercalation of potassium is carried out as described by Nixon and Parry[58]. Apart from the solution based intercalation suggested by Fuhrer et al.[23], an alternative approach where all intercalation processes were done thermally was suggested.

3.3.1 Intercalation of Potassium

A quartz tube was prepared with a BLG sample, along with a small piece of solid Potassium (~ 0.03 mg). The otassium was washed with heptane to remove paraffin and the oxide covered parts was cut away. The quartz tube was pumped down to a pressure of approximately 10^{-6} $m$bar, and was sealed off with an oxy-propane burner. The sealed quartz tube was heated to 300°C for three hours, which is reported to yields a stage-1 intercalation product between potassium and graphite. For intercalation of graphite the stage-1 product can be verified by the graphite changing color from gray to gold. No temperature gradient was induced while doing the intercalation as only stage-1 compounds was desired.

In stead experiments on removing potassium adsorb on the wafer, were done by creating a thermal gradient inside the sealed quartz tube, after the intercalation experiment was conducted. The part of

quartz tube containing the wafer was put on a heating plate set to 100°C, hopefully not resulting in de-intercalating of potassium, only desorption.

3.3.2 Solution Based Intercalation of C_{60} into C_8K-precursor

A saturated solution of C_{60} in dry benzene was prepared. The saturation can be verified by the strong purple color of the solution. The produced C_8K precursor on wafer was immersed in the solution and heated to 80°C for 24 h. Fuhrer et al.[23] report that the samples needs to be annealed in order to remove excess solvent, and measure superconductivity. Due to different problems, which will be discussed in chapter 5, this were never done, but should be kept in mind if the encountered problems are solved, and transport measurements is conducted.

3.3.3 Thermal co-Intercalation of C_{60} and Potassium

Another approach towards the $C_{60}C_{32}K_4$ structure was attempted. A sealed quartz tube containing C_{60}-powder, potassium and a graphene wafer sample was prepared. The sealed quartz tube was first heated to 300°C for three hours to intercalate the potassium and expanding the BLG/FLG sheets. Afterwards was the quartz tube heated to the 600°C for the 2 weeks, needed for the C_{60} intercalation to take place.

Chapter 4

Characterization Techniques

Throughout the course of the thesis a variety of techniques were used, namely Optical Microscopy, Atomic Force Microscope (AFM), Conducting AFM (CAFM), Raman Spectroscopy, Scanning Electron Microscopy (SEM) and X-ray Diffraction (XRD). Below are a short introduction to every technique and a description of how the data manipulation was carried out.

4.1 Optical Microscopy

Optical microscopy is optimal for the initial search for bilayer graphene deposit on SiO_2/Si wafers. Even though few layer graphene sheets are transparent in visible light, they can be seen in the optical microscope with careful choice of wafer. The wafer of choice is silicon with 285 nm of oxide layer. This is due to a weak interference-like contrast between graphene and the SiO_2 layer, compared to an empty Si wafer. Hence the thickness of the oxide layer is very important and many experiments have been conducted to optimize the contrast[8;24]. Thus all wafers used in this project have the optimal 285 nm thick SiO_2 layer. Figure 3.2b is a typical example of a BLG sheet visible on SiO_2 but invisible on the Pt electrode.

Non-destructive measurements and the possibility to search large wafer areas for graphene sheets relatively fast are the biggest advantages of the optical microscope. The disadvantage is that few conclusions can be made from the pictures, and as such the method is mostly relevant as a sheet detection tool.

4.2 Atomic Force Microscopy

The Atomic Force Microscope (AFM) is characterized by the use of a mechanical probe to scan surfaces for nano scale information about the morphology of the surface[7].

Different modes of operation can be employed when using AFM, some of these are: Contact mode, non-contact mode and the intermediate tapping mode. In all of the modes it is the atomic forces between tip and surface that are registered, or more correctly the Van der Waal forces modelled by

the Lennard-Jones potential[36] equation 4.1.

$$U(r) = 4\epsilon \left[\left(\frac{\sigma}{r}\right)^{12} - \left(\frac{\sigma}{r}\right)^{6} \right] \tag{4.1}$$

Where ϵ is the depth of the LJ potential well and σ is the distance between tip and sample where the potential is zero.

All measurements in this project are conducted with tapping mode, where the vibrating cantilever is placed in exactly such a height that the tip taps the surface with a specific resonance while scanning. The resonance of the cantilever is kept constant by changing the distance to the surface, correcting for either height differences or change in surface stickiness. Two AFM apparatus were used, one being a Veeco Multimode 8 and the other a Veeco Dimension Icon. The difference between the quality of the images obtained by the two types of AFMs is not significant hence will not be distinguished.

All AFM data processing was done with the program Gwyddion[56]. Figure 4.1a is an AFM picture of the sheet seen in figure 3.2, while figure 4.1b is a line height profile from the SiO_2 area to the graphene, with the height of the bilayer graphene flake estimated by a step function to approximately 1.2 ± 0.1 nm. AFM pictures presented throughout the thesis are all manipulated, with built-in tools in the Gwyddion software, correcting for data acquisition induced defects, e.g. non-planar surfaces.

The highest advantages of using an AFM as the main characterization tool in this project, are unlimited access (I was one of very few users) and the relatively immediate and direct indication of intercalation. As a rule of thumb, the height of a SLG on SiO_2 is approximately 1 nm and the interlayer distance in MLG (and graphite) is approximately 0.3 nm. From both the theory and the experimental work, it is expected that the interlayer distance increases to ≥ 1 nm after C_{60} intercalation, increasing the thickness of the graphene sheet significantly, see section 2.4.

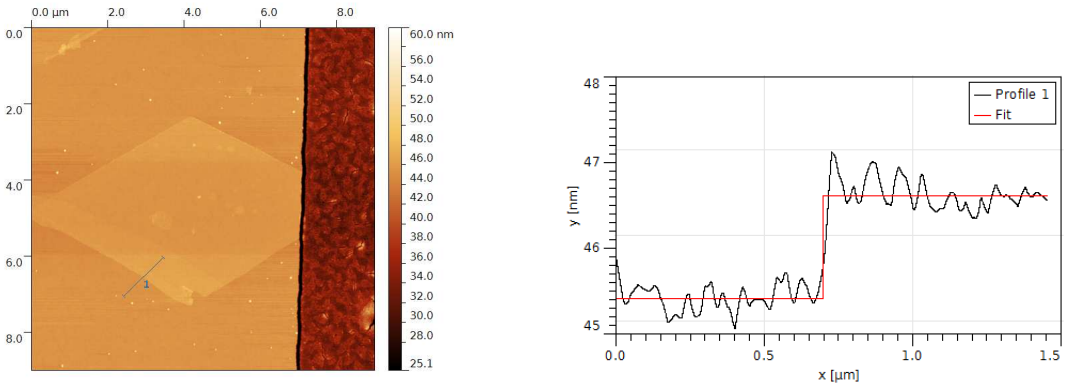

Figure 4.1: **(a)** AFM picture of the sheet seen in 3.2. The orange part is the SiO_2 surface and the darker more rough surface is the Pt electrode. **(b)** Height profile of the line seen in (a). Height estimated by step function fit to 1.2 ± 0.2 nm.

4.3 Conducting Atomic Force Microscopy

For electrical measurements, an AFM is modified so the tip acts as an electrode. A schematic overview can be seen in figure 4.2. The advantages of this technique are the relatively fast data acquisition* and the possibility of probing the sample at different sites.

Special AFM tips made conductive with a coat of platinum, produced by μMasch [55], were used for the conductance measurements. A voltage supplier (Keithley 2400 Source-Meter) was connected as seen in figure 4.2, with a 1 $M\Omega$ resistor before the tip, minimizing the current passing through. The conducting AFM tips could not tolerate a current higher than 100 nA. The current was measured with a Keithley 6514 System Electrometer, with a measurement sensitivity of ± 100 aA. The experimental setup system was controlled in Labview 2010 [34]. All I-V-curves in this project were taken with a bias voltage interval from -5 mV to 5 mV in 200 steps.

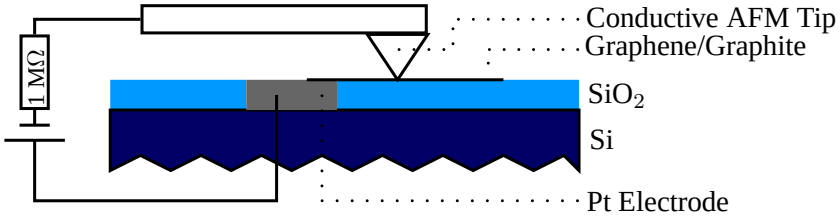

Figure 4.2: Schematic overview of the Conducting AFM setup. The system consists of a conductive AFM tip in contact with the sample. A voltage supplier is connected with a 1 $M\Omega$ resistor before the tip, minimizing the current set through the tip. By engaging the tip at different sites of the sample I-V curves can be conducted.

Figure 4.3 shows CAFM data where the AFM tip is engaged and in contact with a bottom electrode, basically short circuiting the system. Figure 4.3a shows raw data from 7 voltage sweeps from -5 mV to 5 mV. It is seen that the I-V curve in this interval is linear and obeys Ohms law, and hence is a conductor as expected. Data manipulation is done by taking the average of all the sweeps, followed by a linear fit to this curve, the result of which can be seen in figure 4.3b.
The CAFM data presented in the results chapter contains measurements on different sites, twice on the electrode and a couple of times on the sheet. The results are collected and presented in a table similar to table 4.1. The average conductance is read directly from the linear fit as the slope, while the resistance is calculated by taking the inverse of the slope. The resistance measured is a serial resistance, originating from the experimental equipment, and is on its own not informative. Taking the difference between a short circuit measurement (electrode) and one on a sheet, could potentially give information on the electronic properties of the sheet. But as will be discussed below and in further details in section 5 this is not as straight forward as first expected.

Conductance measurements on BLG in contact with an electrode was not expected to alter the total resistance within the detection limit, as the BLG has high charge carrier mobility. Measuring on a C_{60}-intercalated BLG, where a band gap is introduced to the BLG, hopefully lowers the conductance enough to be detectable. The precision of the equipment and the averaging over several sweeps should give good statistics on the measurements, which for individual measurements is the case. The linear fit

*Within half an hour, a sample can be mount and measured

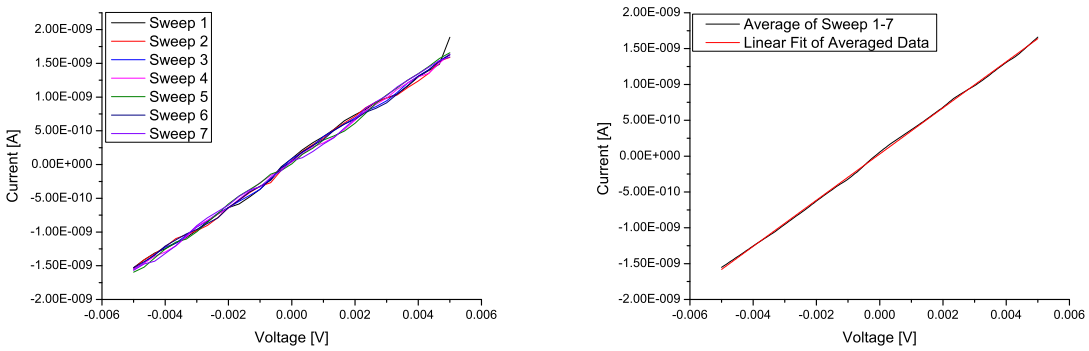

(a) **(b)**

Figure 4.3: CAFM measurement on a Pt electrode. **(a)** The raw data from 7 voltage sweeps from -5 mV to 5 mV. The I-V-curve shows linear characteristics corresponding to a conductor, as expected for the Pt electrodes. **(b)** Average of the 7 sweeps in (a) and a linear fit to this curve.

has a standard error to the slope of $4.6 \cdot 10^{-4}$ μS, or a precision to the third decimal. However as will be seen in the section 5 the variation from measurement to measurement on the same sample varies with the first decimal. This variation will be discussed in further detail when the relevant data is presented, thus only a summary of the argument is given here. The possibility of CAFM tip topology changing after having been engaged into the sample is relatively high, which might change the contact area between tip and sample, hence the contact resistance. Also local variations in the sample might alter the resistance undesirably. Thus a significant change in the resistance between two subsequent measurements on the same sample at the same place with the same tip might occur. The difference is seen to be larger than the precision on individual measurement. Hence the standard error will only be presented in the tables for good measure, but as such is not informative as large variations between each engagement makes the extraction of sheet resistances lower than $0.1M\Omega$ impossible.

Table 4.1: Data from the linear fit in figure 4.3b

Avg. Conductance	Avg. Resistance
$0.3220 \pm 0.0005\mu$S	$3.106 \pm 0.005M\Omega$

4.4 Raman Spectroscopy

Raman Spectroscopy is a strong tool when investigating the physical properties of a FLG-sheet, as the so-called D and G peaks are highly dependent on the number of layers, doping, disorder and phonon distribution. In order to understand this dependency, a deeper knowledge of Raman spectroscopy on graphene is needed, but initially general Raman scattering will be introduced.

Irradiation of matter with monochromatic light can lead to different processes, i.e. the light being transmitted, absorbed or scattered. The Raman process is in general that of inelastic scattering of monochromatic light with matter[62], as opposed to Rayleigh scattering where the light frequency remains unchanged. The change in frequency is due to the excited electron inducing a phonon at the

expense of energy.

For Raman spectroscopy the light is usually in the visible, near infra-red or near ultraviolet range, depending on the material measured. All Raman spectra in this project were conducted with a wavelength of $\lambda = 514$ nm and a spot size of roughly 1 μm.

Raman spectroscopy on graphene was early discovered to be a strong tool when characterizing the properties of the material[22]. Even though Raman spectroscopy is a very popular technique, misinterpretation and disagreement of peak assignment is still very common in the literature[21]. The paper by Ferrari and Basko[21] from 2013 reviews the latest development in Raman spectroscopy on graphene and proposes a self-consistent terminology, in order to minimize peak interpretation mistakes in the future. All Raman data in this thesis will be processed within the terms of this terminology.

The processes giving rise to Raman peaks can be visualized by a model as seen in figure 4.4b. Here the origin of five different peaks are illustrated by different scattering processes. In the suggested process responsible for the G peak, an electron is excited by absorption of a photon. The excited electron relaxes back by emission of a standing phonon and a photon. In the presence of defects, the wave vector of the emitted phonon can be non-zero, as the electron can scatter back on defects, as illustrated for the D and D' peaks. Hence the relative intensity of these peaks gives information on the number of defects in the graphene sheet. Lastly a two phonon process where the conservation of momentum is fulfilled by emission of two phonons with opposite wave vectors, leads to two peaks, namely 2D and 2D'.

Raman data are plotted in terms of the Raman shift, defined as the difference between the incident and scattered photon, and are by historical reasons given in wave numbers [cm^{-1}]. Raman peaks can be assigned to specific processes, with the most important being the E_{2g} responsible for the G-peak, see figure 4.4c for a visualization of the phonon mode.

A typical Raman spectrum for pristine graphene can be seen in the upper part of figure 4.4a, while the lower part is from a graphene sheet with many defects. Such Raman spectra gives immediate information about quality and number of layers. The D peak is due to disorder in the sheet, independent on defect types, being e.g. missing atoms and edges, as this peak originates from Raman processes only conserving momentum by scattering on defects. The absence of the D peak in the pristine graphene indicates high purity. The relative ratio between the G and 2D peak, gives us information about the number of layers. For graphene the 2D peak is more intense, whereas for three layers and up the G peak dominates. For BLG the ratio is approximately one.

Figure 4.4d shows a Raman spectrum of a BLG sheet (the same sheet as seen in fig 3.2). Here it is indeed seen that the G and D peak are present in a 1:1 ratio, confirming that the sheet consist of two layer of graphene in a Bernal stacking. Furthermore the very weak D peak indicate the high quality of the graphite used. Informations on the peak, such as position, standard error and FWHM, are extracted by fitting a Voigt function, using the software OriginPro[64].

4.5 Scanning Electron Microscopy

For higher resolution images than an optical microscope can produce, a Scanning Electron Microscope (SEM) was used. The high resolution is the biggest advantage of this technique, but the disadvan-

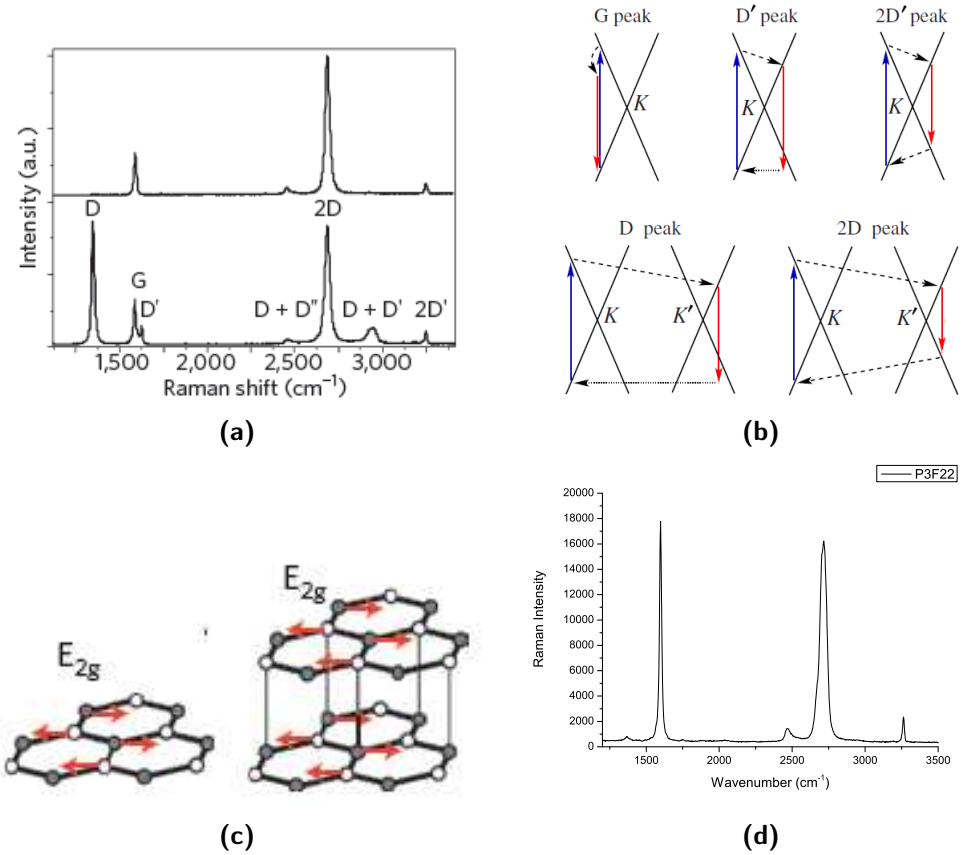

Figure 4.4: **(a)** Example of Raman spectra of high quality graphene (upper) and defected graphene (lower). **(b)** Proposed processes behind the peaks seen in (a). **(c)** The phonon mode responsible for the G peak. It is seen that this mode is active in the graphene. **(d)** Raman spectrum of bilayer graphene, showing the high quality of the graphene used in the project. (a) and (c) adapted from Ferrari and Basko[21], (b) Adapted from Basko et al.[5].

tages, where the most serious are the destruction of graphite and deposition of amorphous carbon by irradiation with the electron beam, minimizes the usability of this technique.

The principle behind a SEM is to take advantage of the wave-like nature of electrons, in a similar way as an optical microscope uses light. Figure 4.5a is a schematic representation of the principal behind SEM. Electrons are accelerated in the electron gun, from an electron source to an anode, and focused down trough some magnetic lenses. Before reaching the sample the electron beam passes through deflection coils, which can scan the beam over the sample and correct for astigmatism. Two options are available when acquiring the SEM picture, both Back-Scattered Electrons (BSE) and Secondary Electrons (SE) can be collected. All images in the project are recorded with BSE. Figure 4.5b is a SEM image of a piece of pristine graphite used in the project.

As the electron beam is destructive to carbon samples, low voltage imaging is preferable. All images in this thesis were taken with an acceleration voltage of 10 kV, which is not very low, but the minimum of the Jeol JSM 632OF apparatus used.

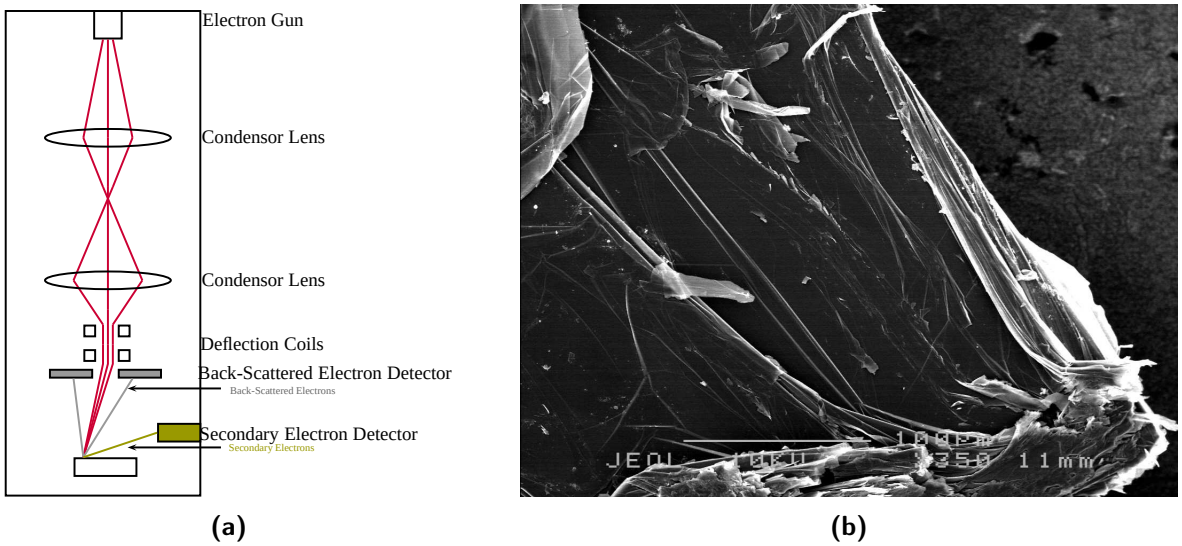

Figure 4.5: Scanning Electron Microscope **(a)** Schematic representation of the principle behind a SEM. An electron beam is focused by a couple of magnetic lenses, before reaching the deflection coils. The deflection coils correct for astigmatism of the beam and are responsible for scanning the sample. **(b)** A SEM picture of a pristine graphite piece. Image is produced by collecting the BSE electrons.

4.6 X-ray Diffraction

Change in the interlayer distance is a strong evidence of successful intercalation, as discussed in the AFM section. However the experiments with expanded graphite were all conducted before deposition onto a substrate, excluding AFM as a useful technique. Instead X-ray Diffraction (XRD) measurements on the graphite pieces was conducted. XRD is normally used for measuring the Bragg reflections from crystals, thus yielding information on the crystal structure and lattice parameters. In crystals the periodic lattice planes can be regarded as semi-transparent mirrors, which give rise to backscattering of an incident electromagnetic beam. Only at certain incident angels are the backscattered light in phase, giving rise to constructive interference. This can be described by Braggs law, eq. 4.2, saying that the incident wavelength, λ, equals the lattice plane separation, d, times sine to the incident angel, θ,

$$n\lambda = 2d\sin\theta \tag{4.2}$$

From this simple equation each diffraction peak in a XRD spectrum (which is given in terms of 2θ) can be contributed to a specific plane spacing. It is possible to assign each individual peak to a lattice plane, albeit very tediously, especially if the crystal structure is unknown and multiple crystal phases are present. As the technique was used for detection of intercalation, only the plane distance was of importance, hence crystal structure information will not be extracted from the XRD data.

The highly planar structure of graphite gives rise to one very prominent Bragg reflection from the (002)-plane, remembering the unit cell of graphite contains two atomic planes. The plane distance of 3.5 nm for pristine graphite would give a prominent peak at $2\theta = 26.6°$ with an x-ray wavelength of $\lambda = 1.54$ Å, as seen in figure 4.6. Other peaks present are due to reflection from other lattice

planes, but are as such not relevant for this thesis as intercalation would be visual by studying the (002)-reflection only. In figure 4.6 these peaks are not visible, due to the high intensity from the (002)-reflection, which also is the origin of the second peak seen, namely the second order of the (002)-peak. To analyse the peak, Voigt (combination of Gauss and Lorentz) functions are applied. The choice is dependent on the source but for the two kinds used in this project a Voigt distribution was suitable. The next section further describes the two different sources. The fitting was done with the software OriginPro[64], and the standard errors were hence extracted from these fits. The calculated standard error for the peak position was for many of the peak fits smaller than the precision on the specified x-ray wavelength. Thus for the peaks with fitted standard error lower than the apparatus precision, the uncertainty on position is based on the x-ray source and not the fit.

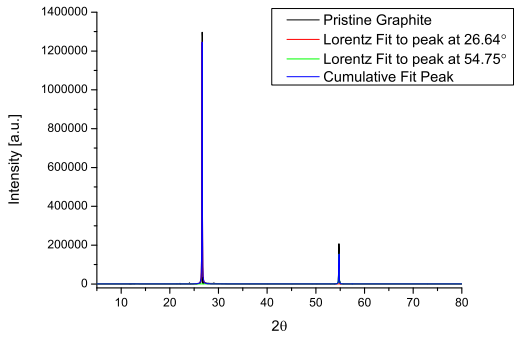

Figure 4.6: XRD data from pristine graphite. The high intensity peak at $2\theta = 26.64°$ is the (002)-reflection, while the second visible peak is the 2nd order of this peak.

The X-ray Sources

Two different types of x-ray sources were used for the diffraction measurements. One type was a Bruker D8 X-ray Diffraction system[10]. This x-ray source is a classic copper anode, which produces K_α radiation with $\lambda = 1.54$ Å. The principle behind the design can be seen in figure 4.7a. Electrons are accelerated from, in this case, a wolfram filament to a copper anode. When the electrons hit the copper anode, they are decelerated due to interaction with the nuclei, sending out electromagnetic radiation. This type of radiation is called Bremsstrahlung and is a broad spectrum of wavelengths. Two high intensity x-ray peaks are characteristic for copper, namely K_α and K_β. These two peaks originate from electron-electron scattering, where the high energy electrons hitting the copper anode kick out a K shell electron. Higher energy electrons then relax back to the vacant by sending out a photon with a very distinct energy. The nomenclature is as follows: The capital letter denotes what shell the core electron relaxes back into (K,L,..), whereas the subscript denotes whether it comes from the shell closets in energy (α) or 2nd closest (β) etc. By filtering away all other energies, a high intensity and low-energy-dispersive x-ray beam can be produced.

Other x-ray measurements were done in MaxLab Lund, beam-line 911-1 (Cassiopeia), by a student group following an experimental course on x-ray techniques, where I was fortunate enough that they used some of my GICs as course samples. The synchrotron source is a so-called wiggler, see figure

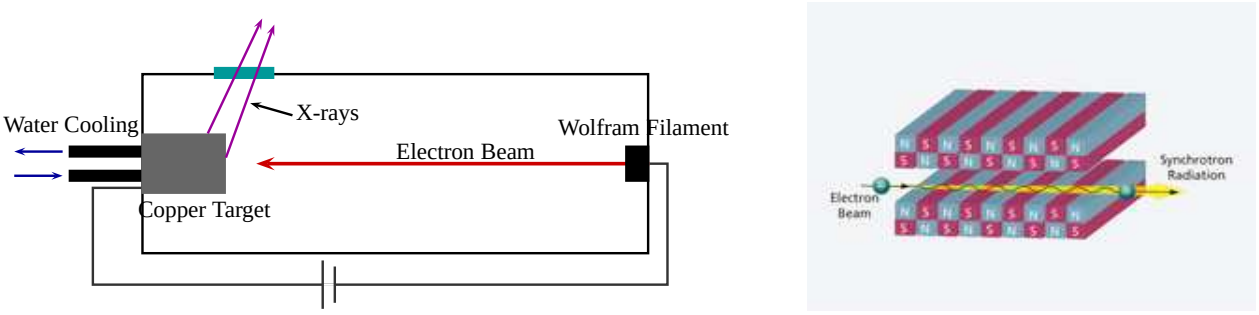

Figure 4.7: X-ray sources **(a)** Schematic representation of the principle behind a Copper anode **(b)** A wiggler x-ray source. A electron is accelerated in opposed magnetic field, emitting light under each acceleration. Picture adapted from: `http://www.psi.ch/media-/the-swiss-light-source-sls` - July 2013

4.7b. This source produces x-rays with a wavelength of 1.048 Å, by accelerating charged particles (electrons) through a series of opposed magnetic fields, emitting x-rays for every acceleration. The wiggler holds the advantage over, the normal copper anode, of producing a much higher intensity x-ray beam, hence having better resolution in the low angle regime. This makes the synchrotron source ideal when measuring on graphite intercalation compounds (GIC) with expected high interlayer distance.

Chapter 5

Results and Discussion

Chapter 5 begins with a description of some of the problems encountered while working on the project. Next the results obtained throughout the course of the project are presented and discussed. The result presentation is divided into three main parts, being thermal intercalation of C_{60} in few-layer graphene, C_{60} intercalation into bulk graphite and finally co-intercalation of Potassium and C_{60}.

5.1 Progress of the Project

The main objective of the project was to intercalate C_{60}-molecules in-between two graphene layers, but before these experiments could be conducted a intercalation system was build. The initial approach was to use a small vacuum chamber with a heating element inside, see figure 5.1a for a schematic drawing. The idea was to use the heating element to heat a graphene sample and C_{60} powder to the 600°C required for the intercalation inside the vacuum chamber. This setup never became operational due to a variety of things. First of all, the basic design had at least one major flaw, namely the continuous need for pumping. Hence it would be very tricky, if not impossible, to create the high C_{60} vapour pressure required for the intercalation to take place. Furthermore the chamber has a lot of leaking sites, e.i. only a vacuum of 10^{-1} $m$bar could initially be created. After three months of consecutive attempts to leak detect and seal, the chamber was finally satisfactory sealed for a test run of 7 days with the heating element powered up. After 5 of the 7 days, a leak appeared while heating to 600°C, and the electrodes and the heating plate oxidized and consequently died. It was not possible to repair the heating element, and this experimental setup was finally banned. After consulting the literature, where the usual approach was to pump down a quartz tube and seal it, a similar setup was build, see schematic in figure 5.1b. After 1 month where several gas burners and gas types were tested*, an oxy-propane burner with four nozzles from Arnold Gruppe[27] was chosen, see figure 3.3a. A turbo pump capable of creating a vacuum of $1 \cdot 10^{-6}$ $m$bar was used. Thus almost half way through the project the actual experiments were started.

*Quartz melting point is beyond the 2000°C, so specialized tools were needed before the experiments could be realized

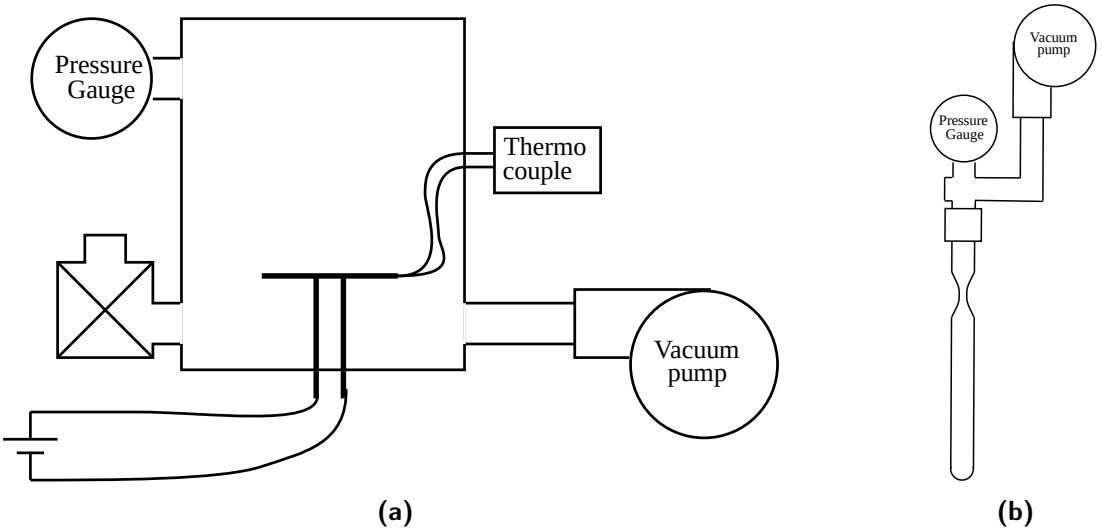

Figure 5.1: The two different experimental systems attempted build in the project. **(a)** The unsuccessful vacuum oven, consisting of a heating element controlled by a voltage supplier and a thermocouple. The vacuum was created with a vacuum pump and measured with a pressure gauge. **(b)** The successful setup, consisting of the quartz tube connected to a turbo pump, capable of creating a vacuum $< 10^{-5}$ $m$bar. The quartz tube can be sealed by an external gas burner.

5.1.1 Testing the Quartz Tube Setup

First step after completing the quartz tube evacuation and sealing setup, was to verify that a graphene sheet could survive the heat treatment, i.e. if the quartz tubes did indeed hold a high vacuum ($< 10^{-5}$ $m$bar). A tube containing multilayer graphene was evacuated and heated to 600°C for 2 weeks. Figure 5.2 shows the Raman spectrum taken subsequent to the heating. From the absence of a pronounced D-peak (around 1400 $c\text{m}^{-1}$ as discussed in section 4.4) it can be seen that no noteworthy disorder has been introduced to the multi-layered graphene sheet. If the quartz tube vacuum had been insufficient oxidization of the carbon atoms would have lowered the quality of the graphene, i.e. induced disorder in the form of breaking the highly conjugated system, see section 4.4. As this is not the case, it was concluded that the experimental setup was properly optimized, and the intercalation experiments were started. Unfortunately the access to the Raman spectrometer was limited so no Raman spectrum was obtained prior to the heating. It is therefore unknown whether the small disorder peak is due to the heat treatment or pre-existing disorders, see section 4.4.

5.2 C_{60} Intercalated Bilayer Graphene

The original idea of the project was to create a 2D all-carbon semiconductor with the in-plane transport characteristics of pristine graphene. As will be presented below this turned out unsuccessful, so alternative approaches towards intercalation of C_{60} into bilayer graphene were proposed, initial, however, the original carbon burger experiments are presented.

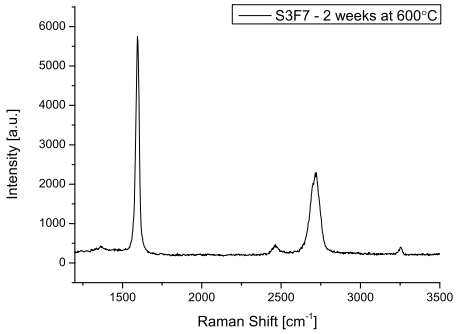

Figure 5.2: Raman spectrum of a MLG sample heated to 600°C for 2 weeks. A pronounced G-peak at 1594.6 $c\text{m}^{-1}$ and the 2D-peak at 2713 $c\text{m}^{-1}$ and only a small D-peak around 1400 $c\text{m}^{-1}$ verifies that the sample still is highly graphitic and has a minimum of disorder after the heat treatment.

5.2.1 Pristine BLG

Intercalation experiments were conducted by preparation of pristine graphene samples (both BLG and MLG) on Si/SiO_2-substrates, followed by thermal intercalation proposed by Gupta et al.[28]. Figure 5.3 are optical microscope images and AFM images showing a typical example of an attempted C_{60} intercalation into FLG, both pre- and post-intercalation attempt. Comparing the two optical images, the most significant change is on the Pt electrodes. After intercalation attempt the electrode surface seems more rough. These structures were not further investigated, but are most likely large cluster of C_{60}-molecules. Figure 5.3c and 5.3d are AFM images of the sheet pre- and post-intercalation attempt respectively. The indications of adsorption of material on the surface observed in the optical microscope images were confirmed by the AFM measurements. The large amount of material on the surface after the intercalation attempt complicated the data acquisition with the AFM, as the tip both got unstable from hitting big structures and from material adsorbing on the tip. This made imaging very difficult, and resulted in only small areas where the tip was stable, hence the small scan size after the C_{60} treatment. Figure B.1a is an AFM image of the same area as in 5.3d before cleaning. The cleaning processes will be introduced below. The height profiles, inset in 5.3c and 5.3d, reveals no significant change in height of the flake after the intercalation attempt. The measured heights were approximately 0.7 ± 0.2 nm both before and after intercalation. The 0.7 nm thickness here is not a SLG, as the height is measured on a SLG to FLG transition, e.i. the total number of layers in the FLG is ∼3LG, and should hence have increased to a thickness of > 3 nm for a stage-1 intercalation structure, see section 2.4.

Cleaning

From the initial intercalation experiments and the large amount of material on the surface, it was clear that some kind of cleaning process had to be developed and optimized, see e.g. figure B.1a showing the same area as 5.3c before cleaning. The first idea was simply to anneal the sample 60 min at 400°C in an inert atmosphere, which resulted in the surface structures seen in 5.3d. The C_{60}-molecules were expected to desorb from the surface at approximately 350°C[35], and as can be seen from the change

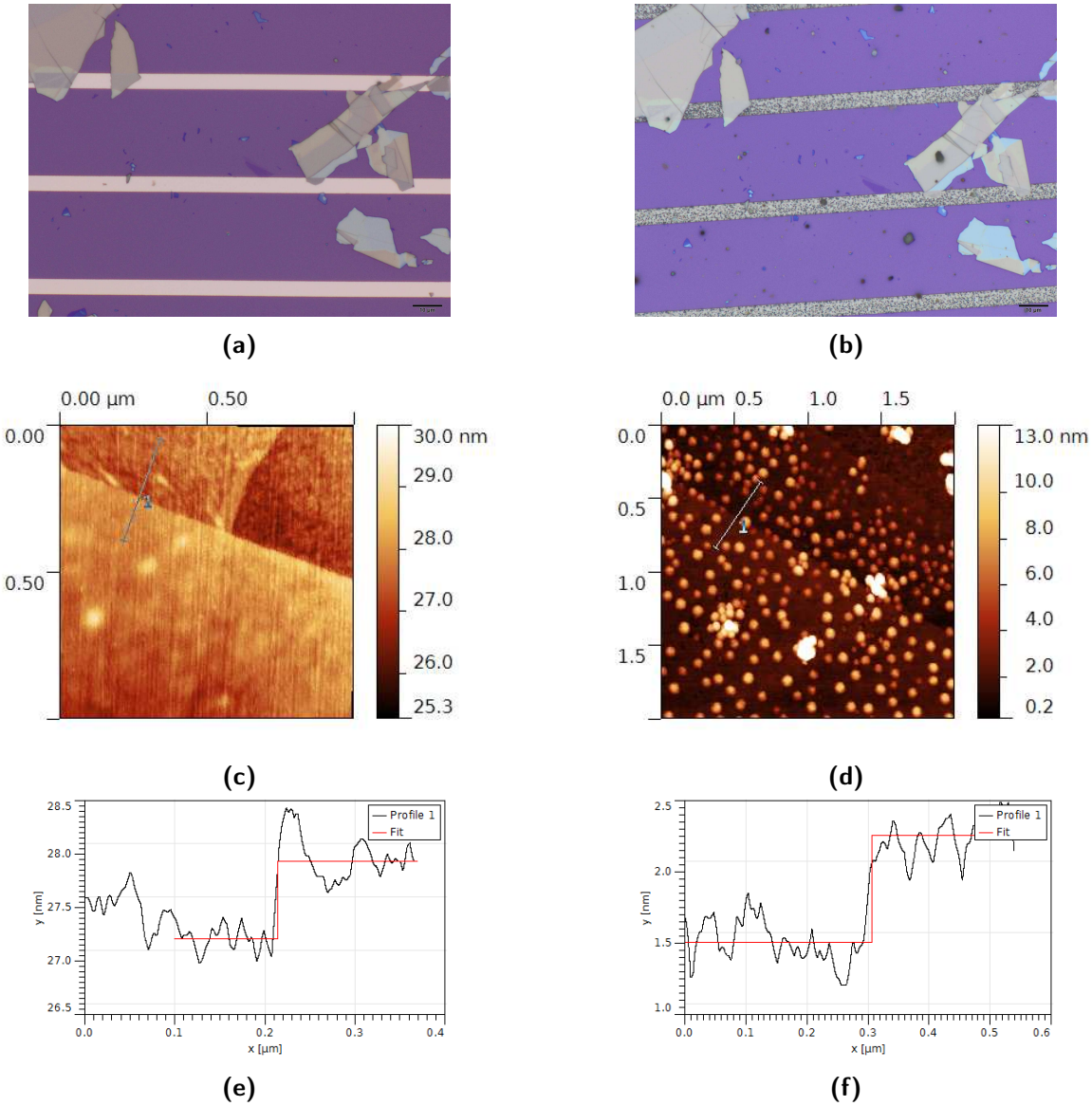

Figure 5.3: Optical microscope and AFM images of the initial experiments with a FLG sheet. **(a)** Optical microscope image of a FLG sheet prior to intercalation. **(c)** AFM image of the sheet, rotated $90°$ compared to the original scan direction. **(e)** is the line-profile marked in the (c) as line 1, showing a height of 0.72 ± 0.21 nm estimated by fitting a step function. **(b)** Optical microscope image after the intercalation. The most noteworthy change are the structures on the Pt-electrodes. **(d)** AFM image after the intercalation and after annealing. **(f)** The height profile shows no sign of intercalation, with a height of 0.71 ± 0.20 nm obtained from the step function fit. Many round shaped structures can be seen, probably being C_{60}-clusters.

in morphology, comparing the two AFM images, this does indeed seem as a reasonable assumption. The remaining clusters are expected still to consist of C_{60}-molecules, but further heating did not remove any more material. Next the sample was soaked in acetone, to hopefully remove any excess C_{60}-molecules, but after two soakings with no further change, see figure B.1b, the acetone approach was abandoned. As the heating seemed as the most effective way of cleaning, an attempt where the quartz tube was taken directly out of the hot oven and cooled rapidly in the air (instead of slow cooling inside the oven), showed to create a similar result (if not better) as the annealing. Figure

5.4d is an example of a sample undergone this treatment indicating less adsorbtion of material. It is highly likely that the quartz tube cool faster than the sample surface inside the tube, resulting in less material adsorbing on the sample due to an induced temperature gradient towards the sample.

Pristine MLG

The unsuccessful intercalation into FLG was speculated to be due to doping effects, e.i. the substrate p-doping the graphene, hence screening the charge transfer from the graphene to the C_{60}-molecules, making the heterostructure unfavourable. These thoughts and in general to rule out the possibility of other substrate effects hindering the intercalation, experiments with MLG on Si/SiO_2-wafers were conducted. The doping effect is completely screened after approximately 10 layers of graphene[43].

Figure 5.4 are optical microscope and AFM images of a MLG sheet pre- and post-intercalation. AFM data from the thick part (yellowish contrast in figure 5.4a), showed no evidence of intercalation. The data are shown in figure B.3 which shows a height of the sheet before intercalation attempt of 7.05 ± 0.61 and after 6.29 ± 0.47, which within the standard error are equal. From this it was concluded that further processing of the graphite pre-intercalation was necessary, as it was expected that the original interlayer distance of 3.3 nm was to small for the C_{60} to intercalate into, e.i. to high a C_{60} vapour pressure was required.

Before describing further measurements, a few observations from the experiments on pristine graphene are presented. The flake seen in figure 5.4 indicates a 1 nm increase in thickness of the thinner part (blueish contrast), see inset in figure 5.3c and 5.4d. The increase could be due to intercalation of a single layer of C_{60} molecules (probably in the SiO_2/graphite interface) or a C_{60} monolayer on top, but nothing can be concluded. From other samples, the creation of small islands of C_{60} on-top of graphene were seen (see an example in figure B.2), but these do not show such a smooth surface as seen in 5.4d. Another reasonable explanation which can not be ruled out is oxidation of the FLG sheet or a mis-calibrated AFM. A Raman spectrum could give further information on which of the above explanations are most likely. A D peak would indicate oxidation, while a shift in G peak would indicate doping of the graphene from interaction with C_{60}-molecules. This measurement was never conducted as the access to the Raman spectroscope was limited and other samples were of higher priority.

5.2.2 Expanded BLG

Realizing the difficulties of intercalation into pristine FLG, inspired a very thorough investigation of the literature to reveal exactly what kind of graphite Gupta et al.[28] did use. They state to use the type of graphite developed by Chen et al.[13]. The graphite developed by Chen et al.[13] was referred to as graphite worms, and was produced through an intermediate step called graphite nano-sheets. Graphite nano-sheets are pristine graphite which get expanded by treatment with a mixture of nitric and sulphuric acid followed by heat treatment. The nano-sheets which basically is a powder consisting of MLG sheets, preserve interlayer distance of 3.3 Å[13]. The same applies to the graphite worms, which are exfoliated graphite nano-sheets and hence is expected to be a powder mainly consisting of FLG sheets. As the interlayer distance is, to all practical means, constant, it was decided to start with the

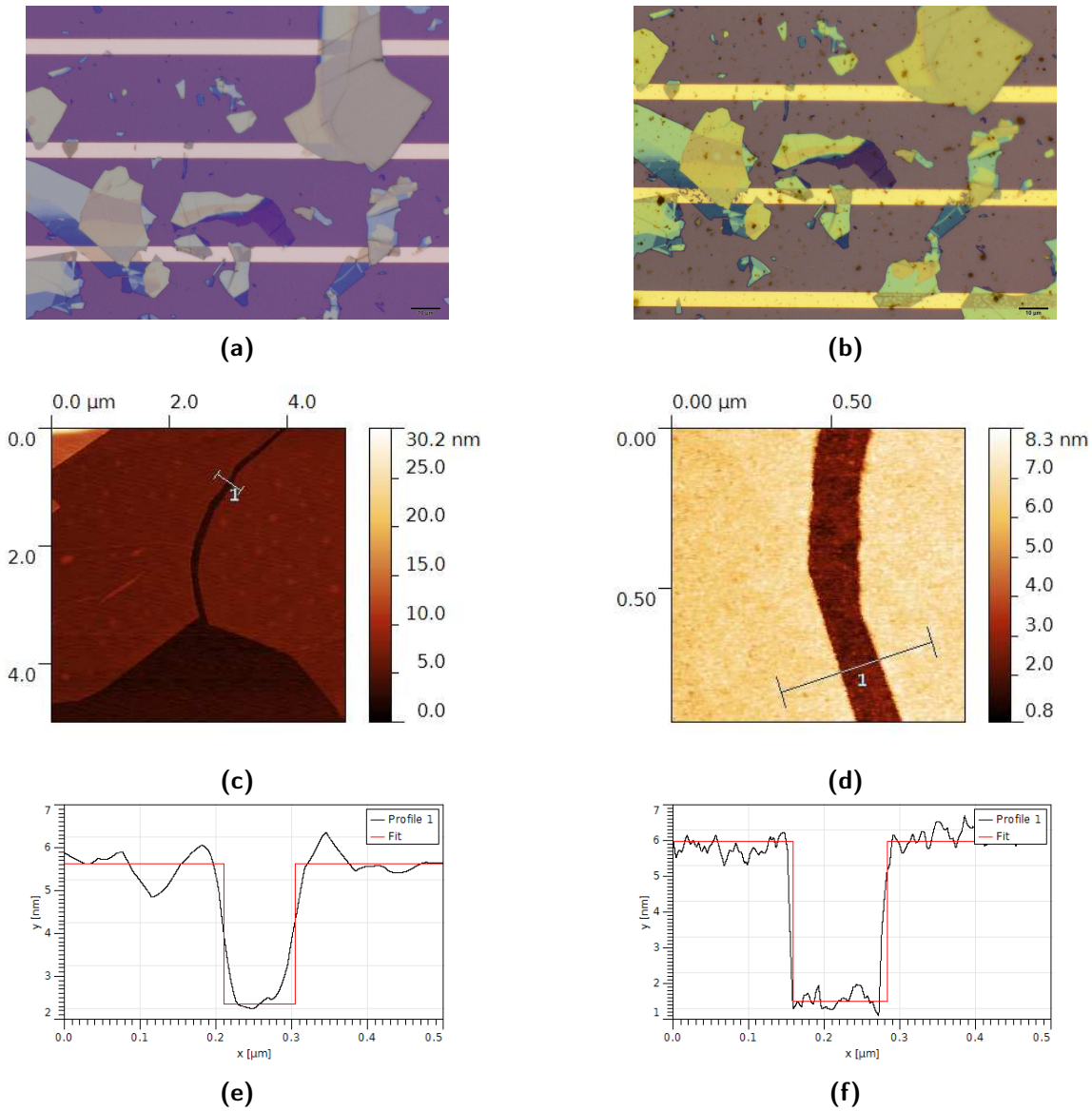

Figure 5.4: Optical microscope and AFM images of the experiments with a MLG sheet. **(a)** Optical microscope image of a MLG sheet prior to intercalation. **(c)** AFM image of the sheet. **(e)** is the height-profile of the line marked in the image as line 1 and the height is estimated with a step function to 3.26 ± 0.42 nm. **(b)** Optical microscope image after the intercalation. This time no features are seen on the Pt-electrodes, compared to 5.3b, which may be due to the faster cooling of the quartz tube. **(d)** AFM image after the intercalation and after annealing. **(f)** The height profile in the inset shows a height of 4.47 ± 0.39 nm and hence an increase of approximately 1 nm compared to (e), which is not enough for a stage-1 intercalation product, but comparable to one layer of C_{60} most probably in the SiO_2/graphite interface.

acid treatment. Instead of a mixture of nitric acid and sulphuric acid, which is highly oxidizing and may oxidize the Pt-electrodes, fuming sulphuric acid was used. Doing the acid treatment on graphene deposit on wafers would enable the possibility of detecting the expansion using AFM.

Acid treating the graphene after deposition on the wafer did not give any useful results. All material (both graphene and graphite) on the wafer washed off, despite careful treatment, probably due to the sulphuric acid intercalating into the SiO_2/graphite site. Instead the graphite acid was

treated pre-deposition. The first indication of successful absorption of the acid into the inter-planar sites, could be seen from the weight of the graphite, which approximately double for all graphite pieces, independent on the initial weight of the graphite pieces.

A combination of SEM and XRD measurements, were used in order to verify that the graphite have preserved the high order and quality after the acid treatment. Figure 5.5 is SEM images of pristine and acid treated graphite, 5.5a and 5.5b respectively. The highly planar structure of the pristine graphite, has been visualized by showing an edge where the layered structure is visible. The acid treated graphite shows the same structure indicating preservation of the same highly planar structure. The layered structure seen here is not single layers of graphene thus the interlayer distance can not be extracted from these images, as the scale is to large. The two images look slightly different, with the planar lines in the acid treated more separated. This is however due to variations in the specific sample, and do not indicate a change in the sample after acid treatment. At least not on a scale of 100 nm.

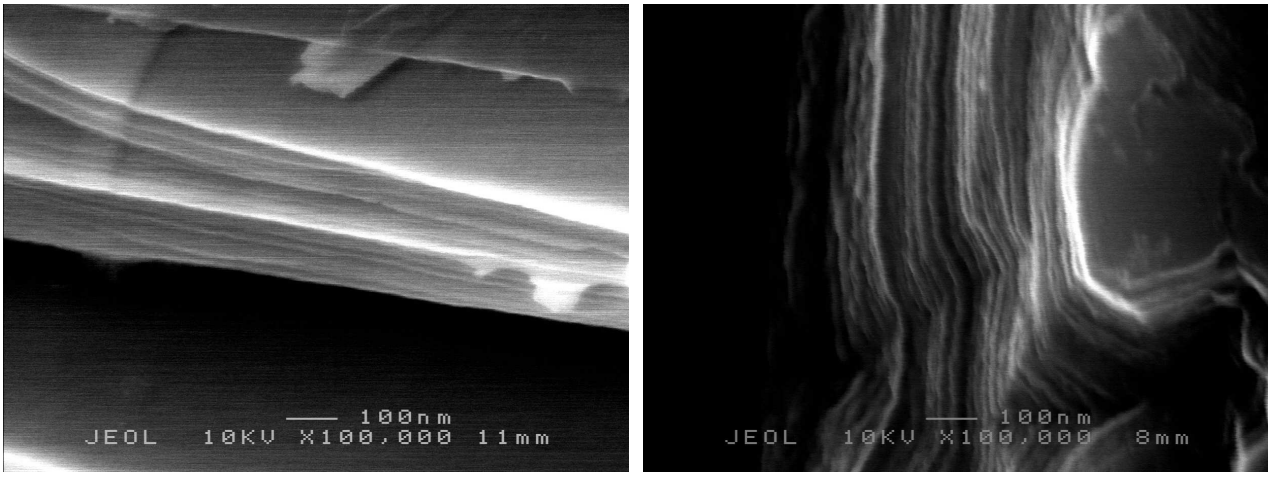

(a) **(b)**

Figure 5.5: SEM image of (a) Pristine graphite (b) Acid treated graphite. Both images shows the layered structure of graphite, indicating that the acid treatment does not destroy the planar order.

XRD experiments were conducted to give information on small changes to the interlayer distance after acid treating the gaphite. The data presented in figure 5.6 are taken with a XRD apparatus at Risø, DTU, with x-ray wavelength $\lambda = 1.54$ Å, hence the peak position values extracted from the fits have at most a precision to the second decimal due to the limitation from the x-ray wavelength distribution, see section 4.4 for discussion on the uncertainties of the measurements. Figure 5.6a shows the high quality of the graphite, also seen in the SEM images. The spectrum only show two very sharp peaks, namely one at $26.64° \pm 0.01$ and $54.75° \pm 0.01$. The first correspond to a very well-defined reflection from the (002)-plane, and gives an interlayer distance of 3.34 Å. The second peak at $54.75° \pm 0.01$, corresponding to $d = 1.670$ Å, for $n = 1$, but is most probably the second order peak of the (002)-reflection, see section 4.6. After the acid treatment a slight decrease in the position of the (002)-peak at $25.30° \pm 0.01$, resulting in an increased in d spacing for the (002) direction, $d = 3.52$ Å, see figure 5.6b. Furthermore the peak is more broaden (going from a FWHM of 0.08 ± 0.01 to 0.70 ± 0.03), assigned to a less well-defined d-spacing. Again is the second order peak to the (002)-

reflection visible, namely at $51.89° \pm 0.2$. The two new peaks at $29.67° \pm 0.09$ and $56.65° \pm 0.1$ corresponds to a diffraction plane distance of 3.01 Å and 1.62 Å, respectively. The specific origin of these peaks are still unknown.

The increased d-spacing after acid treatment most likely was due to intercalation of the sulphuric acid. Which would also explain the broadening of the (002)-peak as the arrangement of the intercalation molecules would not be as perfect as the pristine graphite layers. But the (002)-direction is still preserved enough for the second order peak to be visible, indicating that the highly ordered structure is preserved, only with a slight different plane distance. An explanation of the two new peaks could be due to an in-plane periodic arrangement of the intercalated molecules, giving rise to lattice plane diffraction, or due to a constant distance between intercalated molecules between graphene layers. Instead of using a acid mixture of nitric and sulphuric acid as proposed by Chen et al.[13], the XRD data indicates that a pure sulphuric acid treatment is enough to produce expanded graphite. This is concluded as it seem very likely that the observed change in diffraction pattern can be contributed to successful intercalation. XRD measurements on the expanded graphite, obtained by heat treating the acid treated graphite, are presented in section 5.3.

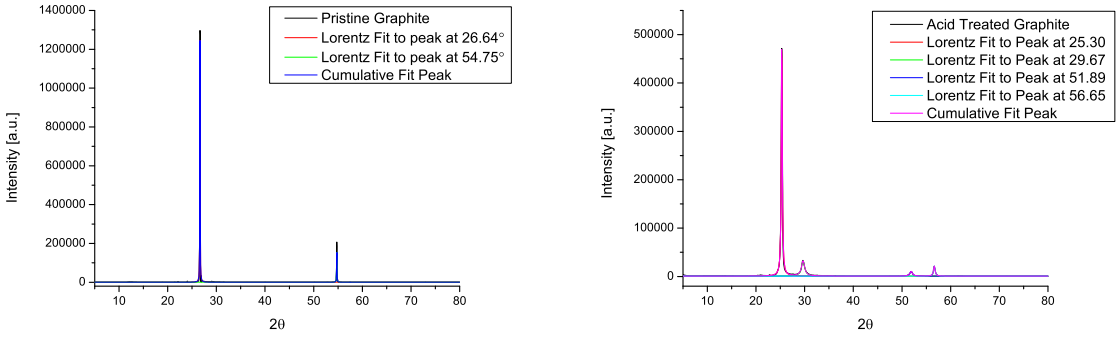

(a) **(b)**

Figure 5.6: XRD measurements on graphite. Lorentz functions are used for peak fitting. **(a)** Pristine graphite, with two pronounced peaks, one at $26.64°$ originating from the (002)-reflection and the second order of this at $54.75°$, corresponding to a interlayer distance of 3.34 Å. **(b)** Acid treated graphite, which shows a quit different spectrum. The (002)-reflection is moved to $25.30°$, with second order at $51.89°$ and d-spacing of $d = 3.52$ Å.

Due to limited time, experiments with C_{60} intercalation into expanded graphite on SiO_2-wafer were not conducted. Instead it was attempted to intercalate C_{60} into bulk graphite, and then wafer deposit afterwards.

5.3 Graphite Intercalated Compounds

After intercalation attempt, but before wafer-deposition, XRD measurements were conducted, on both expanded graphite and the attempted C_{60} graphite intercalated compound (GIC), see figure 5.7. The expanded graphite was produced by heat treating the acid treated graphite. The GIC was produced from expanded graphite. The two spectra, taken at MaxLab with an x-ray wavelength of $\lambda = 1.048$

Å, hence having a precision to at most third decimal, are identical, only showing the (002)-peak around $18.00° \pm 0.001$, corresponding to $d = 3.35$ Å. No peak around 6.0° are present in the GIC spectrum, as is expected for a stage-1 C_{60} intercalation product†. Hence these measurements show no sign of successful intercalation. The slight change in the (002)-reflection observed for the acid treated graphite, are not seen for the expanded. The unchanged interlayer distance are consistent with the experiments conducted by Chen et al. [13], which were the basis for the graphite used by Gupta et al. [28].

It is speculated that the heat treatment de-intercalate all intercalated molecules from the acid treated graphite, creating the expanding separate MLG, so the graphite sample consist of many MLG sheets expanded from each other, each preserving the interlayer distance of pristine graphite.

The preserved interlayer distance and no further peaks is strong evidence of unsuccessful intercalation, and is in contrast to the results obtained by Gupta et al. [28]. The experiments can, however, not be completely compared, as they differ slight. The difference lies in the graphite used, as already explained. To summarize, Gupta et al. [28] uses a powder of exfoliated graphite, which probably consist of FLG sheet with the same interlayer distance as pristine graphite of 3.3 Å. The same is true for the expanded graphite used in this project, except the sheets are expected to be significantly thicker, at least MLG if not more. As the interlayer distance and not the thickness of individual graphite sheets was expected to be the important factor, the difference in used graphite is most likely not causing the negative result obtained in the project. However it can not be ruled out, and XRD measurements on an attempted intercalated exfoliated graphite, similar to the one produced by Gupta et al. [28], is a necessity for conclusions to be made. These were not conducted as the focus was to do a complete investigation on the C_{60} treated expanded graphite. Further discussion of the results obtained by Gupta et al. [28] compared with those of this project, is done in section 5.5.

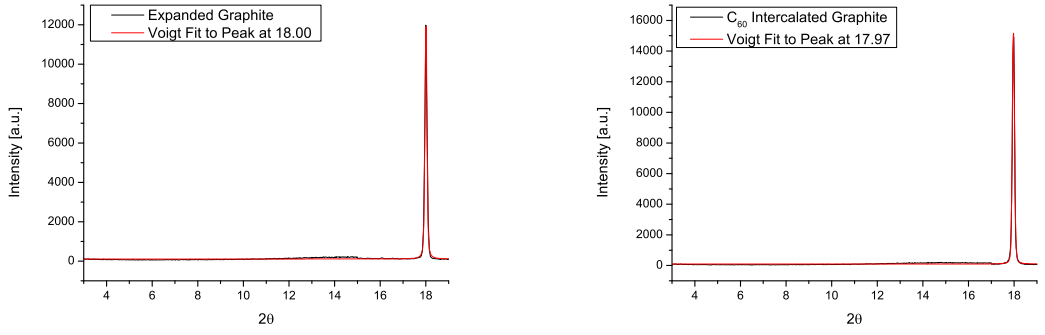

Figure 5.7: XRD data of measurements on graphite, with x-ray energy of 1 Å. **(a)** Expanded graphite only showing one peak at the measured angles, at 18° corresponding to a d-spacing of 3.35 Å. **(b)** C_{60} intercalated Graphite only showing one peak at the measured angles, at 18° corresponding to a d-spacing of 3.35 Å, hence showing no sign of intercalation.

After the XRD measurements Raman spectra on the same samples, expanded and C_{60} treated graphite, were recorded. These experiments was expected to yield information on whether C_{60}-molecules were present in the latter. The charge transfer from the graphene to the C_{60}-molecules,

†An interlayer distance of 1 nm corresponds to a Bragg peak at 6.0°, $\theta = \sin^{-1}(1.048 \cdot 10^{-10}\text{m}/(2 \cdot 1 \cdot 10^{-9}\text{m})) = 3.0°$

should move the graphene G peak towards higher wave-numbers. The G-peak position differs slightly between the two samples, with the position for expanded graphite around 1589.6 $c\text{m}^{-1} \pm 0.6$ and 1591.8 $c\text{m}^{-1} \pm 0.6$ for the intercalated. The observed difference, albeit small, might be due to a p-doping of the graphite from the C_{60}. If a C_{60}-molecule film did cover the graphite sample, the ratio of doped graphene sheets to pristine sheets (not in direct contact to C_{60}) might be high enough to be detected in the measurement. Raman data of a proposed stage-4 compound of the C_{60}-intercalation graphite, is reported to yield a double peak, as the G peak splits for the doped and undoped layers of the sample[29]. Unfortunately such a splitting might not be detectable in the spectrum in figure 5.8b as the spectrum unfortunately was taken with a too low resolution, hence the expected difference between the G peak position of a C_{60} doped and pristine graphene would possibly lie within the resolution of the spectra which was 5 $c\text{m}^{-1}$ per measuring point, see section 2.4. If this is the case a double peak might be measured as single peak if both peak maxima is within the same measuring interval, giving a peak position between the to original peaks. New and higher resolution measurements are desirable, but due to reconstruction of the laboratory the Raman spectrometer was inoperative at the time the mistake was detected.

A more thorough discussion of the results obtained compared to Gupta et al.[28] is conducted in section 5.5.

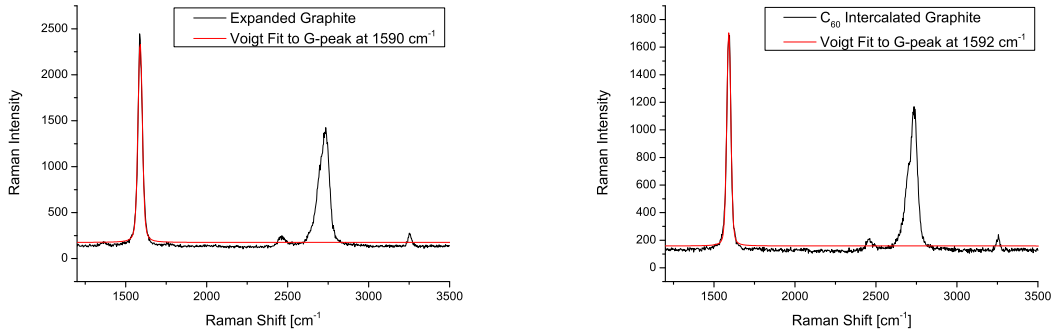

(a) **(b)**

Figure 5.8: Raman spectra taken with a laser wavelength of $\lambda = 514$ nm. **(a)** Expanded graphite **(b)** Intercalated graphite

As the original goal was to do transport measurements on C_{60} intercalated BLG with use of CAFM, wafers with FLG sheets were prepared from three different types of graphite, namely pristine, expanded graphite and "intercalated" graphite. These measurements were conducted despite the negative results from above presented experiments, but it might be possible to detect a difference in conductance between pristine and expanded graphite.

I-V curves were recorded with CAFM at four different sites for two FLG sheet prepared from the pristine graphite, referred to as P1 and P2, see figure 5.9 and B.4, respectively. By direct comparing the I-V curves for P1 it can be seen that the conductance is stable for three of the four measurements, namely for the two at the electrode (place 1 and 4) and for the sheet close to the electrode (place 2). The measurements away from the electrode shows an slight decrease in slope, e.i. in conductance. At first glance this could be due to the increased distance to the sheet, but are more likely bad contact

between the tip and the flake as will be discussed below. However a series of measurements on the sheet with increasing distance to the electrode might reveal whether of the two are a valid explanation. The measured conductances, for both P1 and P2, are summarized in table 5.1.

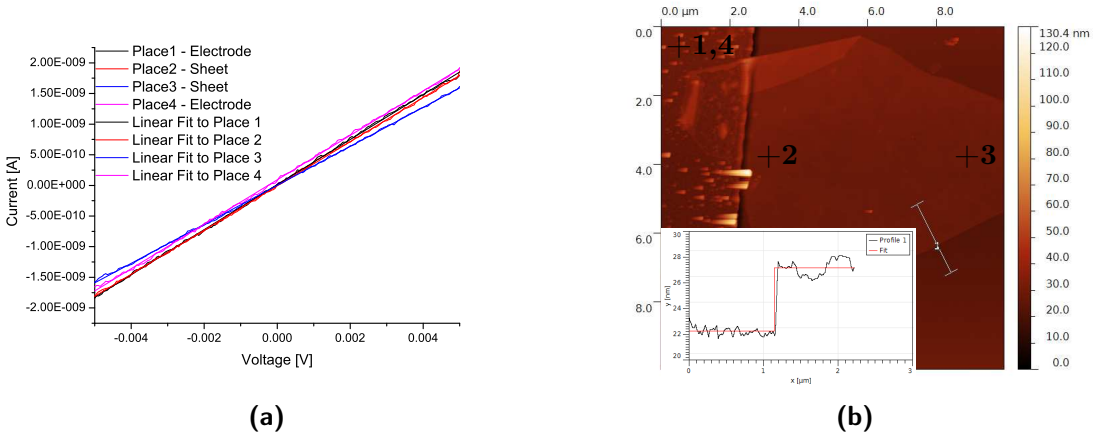

(a) **(b)**

Figure 5.9: Conducting AFM on a pristine few-layered graphene flake deposited on SiO_2, referred to as flake 1. **(a)** Conducting AFM measurements of pristine few layered graphene sheet, first at the electrode then twice at the sheet and lastly at the electrode again, see (b) for specific places. The conductances are extracted by a linear fit to the data. **(b)** AFM image of flake 1. The measuring sites are marked by a +-sign and a number. Inset are the line profile 1, and the fitted square profile yields a sheet height of 4.9 nm.

Place 1 and 4 are direct measurements on the electrode, before and after engaging the flake, verifying whether the contact between the CAFM tip and the sample changed with the number of measurements. Comparing the two measurements for P1, 2.72 $M\Omega$ and 2.76 $M\Omega$, no change are observe as the slight different are within the uncertainty of the measurements. Indication on some degradation of the tip for P2, are visualized by resistance increasing from 2.60 $M\Omega$ to 2.84 $M\Omega$, see figure B.4 for the I-V curves. The two measurements on P2 (place 2 and 3) shows a general degradation after engaging the sample, with place 3 having the same total resistance as the second measurement on the electrode (place 4).

From the measurements on pristine graphite samples, a tendency towards the resistance of the pristine graphite sheet being too low to alter the total resistance detectable, is observed. Furthermore it is seen that resistances between 2.6 $M\Omega$ and 3.1 $M\Omega$ are the interval of expectable values for this type of device, taking degradation of the tip and the slightly random tip-sample resistance into account. Hence the good statistics on the every individual I-V curve, as discussed in section 4.3, is irrelevant as the total resistant of the system can change from 2.55 $M\Omega$ to 2.84 $M\Omega$ for the same place on the same electrode. Thus a graphite sheet resistance of the order of $M\Omega$ might be necessary to be detectable. This rather unstable measurements makes the technique less suitable for these highly conductive samples.

The CAFM measurements on two flakes of C_{60} intercalated graphite, referred to as I1 and I2, can be seen in figure 5.10 and B.5. Again are the differences between measurements directly on the electrodes and on the flake not pronounced. Comparing the I-V curves for pristine graphite, figure 5.9, and the intercalated sample, 5.10, only supports the Raman and XRD measurements in showing no

Table 5.1: Conductance data for Pristine Graphite

		Avg. Conductance	Avg. Resistance
Flake 1 Fig. 5.9b	Place 1 (Electrode)	$0.367 \pm 0.0002\mu S$	$2.72 \pm 0.002M\Omega$
	Place 2 (Sheet)	$0.361 \pm 0.0002\mu S$	$2.77 \pm 0.001M\Omega$
	Place 3 (Sheet)	$0.318 \pm 0.0002\mu S$	$3.14 \pm 0.002M\Omega$
	Place 4 (Electrode)	$0.363 \pm 0.0002\mu S$	$2.76 \pm 0.002M\Omega$
Flake 2 Fig. B.4	Place 1 (Electrode)	$0.384 \pm 0.0002\mu S$	$2.60 \pm 0.002M\Omega$
	Place 2 (Sheet)	$0.362 \pm 0.0002\mu S$	$2.76 \pm 0.001M\Omega$
	Place 3 (Sheet)	$0.350 \pm 0.0002\mu S$	$2.85 \pm 0.002M\Omega$
	Place 4 (Electrode)	$0.355 \pm 0.0003\mu S$	$2.82 \pm 0.002M\Omega$

sign of intercalation. The measurements on I1 again shows a single measurements with an increased resistance, comparable to place 3 for P1. A second measurement on I1, place 4, in the same distance to the electrode as place 3, showed a "normal" resistance of 2.8 $M\Omega$. This indicates that it is local differences or bad tip-sheet contact rather than a distance dependency that increases the resistance.

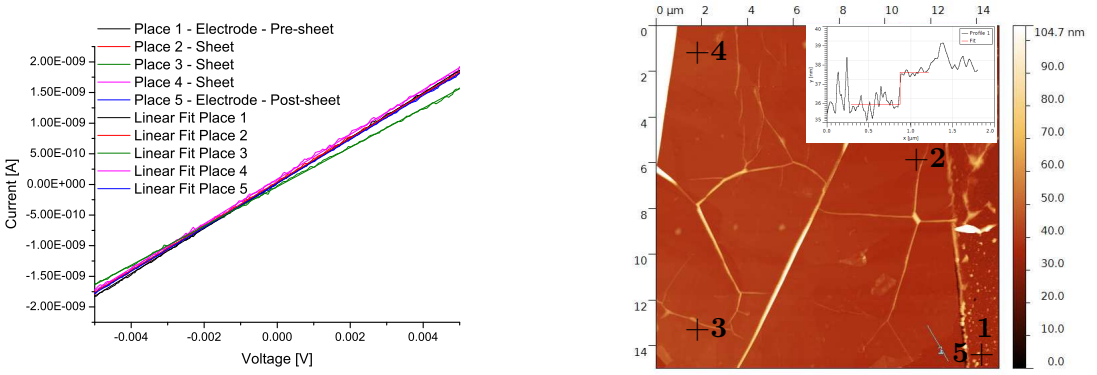

(a) **(b)**

Figure 5.10: Conducting AFM on intercalated few-layered graphene deposited on SiO_2 wafers. **(a)** The averaged I-V curves for the 5 different measurement sites seen in (b). **(b)** AFM image of the flake, where the measuring sites are marked with a +-sign and a number.

Table 5.2 collects the conductance data from the linear fits from figure 5.10a and B.5. I2 shows in general an increasing resistance with the number of measurements. However place 3 has a resistance of almost 4 $M\Omega$. This could be due to local intercalation of C_{60}. The measured sheet however did have a huge fold between the site of measurement and the electrode, which could increase the resistance of the sheet. Small wrinkles in a graphene sheet is reported to increase scattering hence lowering the conductance[53], and is the most likely explanation for the elevated resistance.

CAFM measurement on a single sheet of expanded graphite were conducted to verify that the acid treatment and subsequent heating did not change the resistance. The data are presented in figure B.6 and shows the same total resistance of 2.7 $M\Omega$ as seen for most of the measurements on the pristine and intercalated samples. Hence producing expanded graphite does not alter the electronic properties detectable within the precision of the CAFM setup.

The CAFM measurements showed in general no sign of intercalation. Albeit the individual I-V

Table 5.2: Conductance data for Intercalated Graphite

		Avg. Conductance	Avg. Resistance
Flake 1 Fig. 5.10b	Place 1 (Electrode)	0.369μS	$2.71M\Omega$
	Place 2 (Sheet)	0.360μS	$2.78M\Omega$
	Place 3 (Sheet)	0.320μS	$3.12M\Omega$
	Place 4 (Sheet)	0.359μS	$2.79M\Omega$
	Place 5 (Electrode)	0.364μS	$2.74M\Omega$
Flake 2 Fig. B.5	Place 1 (Electrode)	0.373μS	$2.68M\Omega$
	Place 2 (Sheet)	0.347μS	$2.87M\Omega$
	Place 3 (Sheet)	0.251μS	$3.99M\Omega$
	Place 4 (Electrode)	0.327μS	$3.06M\Omega$

curves was recorded with many measuring points, hence increasing the statistics, random tip-sample contacts neutralized this, giving measured resistance varying 0.3 $M\Omega$ for two individual measurements on the same sample same place.

To summarize the experiments on synthesis of a pure C_{60} intercalated graphite compound, non of the results gives indications towards that the intercalation were successful. A higher resolution Raman spectrum, would give information on whether the graphite where doped by the C_{60}, but it could be speculated that for a highly expanded (or exfoliated) graphite sample the surface adsorbed C_{60}-molecules could yield the same result as an intercalation product. Further discussion can be found in section 5.5.

5.4 Potassium and C_{60} co-Intercalated Bilayer Graphene

Another approach towards intercalation of C_{60}-molecules into bilayer graphene was attempted, through an intermediate product of potassium intercalated graphite. Both solution-based, inspired by the work of Fuhrer et al. [23], and thermal intercalation experiments were conducted. As most of the samples from these experiments were very unstable in the atmosphere, proper characterization were difficult and hence all discussions are based on optical microscope images, limiting the conclusive statements.

5.4.1 Pre-cursor C_8K

The pre-cursor, stage-1 potassium intercalated graphite C_8K, was prepared by thermal intercalation. Characterization of this GIC is limited as the potassium covering the sample oxidized and destroyed the samples. Figure 5.12a are an optical microscope image of a sample after intercalation of potassium still inside the quartz tube, hence the blurry image. For a image of a sample exposed to the air after the quartz tube were smashed see figure 5.11. The apparent wet surface is probably due to the potassium reacting with the oxygen or water in the air forming either potassium oxide or hydroxide (probably both). The surface of the wafer could due to the fast oxidation not be further investigated, but from analysis of the optical microscope images (both 5.12a and 5.11b), it seems likely that a potassium film did cover the entire wafer. The change in contrast of the graphite sheets indicate that the potassium intercalation was successful, but this is very speculative.

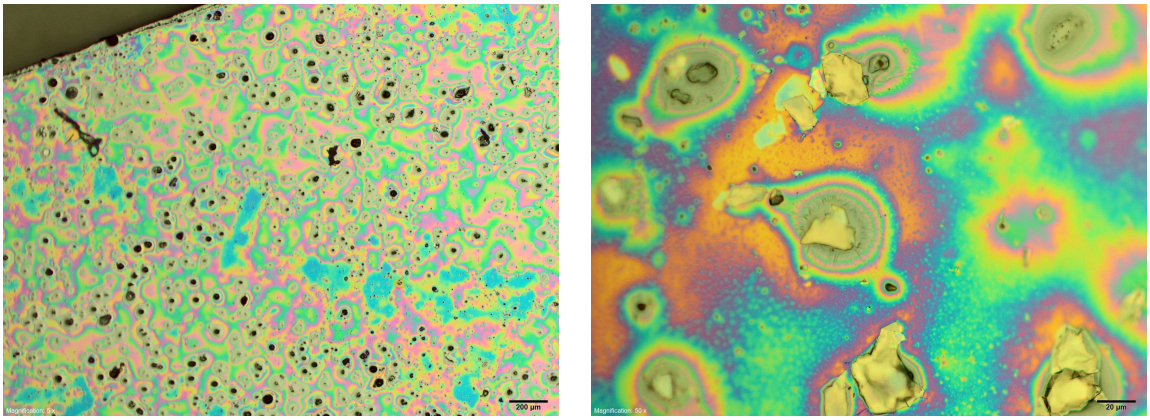

(a) **(b)**

Figure 5.11: Optical microscope images of the potassium intercalated graphite samples on wafers exposed to the air. **(a)** Overview of such a sample. **(b)** Zoom of graphite sheets, which in this image has a gold contrast. The contrast could indicate potassium intercalation, albeit it is hard to deduce anything from these colourful images.

The potassium film covering the wafer was tried removed by creating a temperature gradient through the quartz tube, with the wafer at the high temperature end. The hope was that it required more energy to remove the intercalated potassium than that on the surface. Figure 5.12b is the wafer after 35 min at 100°C. Comparing figure 5.12a and 5.12b, the same contrast between the SiO_2- and Pt-areas are seen. On the contrary some of the graphite sheets have changed color. This indicates de-intercalation of potassium rather than desorption from the surface. These observations, however are very speculative and more experiments needs to be conducted before anything can be said. These experiments could be a more thorough determination of the temperature dependence of the desorption of potassium. Raman measurements could be used to determine if the potassium was intercalated and if it did deintercalated under the heat treatment. This would be evident from the doping dependency of the G-peak position. Also an appropriate way of handling the potassium samples are needed, which not only should protect against the oxidization, but also hold the possibility of conducting characterization measurements in situ.

5.4.2 Solution Based Intercalation

After potassium intercalation, C_{60}-molecules were tried intercalated through solution. The result can be seen in figure 5.13a, which is an optical microscope image of the same area as in 5.12 (just rotated 90°). From this it evident that something had happen, but it is still unknown whether the intercalation was successful or not. A likely scenario is that the suggested potassium film, had been intercalated with a combination of C_{60} and benzene, as an intercalation product of potassium and C_{60} are well documented in the literature[88]. A Raman measurement would give further indications towards what reaction had taken place.

The results showed that this type of reaction are either not suited for samples on wafers or a lot of optimization are needed. Figure 5.13b shows another part of the sample, where the bottom electrodes have been destroyed. The observation that the electrodes seems flushed away, could indicates that

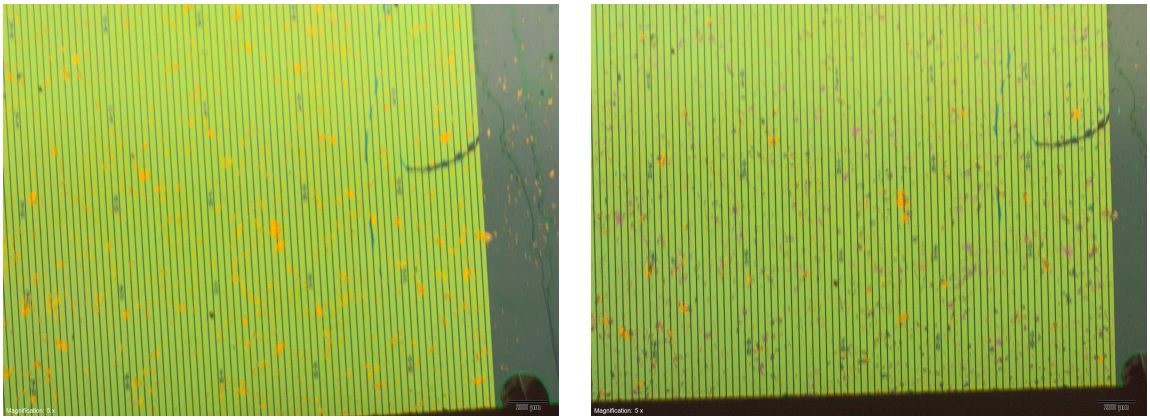

(a) **(b)**

Figure 5.12: (a) Optical microscope image of potassium intercalation into graphite deposited on SiO_2-wafers. A significant change in contrast is seen, indicating successful intercalation. **(b)** An attempt towards cleaning the wafer surface for the expected potassium film, by heating the wafer still in the quartz tube to 100°C for 35 min. Deintercalation is observed as some of the graphite sheet returns to the original contrast.

the SiO_2 have been etched, remembering the electrodes were etched down in the SiO_2, approximately 40 nm. The etching scenario seems likely as the wafer was shortly introduced to the atmosphere (less than 5 s) when transferred to the solution of C_{60} in dry benzene. Even the slightest amount of KOH in the solution could be enough to etch the required 40 nm, as the solution was heated to 80° for 24h. These considerations suggest that the intercalation should be done before wafer deposition.

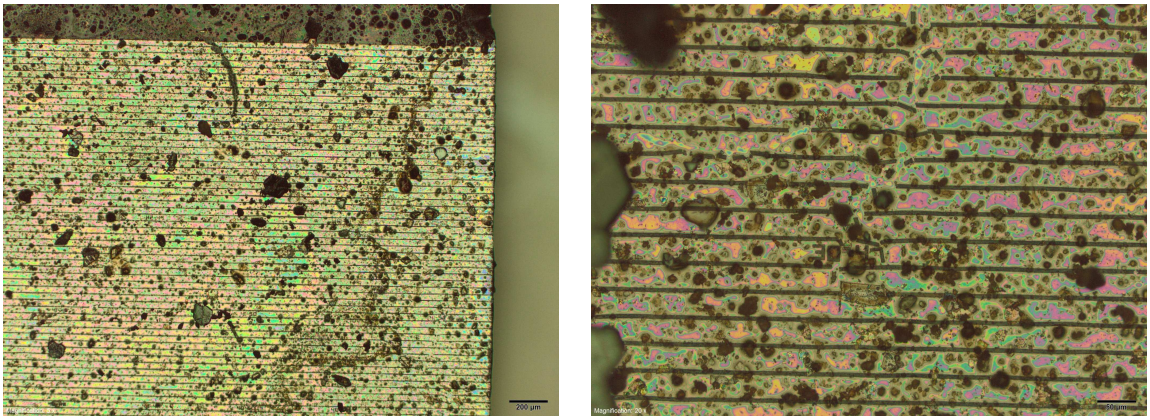

(a) **(b)**

Figure 5.13: (a) Optical microscope image of same area as in 5.12, just rotated 90°, after solution based intercalation of C_{60}. **(b)** One example of the destruction of electrodes when solution intercalating C_{60}.

As the experiments on wafer samples encountered so many unforeseen problems, it naturally follows to do the same experiments on pristine graphite, basically replicating the results obtained by Fuhrer et al.[23]. Raman and XRD measurements on the synthesized GIC with give details towards whether the intercalation were successful or not. These considerations are further discussed in section 5.5.

5.4.3 Thermal Intercalation

Instead of the solution based intercalation, a quartz tube was sealed containing potassium, C_{60}-powder and BLG-samples. The idea was to first increase the interlayer distance by heating the tube to 300°C for intercalation of potassium and subsequent to 600°C for the C_{60}-molecule intercalation. By keeping the sample in the quartz tube oxidation of the potassium could be avoided and hopefully resulting in a stable GIC. Figure 5.14 shows optical microscope images of the product. Again, due to the limited access to the Raman spectroscope and many unsuccessful AFM measurements, no further characterization was conducted on these samples, so all discussion will be on the basis of these two images and hence the only thing that can be conclude is that something had happened. One possible scenario is that the C_{60} and potassium have formed a K_xC_{60} film covering the sample, giving rise to the significant contrast change. This postulate is supported by figure 5.14c, where an apparent uniform film covering the wafer. The turquoise color of the graphite sheets seen in figure 5.14b differs from anything seen on the other samples. It is worth observing the uniform contrast of the sheet after thermal treatment, is independent on the thickness observed in figure 5.14a.

These considerations will be more thoroughly discussed in section 5.5.2 and compared to the results obtained by Fuhrer et al.[23].

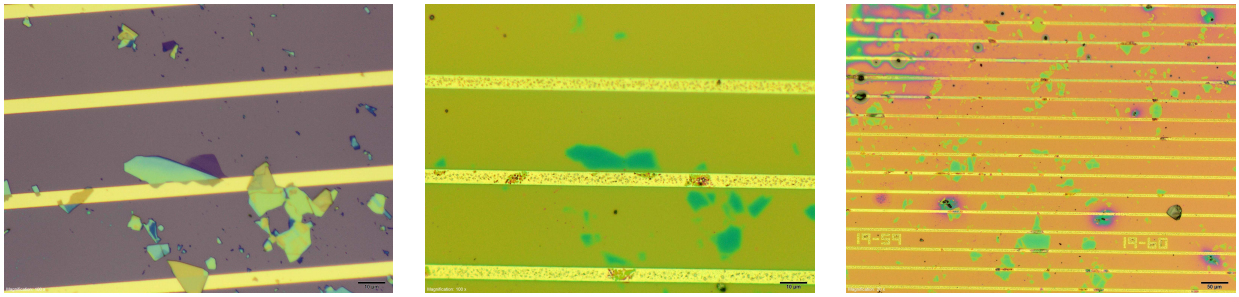

(a) **(b)** **(c)**

Figure 5.14: Optical microscope images of thermal co-intercalation of potassium and C_{60}. **(a)** The MLG flake before intercalation. **(b)** The same flake as in (a) after thermal intercalation of K and C_{60}. **(c)** An overview image of the sample after thermal treatment. What appears like a more or less uniform is covering the surface.

The natural next step is to perform Raman measurements on a sheet from the sample seen in figure 5.14. These measurements would give a good indication towards the nature of the reaction which appears to has taken place. Also experiments with pristine graphite could be interesting, as XRD measurements on such a sample would give a clear results, showing whether the intercalation was successful.

5.5 The Carbon Burger Revisited

As the goal of this thesis, intercalation of C_{60} into bilayer graphene, did not succeed, explanation towards what went wrong will be presented, along with a slightly alternative interpretation of the results obtained by Gupta et al.[28] and Fuhrer et al.[23].

5.5.1 C_{60} Intercalated Bilayer Graphene

The main goal, synthesizing a pure carbon structure by thermally intercalating C_{60}-molecules into BLG or graphite were unsuccessful, albeit Gupta et al.[28] have demonstrated the intercalation into graphite. As discussed in chapter 2 they verify the structure with use of Raman spectroscopy and TEM imagining and diffraction.

The Raman data shows a doping of the G-peak indicating charge transfer from graphene to the C_{60}, changing their Fermi-levels. This doping is as such not evidence for successful intercalation as a C_{60} covered graphene sheet would give a similar result. Albeit one would expect a double peak from C_{60} covered graphite, the type of graphite used by Gupta et al.[28], i.e. highly exfoliated graphite powder with a high percentage of FLG sheets[13], could probably yield the published results. In another article by Gupta et al.[29] from 2005, they publish Raman data from both stage-1 and stage-4 GICs, see figure 5.15. The stage-1 compound is the same as discussed before, but the stage-4 shows some different characteristics. The G-peak is split into two individual peaks, one at 1582 cm^{-1} and another at 1586.6 cm^{-1}, assigned to a pristine and an up-shifted E_{2g}-mode of graphite, respectively. The splitting is assigned to the difference between layers in contact with intercalated species and those not in contact. Hence they argue that stage-1 should be a single peak, as seen from figure 5.15a, while for stages ≥ 2 a double peak would appear, as seen in 5.15b. It is not given that a stage-2 compound would yield a double peak as every graphene sheet in this compound are in direct contact to a C_{60} layer. For stage ≥ 3 it seems more likely that the graphene can screen doping from the layer not in direct contact with the C_{60}-molecules, which might preserve the original E_{2g}-mode.

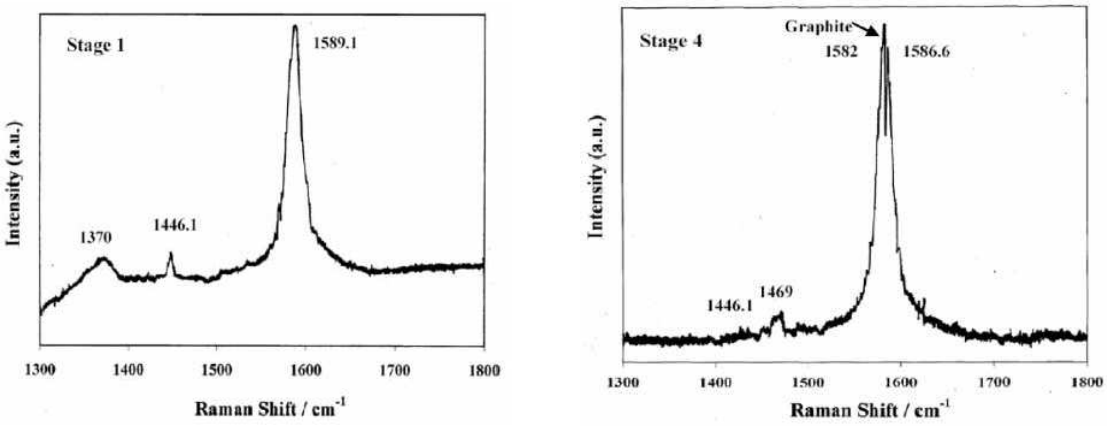

Figure 5.15: Raman spectra of **(a)** stage-1 and **(b)** stage-4 compound of C_{60} intercalated. Adopted from Gupta et al.[29]

In the article from Gupta et al.[29] they also show the TEM data from both a stage-1 and stage-4 compound, figure 5.16a and 5.16b respectively. From the images Gupta et al.[29] find a interlayer distance of 1.27 nm for the stage-1 compound, but does not extract the distance for the stage-4 compound. In the article from 2004[28] they include a diffraction image from a sample similar to the one seen on figure 5.16a. They comment that the sample showed hexagonal symmetry, but apart from that the diffraction pattern is not further used. For a stage-1 compound the distance between two

C_{60} monolayers is expected to be approximately 1.3 nm. The distance between C_{60}-molecules in a monolayer is approximately 1 nm[16]. In the lower left corner of figure 5.16a is a rough hand-drawn hexagon to indicate the hexagonal nature of the sample. The distances between opposite corners in this non-precise drawing are 3.05 nm, 2.93 nm and 2.9 nm, approximately yielding a C_{60}-C_{60} distance of 1.5 nm, surprisingly independent whether they are separated by a graphene layer or not. This is supported by the diffraction image seen in 5.16c, where 5.16d is an enlargement of the lowest order diffraction peaks. Again a hexagon is hand-drawn to visualize the hexagonal structure and to show the points between which the distance was measured. As the original image did not include information on the scale, one of the opposite corner distances was set to 1. By coincident the other two distances did also hit 1, with two decimals precision, giving further indications towards an equally sided hexagonal lattice. Such a lattice could indicate that the measured TEM and diffraction data might be a monolayer of C_{60} molecules on a FLG sheet. However the measured NN distance for the C_{60}-molecules of 1.5 nm larger than the 1 nm expected within the monolayer, is not in agreement whit this statement. A diffraction pattern from the presumed stage-4 compound would have helped describing the overall structure for the GICs. Thus the stage-4 compound can not be further discussed.

Although XRD measurements on C_{60} intercalated expanded graphite did not indicate intercalation, these measurements can not be used when attempting to deduce whether the data presented by Gupta et al.[28] show intercalated graphite or graphite covered by C_{60}-molecules. The reason for this is the difference in the graphite used. As mentioned before the graphite was processed within the terms of Chen et al.[13]. The interlayer distance was expected to be the important factor. Chen et al.[13] show that both the graphite nano-sheet and the graphite worms retain the same interlayer distance as pristine graphite. Hence it was decided to do the intercalation experiments with nano-sheets, even though Gupta et al.[28] most probably used the graphite worms. The graphite worms, which were exfoliated expanded graphite, is a powder consisting of many FLG sheets. Depending on the efficiency of the exfoliation, parts of such a sample might yield the Raman data seen for both presumed stage-1 and stage-4 compounds after intercalation. If it is presumed that the TEM data for the stage-1 compound instead shows a C_{60} film covering a FLG sheet, this could also be a possible scenario with the graphite worms. Although the found C_{60}-C_{60} distance is inconsistent with this explanation, it is also difficult to describe within the intercalation scenario, as equal distances would not be expected. A difference in distance between C_{60} molecules separated by a graphene layer and in direct contact is expected.

5.5.2 Potassium and C_{60} co-Intercalated Bilayer Graphene

The experiments with co-intercalation of potassium and C_{60}-molecules were inspired by the work done by Fuhrer et al.[23]. As discussed previously they state to have synthesized the heterostructure with the stoichiometry $C_{32}K_4C_{60}$. This postulate is only backed-up by transport measurements, showing superconductivity of the sample with $T_c = 19.5°$C. Raman spectroscopy and XRD measurements were at the time of publication (1994) ongoing, but have unfortunately never been published. Also the T_c's dependency on the electric and magnetic field were in progress, but for some reason remained unpublished. If published these measurements would clearly demonstrate whether the superconductivity

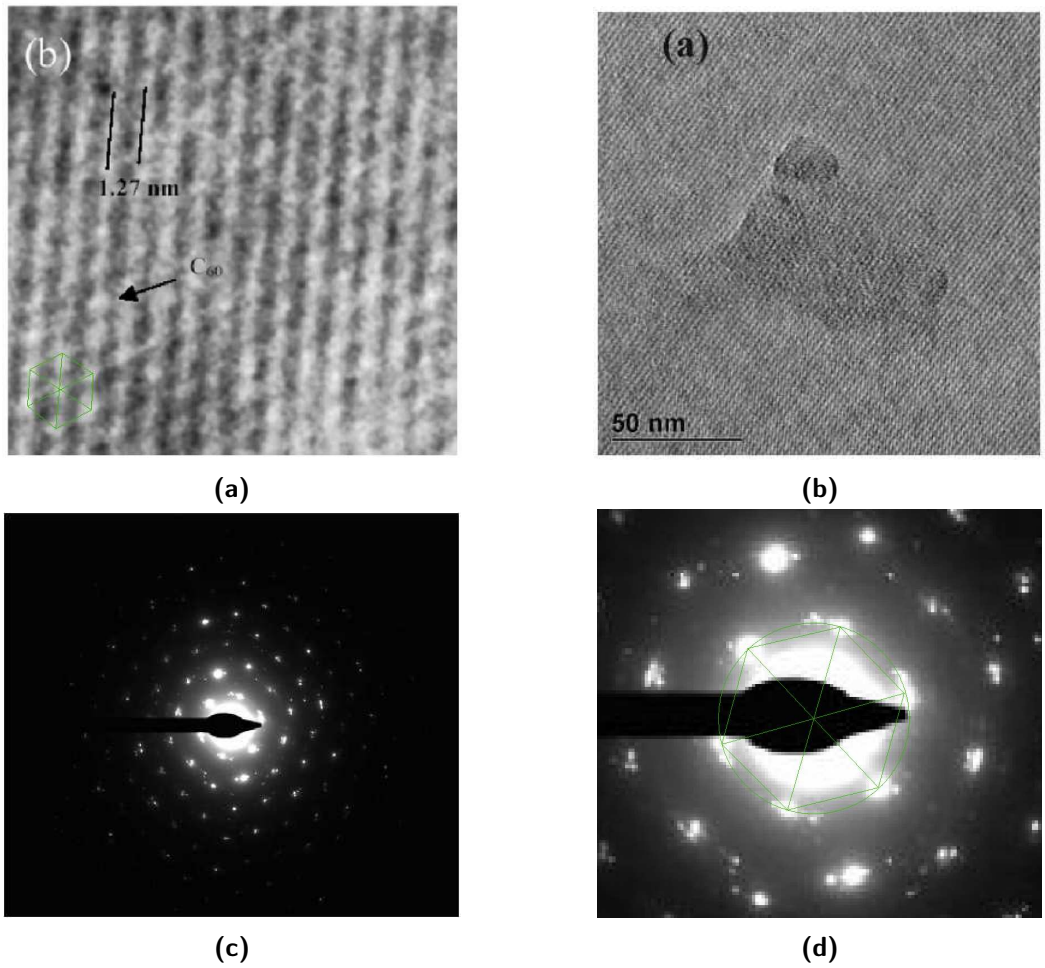

Figure 5.16: TEM imagine of **(a)** stage-1 and **(b)** stage-4 compound of C_{60} intercalated. **(c)** An diffraction image of the sample seen in (a). The diffraction pattern are hexagonal. **(d)** Zoom of the low order diffraction spots used to analyse the diffraction pattern further. It is seen from the circle and hand drawn hexagon that the hexagonal lattice is equal sided. (a), (c) and (d) Adopted from Gupta et al.[28] and (b) from Gupta et al.[29]

originated from a K_3C_{60} phase present in the sample, as they argue.

The next experiments to be conducted following the results obtained in this project, are to replicate the results from Fuhrer et al.[23] and determine if the intercalation process does take place. The Raman and XRD measurements suggested by Fuhrer et al.[23] are suitable, as they would give information on the condition of the graphite and on the interlayer distance, respectively.

It is speculated that these measurements would most probably yield the information that the graphite was only intercalated with potassium, but covered with a film of superconducting K_3C_{60}. Fuhrer et al.[23] rule out this explanation as they state that the C_{60} would form the isolating phase K_6C_{60} when exposed to potassium in excess. It is not obvious why they expect the potassium to be in excess. The graphite was initially intercalated with potassium, before diluted in a saturated solution of C_{60}. Thus only the surface and the intercalated potassium holds the possibility to react with C_{60} in excess. This might make the K_3C_{60} favourable. This is very speculative, and as stated by Fuhrer et al.[23] further measurements are a necessity, but I tend to believe that a K_3C_{60} film covering their

graphite was the origin of the measured superconductivity and transition temperature of 19.5 K

Furthermore, the possibly large amount of potassium adsorbing to the surface have been reduced by the two-zone intercalation technique used by Fuhrer et al.[23], compared to what was observed for the measurements in this project. A thermal gradient between the potassium and the graphite should minimize the adsorption[17], albeit a thin potassium film would still be expected to cover the graphite. This might have helped in the experiments on wafers, but is not expected to have solved the problem totally, as the removal of the expected potassium film proved very hard. Thus it is still believed that these experiments are not suitable for wafer-samples.

Chapter 6

Conclusion and Outlook

The main aim of this project was to synthesize a 2D all-carbon heterostructure consisting of a C_{60} monolayer between two graphene electrodes. The structure was attempted produced by fabrication of bilayer graphene samples on bottom electrodes, followed by thermal intercalation of C_{60}-molecules, as proposed by Gupta et al.[28]. The structural characterization was done with an optical microscope, an atomic force microscope, a scanning electron microscope, a Raman spectrometer and x-ray diffraction measurements. Electrical characterization was conducted with a conducting atomic force microscope. None of these indicated successful production of the structure.

The second part of the project was to intercalate C_{60} into graphite. The same characterization techniques as in the first part did not show any signs of intercalation for these samples either.

The last part was to expand the interlayer distance of bilayer graphene by intercalation of potassium into graphite, potentially easing the intercalation of C_{60} molecules. These samples were only characterized with optical microscopy, hence all conclusions stated from this part are very speculative.

The results from the three different parts of the project, albeit mostly negative, will be concluded and suggestions to future work will be given within each of these. Finally some overall conclusive remarks are given, to wrap up the project at the final year of my education.

6.1 C_{60} Intercalated Bilayer Graphene

The main objective of the thesis was to intercalate BLG with a monolayer of C_{60} molecules and conduct structural and electrical characterization of the compound. The structural and electrical characterization was successfully conducted, unfortunately not showing any sign of intercalation.

The initial structural characterization measurements were done with AFM, which was the main technique for characterization of graphene samples deposited on wafers. All samples produced, both FLG and MLG, showed no significant increase in sheet thickness as proposed both theoretically[75] and experimentally[28] for a stage-1 intercalation compound.

The small interlayer distance is thought to be the main hindering for the successful intercalation of C_{60} molecules, hence the graphite interlayer distance was attempted increased. This was done by treating the graphite with oleum followed by heat treatment, inspired by the work of Chen et al.[13]. It proved impossible to do the acid treatment or deposition of acid treated graphite on wafers. It would

be possible to deposit expanded graphite on Si wafers and do the intercalation experiments on these. These experiments would most likely yield the same unsuccessful results as for the expanded graphite, reviewed below. Hence further experiments on wafers should first be conducted, when successful intercalation into some type of graphite has been demonstrated, it being expanded, exfoliated or a third new type.

6.2 C_{60} Intercalated Graphite Compounds

The prepared expanded graphite, expected to consist of MLG sheets, was attempted thermally intercalated with C_{60}-molecules. XRD measurements showed that the expanded graphite preserved the interlayer distance of pristine graphite, also confirmed by Chen et al.[13]. Unfortunately, the attempted intercalated sample yielded the exact same results, proving no increased d-spacing, hence no intercalation. A very small successful doping of the "intercalated" graphite was indeed indicated by the Raman spectra recorded for the two samples, however the most possible explanation for this, compared with the XRD measurement, is due to C_{60}-film covering the sample, rather than intercalation.

As one of the main objectives was to do electrical characterization, CAFM measurements were conducted, albeit the AFM, XRD and Raman data revealed that the intercalation process did not work. In addition to introduction to the CAFM, these measurements was thought to maybe give further indications as to whether the acid treatment or the heat treatment altered the properties of the graphene/graphite. The conductance measurements showed that the resistances were roughly constant around $2.7 \pm 0.2\ M\Omega$, with some exceptions. These have been explained by degradation of the tip, wrinkles in the graphene sheet and local variations of the sample. Furthermore it is the tendency that these variations of the contact resistance makes it impossible to extract the conductance of highly conductive graphene sheets, hence all the resistances measured are basically just the serial resistance originating from the experimental setup. Thus the only conclusion that can be made from the electrical measurements is that none of the graphene sheets showed a general increased resistance, at least not measurable with the CAFM. This result is in good agreement with the structural characterization confirming preservation of the quality of the graphite (Raman) and no intercalation (XRD).

If further experiments on C_{60} intercalation into graphite were to be conducted, a complete replication of the experiments by Gupta et al.[28] is the next step. XRD measurements on such samples would give the some of missing information on the lattice planes leading to diffraction, hence give information on a potential intercalation structure. Comparing the results obtained in this project and the result from Gupta et al.[28] it is postulated that (almost) all the results can be explained from a C_{60} film covering FLG samples, albeit the measured interlayer distance of 1.27 nm is hard to explain in this scenario. Another peculiar feature of the hexagonal lattice measured by Gupta et al.[28] is the independency of the C_{60}-C_{60} distance of 1.5 nm on whether the molecules are separated by a graphene layer or not. A distance between adjacent C_{60} molecules of 1.5 nm is not the usual distance reported in the litterature for C_{60} molecules deposited on a graphene sheet. They do pack in a hexagonal lattice, but with a NN distance of 1 nm.

6.3 Potassium and C_{60} co-Intercalated Bilayer Graphene

Along the production of the all-carbon compound, C_{60} intercalation into potassium intercalated graphite was attempted. The potassium intercalation made samples unstable in ambient conditions, complicating the characterization of these sample, hence only optical images were successfully recorded. From these it seemed that a potassium film covered the wafer, with a contrast change of the graphite indicating successful potassium intercalation. This was supported by the cleaning experiments probably resulting in de-intercalation of the potassium — after all, kind of a positive result albeit not intended.

From the optical images from the solution based intercalation, proposed by Fuhrer et al.[23], it could not be confirmed whether the intercalation was successful or not. The observed potassium film covering the sample and the known compound of K_xC_{60}, suggests that K_xC_{60} is covering the wafer. The most important conclusion from these measurements is that the experiments are not suitable for wafer samples. Instead it would be interesting to replicate the sample made by Fuhrer et al.[23] and conduct the XRD and Raman measurements.

6.4 Final Remarks

The use of graphene as electrode holds many advantages over "normal" metal electrodes, as discussed in section 2, and further work in this field is naturally of great interest. Regarding the Carbon Burger, this structure has the possibility of being synthesized, but probably not through intercalation into bilayer graphene (or graphite). Instead, the possibility of producing it in a bottom to top manner seems like a more suitable approach for successful synthesis. In general, intercalation of C_{60} is expected to be very tricky, so the proposed future experiments may just yield further evidence that intercalation does not work for graphite with the pristine interlayer distance of 3.3 Å.

Appendix A

Device Fabrication

Below are the optimized experimental details and recipes used throughout the project

UV-lithography

1. Disperse wafer in Acetone and sonicate for 10 min
2. Disperse in IPA and sonicate for 5 min
3. Blow dry with N_2
4. Bake at 185°C for 5 min. Allow to cool afterwards
5. Spin resist (AZ1505) at 4000 rpm in 45 s
6. Clean masks with Acetone and IPA and blow dry with N_2
7. To remove edge beads expose with appropriate mask for 30 s
8. Change mask to desired design and expose for 4 s
9. Develop in AZ400K (1:4 in millipore water) for 30 s
10. Rinse in millipore water
11. Blow dry with N_2
12. Plasma etch for 20 s

E-beam Lithography

1. Disperse wafer in Acetone and sonicate for 10 min
2. Disperse in IPA and sonicate for 5 min
3. Blow dry with N_2
4. Bake at 185°C for 3 min. Allow to cool afterwards
5. Spin 4% PMMA at 4000 rpm in 45 s
6. Bake at 185°C for 3 min. Allow to cool afterwards
7. Do desired E-beam lithography

8. Develop in MBIK:IPA (1:3) for 60 s
9. Disperse in IPA for 30 s
10. Blow dry with N_2

Etching

1. Prepare two beakers, one with millipore water and one (NOT GLASS) with an Ammonium fluoride - hydrofluoric acid mixture from SigmaAldrich[78]
2. Put wafer in the etching solution for appropriate amount of time (etching rate 1.3 nm)
3. Directly transfer the wafer to millipore water
4. Blow dry with N_2

Metal Evaporation

1. Evaporate wanted metal(s)
2. Develop in PG remover for 1h
3. If development not complete try sonication in PG remover or heating to 80°C

Expanded Graphite

1. Natural graphite are dispersed in fuming sulfuric acid (oleum) for 12h-16h
2. Rinse in millipore water

Quartz Ampoule Cleaning

1. Disperse in Acetone and sonicate for 10 min
2. Disperse in IPA and sonicate for 5 min
3. Blow dry with N_2
4. Plasma etch for 5 min

Thermal C_{60} Intercalation

1. Prepare a clean quartz ampoule with a graphite sample and C_{60}.
2. Evacuate for at least 1h to reach a pressure $< 5 \cdot 10^{-6}$ $m$bar
3. Seal quartz ampoule and heat to 600°C for 2 weeks

Potassium Intercalation

1. Prepare a large heptane bath
2. Take a piece Potassium, wipe off most of the mineral oil, and transfer directly to the heptane.
3. Use a scalpel to cut away some of the oxide layer, to reveal the shine metal. Do this in the heptane bath
4. A piece of clean Potassium is prepared, and another beaker is prepared with heptane and put on a weight capable of measuring with a precision of 0.1 mg
5. Weigh the small piece (target weight is 1-3 mg). Remember to wipe of most of the heptane, before weighing
6. Prepare a cleaned quartz ampoule with your graphene/graphite sample
7. Quickly transfer the potassium piece to the quartz ampoule and evacuate for at least 1h. Pressure $< 5 \cdot 10^{-6}$ $m$bar
8. Seal quartz tube and heat to 300°C for 3h

Solvent C_{60} Intercalation

1. Prepare a Pyrex glass with a C_{60}-saturated dry benzene solution
2. The quartz tube containing the potassium intercalated sample is smashed with a hammer, and the sample is directly transferred to the solution. It can be ease the process to do an intermediate step, where the sample is transferred to a large beaker containing e.g. heptane.
3. The Pyrex glass is sealed and heated to 80°C for at least one day
4.

Thermal co-Intercalation of Potassium and C_{60}

1. Prepare a clean quartz ampoule with a graphite sample, potassium and C_{60}.
2. Evacuate for at least 1h to reach a pressure $< 5 \cdot 10^{-6}$ $m$bar
3. Seal quartz ampoule
4. Heat the quartz tube to 300°C for 3 hours
5. Heat the quartz tube to 600°C for 2 weeks

Appendix B

Supplementary Results

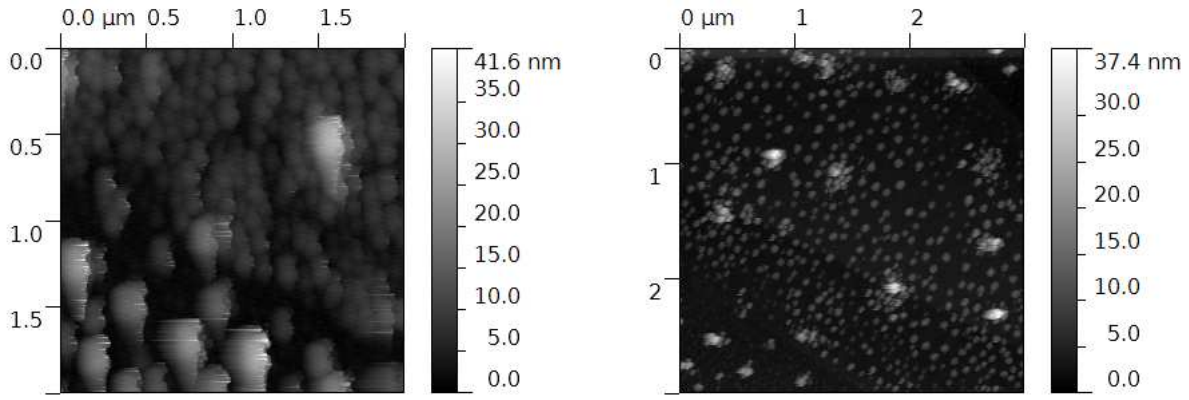

(a) **(b)**

Figure B.1: **(a)** An example of the large amount of material adsorbed to the graphene sample after intercalation was attempted. **(b)** Acetone cleaned graphene sample, showing no further cleaning compared to the thermal cleaning.

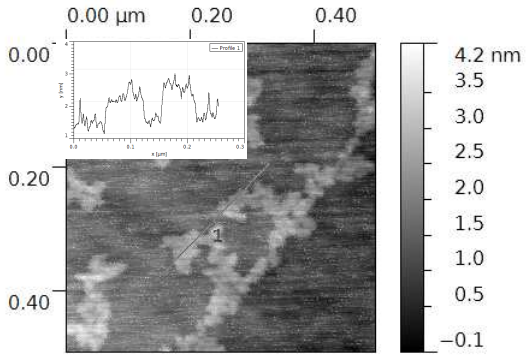

Figure B.2: An example of C_{60} islands forming on some of the graphene samples.

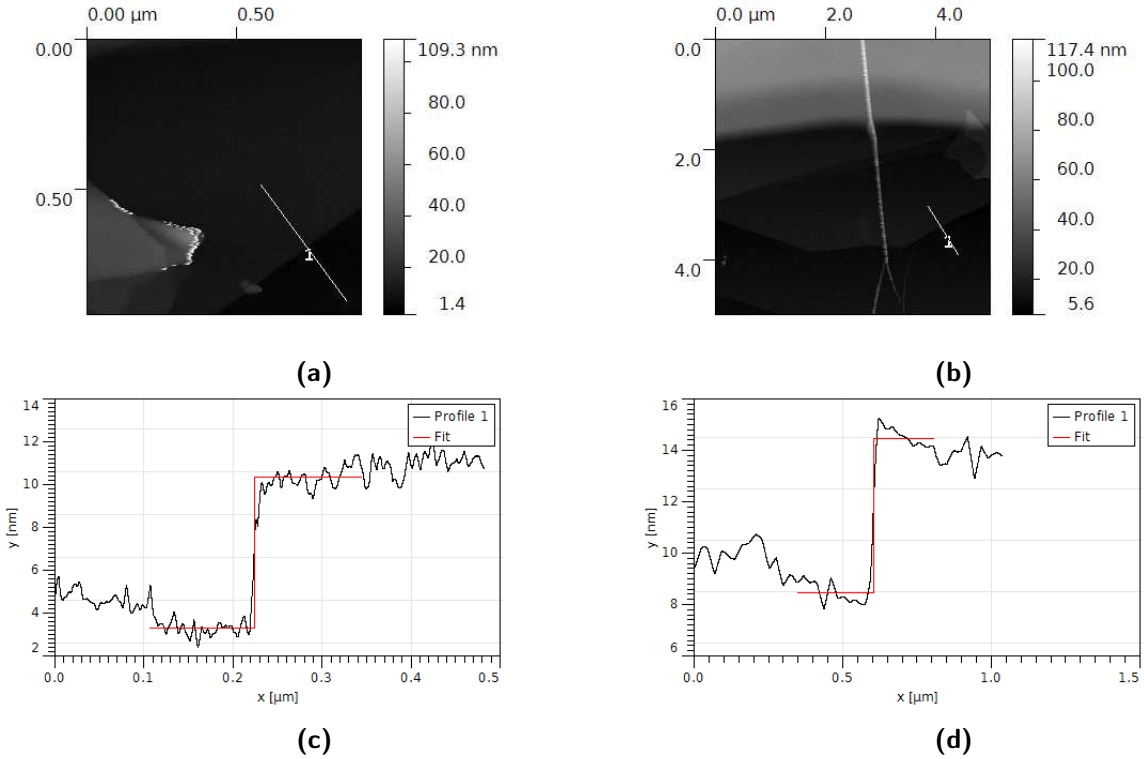

Figure B.3: **(a)** AFM image of a MLG pre-intercalation attempt, with **(c)** being the height profile showing a thickness of 7.05 ± 0.61 nm. **(b)** AFM image of a MLG post-intercalation attempt, with **(d)** being the height profile showing a thickness of 6.29 ± 0.47 nm.

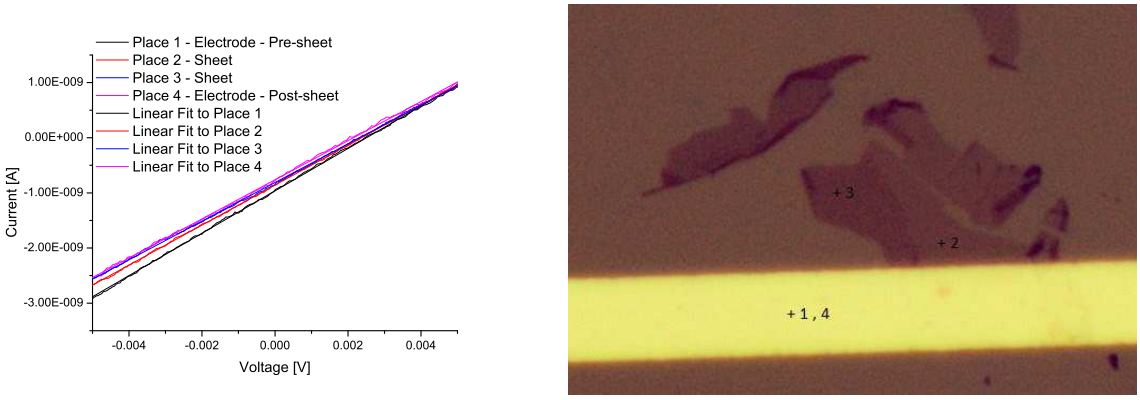

Figure B.4: **(a)** I-V curves corresponding to the points indicated in (b). **(b)** Optical image of the pristine FLG sample used for CAFM, with each site engaged denoted with a number and a +-sign.

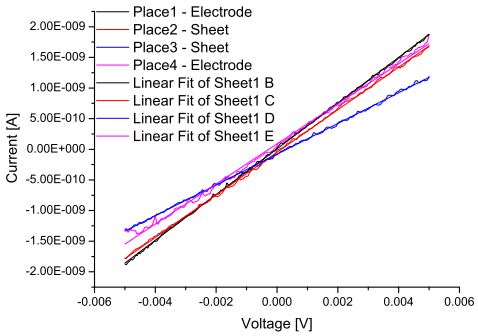

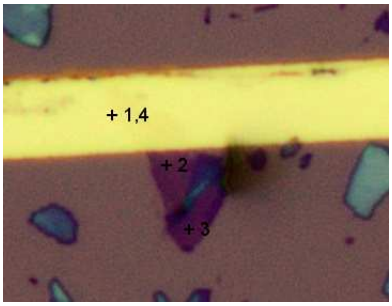

(a) **(b)**

Figure B.5: **(a)** I-V curves corresponding to the points indicated in (b). **(b)** Optical image of the attempted intercalated FLG sample used for CAFM, with each site engaged denoted with a number and a +-sign.

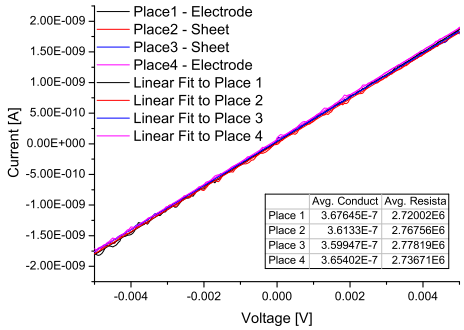

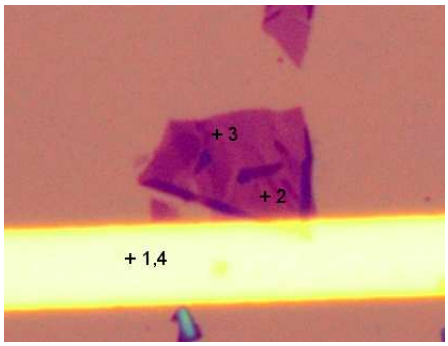

(a) **(b)**

Figure B.6: **(a)** I-V curves corresponding to the points indicated in (b). **(b)** Optical image of the expanded FLG sample used for CAFM, with each site engaged denoted with a number and a +-sign.

Appendix C

Supplementary Theory

Besides explaining some theoretical models in more details, this appendix includes extra calculations that to some extent are important for a better overview of the theory in this thesis or just some calculations that were simple, but very tedious, time consuming and would aid the inexperienced reader.

Tight Binding Model

For a detailed description of the band structure of graphene (SLG to FLG), the tight-binding model yields a satisfactory result for the energy levels in proximity of the Fermi energy. Weakly interacting atoms are a crucial assumption in this model, which gives almost intact atomic orbitals after forming the crystal.

A trial wave function are constructed as the sum between the wave functions for each of the two sub-lattices weighted with the complex functions $a(\mathbf{k})$ and $b(\mathbf{k})$

$$\psi(\mathbf{k},\mathbf{r}) = a(\mathbf{k})\psi_A(\mathbf{k},\mathbf{r}) + b(\mathbf{k})\psi_B(\mathbf{k},\mathbf{r})$$

The electronic wave function for the two sub-lattices can be constructed from a linear combination of atomic p_z-orbitals, $\phi_s(r - R_s)$,

$$\psi_s(\mathbf{k},\mathbf{r}) = \frac{1}{\sqrt{N}} \sum_{\mathbf{R}_s} e^{i\mathbf{k}\mathbf{R}_s} \phi_s(\mathbf{r} - \mathbf{R}_s)$$

with $s = [A, B]$. Searching for solution to the Schrödinger equation, $\mathcal{H}\psi(\mathbf{k},\mathbf{r}) = E(\mathbf{k})\psi(\mathbf{k},\mathbf{r})$, by multiplying with $\psi^*(\mathbf{k},\mathbf{r})$, yields (vector representation)

$$(a^*(\mathbf{k}), b^*(\mathbf{k}))\mathbb{H} \begin{pmatrix} a(\mathbf{k}) \\ b(\mathbf{k}) \end{pmatrix} = E(\mathbf{k})(a^*(\mathbf{k}), b^*(\mathbf{k}))\mathbb{S} \begin{pmatrix} a(\mathbf{k}) \\ b(\mathbf{k}) \end{pmatrix}$$

where the $2x2$ matrices (both $\mathbb{H}$ and $\mathbb{S}$) are given as

$$\mathbb{H} = \begin{pmatrix} H_{AA} & H_{AB} \\ H_{BA} & H_{BB} \end{pmatrix} = \begin{pmatrix} H_{AA} & H_{AB} \\ H^*_{AB} & H_{AA} \end{pmatrix}$$
$$\mathbb{S} = \begin{pmatrix} S_{AA} & S_{AB} \\ S_{BA} & S_{BB} \end{pmatrix} = \begin{pmatrix} S_{AA} & S_{AB} \\ S^*_{AB} & S_{AA} \end{pmatrix}$$

where $H_{ss'} = \langle \Psi_s | \mathcal{H} | \Psi_{s'} \rangle$ and $S_{ss'} = \langle \Psi_s | \Psi_{s'} \rangle$. As SLG contains two different carbon atoms in the unit cell, which by all practical means are indistinguishable, $H_{AA} = H_{BB}$ and $H_{BA} = H^*_{AB}$. For the overlap

matrix, $\mathbb{S}$, it is assumed that the atomic wave functions are normalized, yielding $S_{AA} = S_{BB} = 1$ (the overlap between two normalized identical wave functions is 1).

Including both the tight-binding Hamiltonian and the overlap matrix, for a 2D material with two different atoms in the unit cell, one ends up with the following secular equation to solve

$$\det\left[\mathbb{H} - E\mathbb{S}\right] = 0 \tag{C.1}$$

Solving the determinant in equation C.1, yields

$$E = \frac{2H_{AA}S_{AA} - H^*_{AB}S_{AB} - H_{AB}S^*_{AB} \pm \sqrt{(2H_{AA}S_{AA} - H^*_{AB}S_{AB} - H_{AB}S^*_{AB})^2 - 4(H^2_{AA} - H^*_{AB}H_{AB})(S^2_{AA} - S^*_{AB}S_{AB})}}{2(S^2_{AA} - S^*_{AB}S_{AB})}$$

With inspiration from Reich et al.[70], this equation can be written on the form

$$E = \frac{2E_0 - E_1 \pm \sqrt{(2E_0 - E_1 - 4E_2E_3)}}{2E_3}$$

by substitution of the following definitions

$$\begin{aligned} E_0 &\equiv H_{AA}S_{AA} & E_1 &\equiv H^*_{AB}S_{AB} + H_{AB}S^*_{AB} \\ E_2 &\equiv H^2_{AA} - H^*_{AB}H_{AB} & E_3 &\equiv S^2_{AA} - S^*_{AB}S_{AB} \end{aligned}$$

The matrix elements are

$$\begin{aligned} H_{AA} &= \left(\frac{1}{\sqrt{N}}\sum_{\mathbf{R}_A} e^{-i\mathbf{k}\mathbf{R}_A}\left\langle\phi_{2p_z}(\mathbf{r}-\mathbf{R}_A)\right|\right)\mathcal{H}\left(\frac{1}{\sqrt{N}}\sum_{\mathbf{R}_{A'}} e^{i\mathbf{k}\mathbf{R}_{A'}}\left|\phi_{2p_z}(\mathbf{r}-\mathbf{R}_{A'})\right\rangle\right) \\ &= \frac{1}{N}\sum_{\mathbf{R}_A}\sum_{\mathbf{R}_{A'}} e^{i\mathbf{k}(\mathbf{R}_{A'}-\mathbf{R}_A)}\left\langle\phi_{p_z}(\mathbf{r}-\mathbf{R}_A)|\mathcal{H}|\phi_{p_z}(\mathbf{r}-\mathbf{R}_{A'})\right\rangle \end{aligned}$$

Nearest-Neighbour Approximation For simplicity, only interactions between adjacent carbon atoms are accounted for, i.e. nearest-neighbour approximation, which for H_{AA} only gives a result for $A = A'$

$$H_{AA} \approx \frac{1}{N}\sum_{\mathbf{R}_A}\left\langle\phi_{2_{pz}}(\mathbf{r}-\mathbf{R}_A)|\mathcal{H}|\phi_{2p_z}(\mathbf{r}-\mathbf{R}_A)\right\rangle = \epsilon_{2p_z}$$

ϵ_{2p_z} is the atomic energy for atom in the 2D crystal (the Hamiltonian contains the crystal potential).

In a similar way can H_{AB} and S_{AB} be determined.

$$
\begin{aligned}
H_{AB} &= \left(\frac{1}{\sqrt{N}} \sum_{\mathbf{R}_A} e^{-i\mathbf{k}\mathbf{R}_A} \langle \phi_{2p_z}(\mathbf{r}-\mathbf{R}_A)| \right) \mathcal{H} \left(\frac{1}{\sqrt{N}} \sum_{\mathbf{R}_B} e^{i\mathbf{k}\mathbf{R}_B} |\phi_{2p_z}(\mathbf{r}-\mathbf{R}_B)\rangle \right) \\
&= \frac{1}{N} \sum_{\mathbf{R}_A} \sum_{\mathbf{R}_B} e^{i\mathbf{k}(\mathbf{R}_B-\mathbf{R}_A)} \langle \phi_{p_z}(\mathbf{r}-\mathbf{R}_A)|\mathcal{H}|\phi_{p_z}(\mathbf{r}-\mathbf{R}_B)\rangle \\
&= \frac{1}{N} \sum_{\mathbf{R}_A} \sum_{\mathbf{R}_i} e^{i\mathbf{k}(\mathbf{R}_A-\mathbf{R}_A+\mathbf{R}_i)} \langle \phi_{p_z}(\mathbf{r}-\mathbf{R}_A)|\mathcal{H}|\phi_{p_z}(\mathbf{r}-\mathbf{R}_A-\mathbf{R}_i)\rangle \\
&\approx \gamma_0 f(\mathbf{k}) \qquad , \qquad \text{with } \gamma_0 = \langle \phi_{p_z}(\mathbf{r}-\mathbf{R}_A)|\mathcal{H}|\phi_{p_z}(\mathbf{r}-\mathbf{R}_A-\mathbf{R}_i)\rangle \\
S_{AB} &= \frac{1}{N} \sum_{\mathbf{R}_A} \sum_{\mathbf{R}_i} e^{i\mathbf{k}(\mathbf{R}_A-\mathbf{R}_A+\mathbf{R}_i)} \langle \phi_{p_z}(\mathbf{r}-\mathbf{R}_A)|\phi_{p_z}(\mathbf{r}-\mathbf{R}_A-\mathbf{R}_i)\rangle \\
&\approx s_0 f(\mathbf{k}) \qquad , \qquad \text{with } s_0 = \langle \phi_{p_z}(\mathbf{r}-\mathbf{R}_A)|\phi_{p_z}(\mathbf{r}-\mathbf{R}_A-\mathbf{R}_i)\rangle
\end{aligned}
$$

Here γ_0 and s_0 are the transfer integral and overlap integral between nearest neighbours, respectively, and $f(\mathbf{k}) = e^{i\mathbf{k}\mathbf{R}_1} + e^{i\mathbf{k}\mathbf{R}_2} + e^{i\mathbf{k}\mathbf{R}_3}$, with $\mathbf{R}_1 = a(-1/2, 1/(2\sqrt{3}))$, $\mathbf{R}_2 =$ and $\mathbf{R}_3 =$, the three vectors to the nearest neighbours.

Inserting the calculated matrix elements in the energy dispersion equation, yields:

$$
\begin{aligned}
E(\mathbf{k}) &= \frac{2\epsilon_{2p_z} - 2\gamma_0 s_0 f(\mathbf{k})^2 \pm \sqrt{(2\gamma_0 s_0 f(\mathbf{k})^2 - 2\epsilon_{2p_z})^2 - 4(1-s_0^2 f(\mathbf{k})^2)(\epsilon_{2p_z}^2 - \gamma_0^2 f(\mathbf{k})^2)}}{1 - s_0^2 f(\mathbf{k})^2} \\
&= \frac{\epsilon_{2p_z} \pm \gamma_0 \sqrt{|f(\mathbf{k})|^2}}{1 \pm s_0 \sqrt{|f(\mathbf{k})|^2}}
\end{aligned}
$$

The three parameters ϵ_{2p_z}, s_0 and γ_0, can be estimated by fitting either experimental or first-principles calculation data[70]. The sum of phase factors, $f(\mathbf{k})$, is

$$
f(\mathbf{k}) = 2\cos\left(\frac{a}{2}k_x\right) \exp\left(i\frac{a}{2\sqrt{3}}k_y\right) + \exp\left(-i\frac{a}{\sqrt{3}}k_y\right)
$$

Bibliography

[1] DSL Abergel, V Apalkov, J Berashevich, K Ziegler, and T Chakraborty. Properties of graphene: a theoretical perspective. *Advances in Physics*, 59(4):261–482, 2010.

[2] W Andreoni, P Giannozzi, and M Parrinello. Molecular-structure and chemical bonding in k3c60 and k6c60. *Physical Review B*, 51(4):2087–2097, Jan 15 1995.

[3] S Aronson, C Frishberg, and G Frankl. Thermodynamic properties of the graphite-bisulfate lamellar compounds. *Carbon*, 9(6):715–72, 1971.

[4] A Aviram and MA Ratner. Molecular rectifiers. *Chemical Physics Letters*, 29(2):277–283, 1974.

[5] DM Basko, S Piscanec, and AC Ferrari. Electron-electron interactions and doping dependence of the two-phonon raman intensity in graphene. *Physical Review B*, 80(16), Oct 2009.

[6] C Berger, ZM Song, TB Li, XB Li, AY Ogbazghi, R Feng, ZT Dai, AN Marchenkov, EH Conrad, PN First, and WA de Heer. Ultrathin epitaxial graphite: 2d electron gas properties and a route toward graphene-based nanoelectronics. *Journal of Physical Chemistry B*, 108(52):19912–19916, Dec 30 2004.

[7] G Binnig, CF Quate, and C Gerber. Atomic force microscope. *Physical Review Letters*, 56(9): 930–933, Mar 3 1986.

[8] P Blake, EW Hill, AH Castro Neto, KS Novoselov, D Jiang, R Yang, TJ Booth, and AK Geim. Making graphene visible. *Apllied Physics Letters*, 91(6), Aug 6 2007.

[9] F Boerrnert, L Fu, S Gorantla, M Knupfer, B Buechner, and MH Ruemmeli. Programmable sub-nanometer sculpting of graphene with electron beams. *ACS Nano*, 6(11):10327–10334, Nov 2012.

[10] Bruker, Jun 2013. URL `http://www.bruker.com`.

[11] EV Castro, KS Novoselov, SV Morozov, NMR Peres, JMBL Dos Santos, J Nilsson, F Guinea, AK Geim, and AH Castro Neto. Biased bilayer graphene: Semiconductor with a gap tunable by the electric field effect. *Physical Review Letters*, 99(21), Nov 23 2007.

[12] AH Castro Neto, F Guinea, NMR Peres, KS Novoselov, and AK Geim. The electronic properties of graphene. *Reviews of Modern Physics*, 81(1):109–162, Jan-Mar 2009.

[13] GH Chen, DJ Wu, WU Weng, and CL Wu. Exfoliation of graphite flake and its nanocomposites. *Carbon*, 41(3):619–621, 2003.

[14] J Chen, MA Reed, AM Rawlett, and JM Tour. Large on-off ratios and negative differential resistance in a molecular electronic device. *Science*, 286(5444):1550–1552, Nov 19 1999.

[15] Z Chen, YM Lin, MJ Rooks, and P Avouris. Graphene nano-ribbon electronics. *Physica E-Low-Dimensional Systems & Nanostructures*, 40(2):228–232, Dec 2007.

[16] J Cho, J Smerdon, L Gao, O Suezer, JR. Guest, and NP. Guisinger. Structural and electronic decoupling of c-60 from epitaxial graphene on sic. *Nano Letters*, 12(6):3018–3024, Jun 2012.

[17] MS Dresselhaus and G Dresselhaus. Intrecalation Compounds of Graphite. *Advances in Physics*, 30(2):139–326, 1981.

[18] MS Dresselhuas, G Dresselhaus, and PC Eklund. *Science of Fullerenes and Carbon Nanotubes*. Academic Press, 1996.

[19] G Eda, G Fanchini, and M Chhowalla. Large-area ultrathin films of reduced graphene oxide as a transparent and flexible electronic material. *Nature Nanotechnology*, 3(5):270–274, May 2008.

[20] H Fernandezmoran. Single-crystal of graphite and of mica as specimen support for electron microscopy. *Journal of Applied Physics*, 31(10):1840, 1960.

[21] AC Ferrari and DM Basko. Raman spectroscopy as a versatile tool for studying the properties of graphene. *Nature Nanotechnology*, 8(4):235–246, Apr 2013.

[22] AC Ferrari, JC Meyer, V Scardaci, C Casiraghi, M Lazzeri, F Mauri, S Piscanec, D Jiang, KS Novoselov, S Roth, and AK Geim. Raman spectrum of graphene and graphene layers. *Physical Review Letters*, 97(18), Nov 3 2006.

[23] MS Fuhrer, JG Hou, XD Xiang, and A Zetil. C60 intercalated graphite - predictions and experiments. *Solid State Communications*, 90(6):357–360, May 1994.

[24] AK Geim and KS Novoselov. The rise of graphene. *Nature Materials*, 6(3):183–191, Mar 2007.

[25] MO Goerbig. Electronic properties of graphene in a strong magnetic field. *Review of Modern Physics*, 83:1193–1243, Nov 2011.

[26] A Grüneis, C Attaccalite, L Wirtz, H Shiozawa, R Saito, T Pichler, and A Rubio. Tight-binding description of the quasiparticle dispersion of graphite and few-layer graphene. *Physical Review B*, 78:205425, Nov 2008.

[27] Arnold Gruppe, Feb 2013. URL `http://www.arnold-gruppe.de`.

[28] V Gupta, P Scharff, K Risch, H Romanus, and R Muller. Synthesis of c-60 intercalated graphite. *Solid State Communications*, 131(3-4):153–155, Jul 2004.

[29] V Gupta, P Scharff, LC Abelmann, and L Spiess. C-60 intercalated graphite: A new form of carbon. *Fullerenes Nanotubes and Carbon Nanostructures*, 13(1):427–430, May 24-28 2005.

[30] CR Hansen, TJ Sørensen, M Glyvradal, J Larsen, SH Eisenhardt, T Bjørnholm, MM Nielsen, R Feidenhans'l, and BW Laursen. Structure of the buried metal-molecule interface in organic thin film devices. *Nano Letters*, 9(3):1052–1057, 2009.

[31] AF Hebard, MJ Rosseinsky, RC Haddon, DW Murphy, SH Glarum, TTM Palstra, AP Ramirez, and AR Kortan. Superconductivity at 18-k in potassium-doped c-60. *Nature*, 350(6319):600–601, Apr 18 1991.

[32] WC Hu, K Sarveswaran, M Lieberman, and GH Bernstein. Sub-10 nm electron beam lithography using cold development of poly(methylmethacrylate). *Journal of Vacuum Science & Technology B*, 22(4):1711–1716, Jul-Aug 2004.

[33] IMSI/Design. Designcad 3d max, Jul 2013. URL `http://www.imsidesign.com/`.

[34] National Instruments. Labview, Aug 2013. URL `http://sine.ni.com/np/app/main/p/docid/nav-104/lang/da/`.

[35] HG Jee, JH Han, HN Hwang, YD Kim, and CC Hwang. Adsorption and desorption of fullerene on graphene/sic(0001). *Surface Science*, 605(7-8):649–653, Apr 2011.

[36] JE Jones. On the determination of molecular fields. ii. from the equation of state of a gas. *Proceedings of the Royal Society of London. Series A*, 106(738):463–477, 1924.

[37] KS Kim, Y Zhao, H Jang, SY Lee, JM Kim, KS Kim, JH Ahn, P Kim, JY Choi, and BH Hong. Large-scale pattern growth of graphene films for stretchable transparent electrodes. *Nature*, 457 (7230):706–710, Feb 5 2009.

[38] DV Kosynkin, AL Higginbotham, A Sinitskii, JR Lomeda, A Dimiev, BK Price, and JM Tour. Longitudinal unzipping of carbon nanotubes to form graphene nanoribbons. *Nature*, 458(7240): 872–U5, Apr 16 2009.

[39] W Kratschmer, LD Lamb, K Fostiropoulos, and DR Huffman. Solid c-60 - a new form of carbon. *Nature*, 347(6291):354–358, Sep 27 1990.

[40] HW Kroto, JR Heath, SC Obrien, RF Curl, and RE Smalley. C-60 - buckminsterfullerene. *Nature*, 318(6042):162–163, 1985.

[41] HW Kroto, AW Allaf, and SP Balm. C-60 - buckminsterfullerene. *Chemical Reviews*, 91(6): 1213–1235, Sep-Oct 1991.

[42] C Lee, X Wei, JW Kysar, and J Hone. Measurement of the elastic properties and intrinsic strength of monolayer graphene. *Science*, 321(5887):385–388, Jul 18 2008.

[43] NJ Lee, JW Yoo, YJ Choi, CJ Kang, DY Jeon, DC Kim, S Seo, and HJ Chung. The interlayer screening effect of graphene sheets investigated by kelvin probe -force microscopy. *APPLIED PHYSICS LETTERS*, 95(22), Nov 30 2009.

[44] G Li, HT Zhou, LD Pan, Y Zhang, JH Mao, Q Zou, HM Guo, YL Wang, SX Du, and HJ Gao. Self-assembly of c-60 monolayer on epitaxially grown, nanostructured graphene on ru(0001) surface. *Applied Physics Letters*, 100(1):013304, 2012.

[45] LM Malard, MA Pimenta, G Dresselhaus, and MS Dresselhaus. Raman spectroscopy in graphene. *Physics Report-Review Section of Physics Letters*, 473(5-6):51–87, Apr 2009.

[46] CA Martin, D Ding, JK Sorensen, T Bjornholm, JM van Ruitenbeek, and HSJ van der Zant. Fullerene-based anchoring groups for molecular electronics. *Journal of the American Chemical Society*, 130(40):13198–13199, Oct 8 2008.

[47] Delta Mask, May 2013. URL `http://www.deltamask.nl/`.

[48] MathWorks. Matlab, Jul 2013. URL `http://www.mathworks.se/products/matlab/`.

[49] E McCann. Asymmetry gap in the electronic band structure of bilayer graphene. *Physical Review B*, 74(16), Oct 2006.

[50] E McCann and VI Fal'ko. Landau-level degeneracy and quantum hall effect in a graphite bilayer. *Physical Review Letters*, 96(8), Mar 3 2006.

[51] E McCann and M Koshino. The electronic properties of bilayer graphene. *Reports on Progress in Physics*, 76(5), May 2013.

[52] AM Moore, AA Dameron, BA Mantooth, RK Smith, DJ Fuchs, JW Ciszek, F Maya, YX Yao, JM Tour, and PS Weiss. Molecular engineering and measurements to test hypothesized mechanisms in single molecule conductance switching. *Journal of the American Chemical Society*, 128 (6):1959–1967, Feb 15 2006.

[53] SV Morozov, KS Novoselov, MI Katsnelson, F Schedin, DC Elias, JA Jaszczak, and AK Geim. Giant intrinsic carrier mobilities in graphene and its bilayer. *Physical Review Letters*, 100(1), Jan11 2008.

[54] K Moth-Poulsen and T Bjornholm. Molecular electronics with single molecules in solid-state devices. *Nature Nanotechnology*, 4(9):551–556, Sep 2009.

[55] μMasch. Spm tip producer, Jul 2013. URL `http://www.spmtips.com/`.

[56] D Necas and P Klapetek. Gwyddion: an open-source software for SPM sata analysis, 2012. URL `http://gwyddion.net/`.

[57] J Nilsson, AH Castro Neto, F Guinea, and NMR Peres. Electronic properties of bilayer and multilayer graphene. *Physical Review B*, 78(4), Jul 2008.

[58] DE Nixon and GS Parry. Formation and structure of potassium graphites. *Journal of Physics D-Applied Physics*, 1(3):291–&, 1968.

[59] KS Novoselov, AK Geim, SV Morozov, D Jiang, Y Zhang, SV Dubonos, IV Grigorieva, and AA Firsov. Electric field effect in atomically thin carbon films. *Science*, 306(5696):666–669, Oct 22 2004.

[60] KS Novoselov, AK Geim, SV Morozov, D Jiang, MI Katsnelson, IV Grigorieva, SV Dubo-nos, and AA Firsov. Two-dimensional gas of massless dirac fermions in graphene. *Nature*, 438(7065): 197–200, Nov 10 2005.

[61] KS Novoselov, Z Jiang, Y Zhang, SV Morozov, HL Stormer, U Zeitler, JC Maan, GS Boebinger, P Kim, and AK Geim. Room-temperature quantum hall rffect in graphene. *Science*, 315(5817): 1379, Mar 9 2007.

[62] P O'Brien, H Craighead, H Kroto, and MS Amer. *Raman Spectroscopy Fullerenes and Nanotechnology*. RSC Nanoscience and Nanotechnology. The Royal Society of Chemistry, 2010.

[63] T Ohta, A Bostwick, T Seyller, K Horn, and E Rotenberg. Controlling the Electronic Structure of Bilayer Graphene. *Science*, 313(5789):951–954, Aug 18 2006.

[64] OriginLab. Originpro 8.6, Aug 2013. URL `http://www.originlab.com/`.

[65] TTM Palstra, O Zhou, Y Iwasa, PE Sulewski, RM Fleming, and BR Zegarski. Superconductivity at 40k in cesium doped c-60. *Solid State Communications*, 93(4):327–330, Jan 1995.

[66] H Park, AKL Lim, AP Alivisatos, J Park, and PL McEuen. Fabrication of Metallic Electrodes with Nanometer Separation by Electromigration. *Applied Physics Letters*, 75(2):301–303, Jul 12 1999.

[67] NMR. Peres. The electronic properties of graphene and its bilayer. *Vacuum*, 83(10):1248–1252, Jun 16 2009.

[68] NMR Peres. Colloquium: The transport properties of graphene: An introduction. *Reviews of Modern Physics*, 82(3):2673–2700, Sep 15 2010.

[69] MA Reed, C Zhou, CJ Muller, TP Burgin, and JM Tour. Conductance of a Molecular Junction. *Science*, 278(5336):252–254, Oct 10 1997.

[70] S Reich, J Maultzsch, C Thomsen, and P Ordejón. Tight-binding description of graphene. *Physical Review B*, 66:035412, Jul 2002.

[71] C Rogero, JI Pascual, J Gomez-Herrero, and AM Baro. Resolution of site-specific bonding properties of c-60 adsorbed on au(111). *Journal of Chemical Physics*, 116(2):832–836, Jan 8 2002.

[72] R Saito, G Dresselhaus, and MS Dresselhaus. *Physical Properties of Carbon Nanotube*. Imperial College Press, 1998.

[73] S Saito and A Oshiyama. Ionic metal kxc60 - cohesion and energy-bands. *Physical Review B*, 44 (20):11536–11539, Nov 15 1991.

[74] S Saito and A Oshiyama. Cohesive mechanism and energy-bands of solid c60. *Physical Review Letters*, 66(20):2637–2640, May 20 1991.

[75] S Saito and A Oshiyama. Design of c(60)-graphite cointercalation compounds. *Physical Review B*, 49(24):17413–17419, Jun 15 1994.

[76] F Schwierz. Graphene transistors. *Nature Nanotechnology*, 5(7):487–496, Jul 2010.

[77] SHR Sena, JM Pereira, Jr., GA Farias, FM Peeters, and RN Costa Filho. The electronic properties of graphene and graphene ribbons under simple shear strain. *Journal of Physics-Condensed Matter*, 24(37), Sep 19 2012.

[78] Sigma-Aldrich, Dec 2012. URL `http://www.sigmaaldrich.com`.

[79] JK Sorensen, J Fock, AH Pedersen, AB Petersen, K Jennum, K Bechgaard, K Kilsa, V Geskin, J Cornil, T Bjornholm, and MB Nielsen. Fulleropyrrolidine end-capped molecular wires for molecular electronics-synthesis, spectroscopic, electrochemical, and theoretical characterization. *Journal of Organic Chemistry*, 76(1):245–263, Jan 7 2011.

[80] K Tanigaki, TW Ebbesen, S Saito, J Mizuki, JS Tsai, Y Kubo, and S Kuroshima. Superconductivity at 33-k in csxrbyc60. *Nature*, 352(6332):222–223, Jul 18 1991.

[81] P Venezuela, M Lazzeri, and F Mauri. Theory of double-resonant raman spectra in graphene: Intensity and line shape of defect-induced and two-phonon bands. *Physical Review B*, 84:035433, Jul 2011.

[82] M. Švec, P. Merino, Y. J. Dappe, C. González, E. Abad, P. Jelínek, and J. A. Martín-Gago. van der waals interactions mediating the cohesion of fullerenes on graphene. *Physical Review B*, 86: 121407, Sep 2012.

[83] PR Wallace. The band theory of graphite. *Physical Review*, 71(9):622–634, 1947.

[84] R Wang, S Wang, X Wang, JAS Meyer, P Hedegard, BW Laursen, Z Cheng, and X Qiu. Charge transfer and current fluctuations in single layer graphene transistors modified by self-assembled c60 adlayers. *Small*, 9:2420–6, Jul 22 2013.

[85] X Wang and H Dai. Etching and narrowing of graphene from the edges. *Nature Chemistry*, 2(8): 661–665, Aug 2010.

[86] Wieweb. Clewin 4, Dec 2012. URL `http://www.wieweb.com/ns6/index.html`.

[87] G Xie, Z Shi, R Yang, D Liu, W Yang, M Cheng, D Wang, D Shi, and G Zhang. Graphene edge lithography. *Nano Letters*, 12(9):4642–4646, Sep 2012.

[88] O Zhou, JE Fischer, N Coustel, S Kycia, Q Zhu, AR McGhie, WJ Romanow, JP McCauley, AB Smith, and DE Cox. Structure and bonding in alkali-metal-doped c60. *Letters to Nature*, 351:462–464, Jun 1991.